DESIGN AND IMPLEMENTATION OF A NEW BIOFIDELIC ATD NECK FOR REAR IMPACTS

An Undergraduate Honors Thesis
Submitted to the Department of Mechanical and Aerospace Engineering
The Ohio State University
In Fulfillment of the Requirements
For Graduation with Honors Research Distinction in Mechanical Engineering

Jonathon Louis Blank

Advisor: Dr. Yun Seok Kang

May, 2018

ABSTRACT

Anthropomorphic test devices (ATDs) are intended to provide a humanlike response in experimental scenarios where using human volunteers or post-mortem human surrogates (PMHS) are either inappropriate or impossible. Therefore, an effective ATD must be biofidelic, meaning that it must replicate the response of a human in an automotive impact. A current regulation allows for the use of the Hybrid III ATD in rear impacts although it was designed for frontal impacts only, and the ATD's neck has been found to exhibit poor biofidelity in this scenario. One of the more biofidelic rear impact necks, the BioRID II, only allows for 2D sagittal plane motions due to its use of revolute joints between each pair of cervical vertebrae. The purpose of this study is to provide a new biofidelic, mechanical design for an ATD neck that allows more degrees of freedom, making it more representative of a human's neck and therefore more biofidelic. The neck's design is intended to anatomically replicate a human neck and includes seven individual vertebrae. Spherical joints were used in between these vertebrae, with the exception of the C1 and C2 revolute coupling, thus accommodating more degrees of freedom. Four strands of wire rope, two anterior and two posterior, in combination with polymer damping material, were utilized in the design to control the kinematics of the neck. Dynamic simulations using a commercial multibody dynamics software (e.g. MSC ADAMs) were conducted in order to validate the design's biofidelity by mimicking the results of previous rear impact PMHS study conducted at The Ohio State University. Damping material and wire ropes were modeled using two and one-way spring dampers, respectively. A physical model was then fabricated, and a rear impact will be simulated on a sliding head and neck fixture. Biomechanical targets created from this previous rear impact PMHS studies were used to evaluate the responses from the simulation, and will be used to assess the bofidelity of the physical model. NHTSA

biorank scores (BRS) were calculated to evaluate the results of the simulation. BRS for head kinematics measured from the simulation was less than two. The resulting ATD neck is the product of a novel design process with the objective of improving biofidelity. The neck will ultimately help to increase occupant safety in rear-end automotive collisions as it will provide car manufacturers with a more humanlike tool from which they can base future car safety design features.

ACKNOWLEDGMENTS

I would firstly like to thank my advisor on this project, Dr. Yun Seok Kang. I met Dr. Kang in an interesting way during my very first day volunteering at the lab, as he was in the middle of test preparation. It was my first experience working with a PMHS. When I approached Dr. Kang with this project at the forefront of my interest a year and a half later, he was excited, and he supported me and helped me lay out a plan to make it my honors thesis. I would say that our student-advisor relationship is unique, as he is more than willing to help or guide me at a moment's notice. I have learned very many things from Dr. Kang because he had challenged me and tested my ability to think critically throughout the entirety of the project. Dr. Kang not only taught me a great deal about biomechanics and ATDs, but he also taught me how to be thorough, how to maintain my work-life balance, and the importance of listening to my advisor.

I would also like to thank Dr. John Bolte IV, who advised me on other projects outside of this thesis. Two and a half years ago we met for the first time when I was invited to visit the lab. I had no idea what my direction was – the only things I knew were that I wanted to be an engineer and had a general interest in mechanical engineering and biomechanics, although I knew absolutely nothing about the latter. Despite my lack of experience Dr. Bolte welcomed me into his lab. During my time in the lab, Dr. Bolte held me to a very high standard, something that at times I didn't even think myself capable. Dr. Bolte also gave me valuable opportunities outside of the lab space, such as being able to work with the Transportation Research Center and Humanetics ATD. I owe a lot to Dr. Bolte for giving me confidence as a researcher and helping me get a start in biomechanics.

The rest of the students and staff of the Injury Biomechanics Research Center have been of phenomenal support during my honors thesis. I would specifically like to thank Dr. Rakshit

Ramachandra, David Stark, Arriana Willis, Stephen Rudolph, Warren Lee, and Noah Eckstein. Whether it involved helping with testing, machining, or freeing me up in order to work on my thesis, or any other project, they found a way. Blood, sweat, and tears (quite literally) have been spent on this project and other projects of mine.

The Robert O. Webster Machine Shop and staff were of vital importance to this project. I would specifically like to thank Aaron Osborn for his expertise in machining. He was very patient and helped me not only develop my parts but develop my skills as a machinist. Also, I would like to thank Johnathan Shover and the Astronomy Machine Shop for their assistance in assembling the prototype neck.

Finally, I would like to thank my parents and my brother, Christopher, for their phenomenal support during this entire experience. Because of them, my life outside of being a student is very stable and secure.

TABLE OF CONTENTS

LIST OF FIGURES

LIST OF TABLES

Chapter 1: Introduction

1.1 ATD Background and Applications

An anthropometric test device (ATD) is a mechanical component that is used in injurious automotive crash scenarios. ATDs are meant to replicate the response of a living person of a specific demographic in these experiments. Typically, ATDs are used when post-mortem human subjects (PMHS) are not available or feasible to use. Thus, the ATD is intended to be a powerful and convenient tool for researchers to use to better understand the effects of car collisions on their passengers, and with this knowledge, occupant safety systems in vehicles become more effective.

ATDs are robust and stiff mechanical fixtures that accurately depict the human anatomy. The ATD head is typically a metal casting that supports instrumentation about the center of gravity of the head, which typically consist of three accelerometers. The head is covered in a vinyl skin, which can be seen in use throughout the entire body [1]. ATD necks usually consist of rigid segments connected by spring-like components. The torso of the ATD varies greatly across all models, however it always consists of a ribcage and a lumbar spine, along with internal data acquisition devices. Newer models incorporate pressure sensors in the lower abdomen. The limbs of the ATD are typically metal with a vinyl skin, and the limbs display the same degrees of freedom as an actual human limb. Despite these consistencies, the anatomy of an ATD can vary greatly from model to model because each model of an ATD is intended to represent a certain demographic. The variation of these ATDs is primarily found in their mass and stature, which are signified by specifying a percentile corresponding to the population of interest. Examples of these demographics include the 50^{th} percentile male, 5^{th} percentile female, the elderly, and children. The Hybrid III 50^{th} male is currently the most popular ATD in industry (Figure 1) [3].

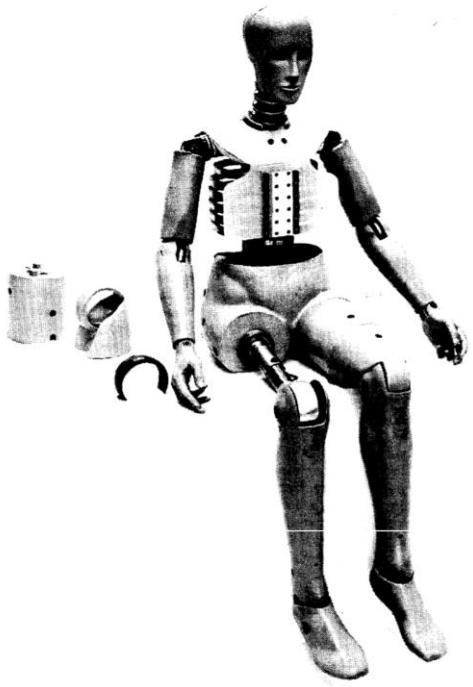

Figure 1: Hybrid III 50th male anthropomorphic test device

1.2 Biofidelity

Biofidelity, in this application, is defined as the faithfulness with which an ATD replicates the response of a human in an experimental scenario. In injury biomechanics, specifically in automotive safety applications, it is a means that researchers use to validate tools that are fabricated to mimic the behavior of a human during an experimental scenario. The tools that these researchers seek to calibrate are ATDs. Having more biofidelic ATDs means that researchers will have a more concrete understanding of the response of a human in a simulated car collision. As a result of this biofidelity, improvements can be made in vehicular occupant safety based on the response provided by the ATD.

Engineers can evaluate the biofidelity of an ATD by comparing its own response in an experiment to the response of a PMHS in the same experimental scenario. This is because a PMHS is the closest representation of a living person that can be used in an injurious

biomechanics experiment. The system used to evaluate the biofidelity utilized corridors comprised of the mean PMHS response and a standard deviation above and below that same response. If the ATD were to stay within the corridor for this same measurement, then it is considered to have good biofidelity in that area. Specifically, biorank is used as a quantitative measure of the correlation of the ATD's response to the target corridor. Biorank is the cumulative variance between the ATD response and mean human response over the cumulative variance between the mean human response and the mean plus one standard deviation [36].

1.3 ATD Necks and Limitations

The neck region of the ATD is an area that can be improved upon in its design to promote biofidelity. Specifically, innovation is required for studying rear impacts and how they affect passenger safety. Current standards for head restraint systems, as seen in FMVSS 202a (Federal Motor Vehicle Safety Standard), are misguided. This setup utilizes a Hybrid III for rear impact assessment, even though the Hybrid III ATD was designed to be a frontal impact assessment device [10]. Also, many studies indicate that the Hybrid III, the latest model in the Hybrid series and the most popular ATD in use today, has a neck that is much too stiff to be considered biofidelic [1]. The Hybrid III is considered a poor device for predicting whiplash injury in high crash severity scenarios and is considered simple when compared to the complexity of a human neck [2]. This comes as no surprise when examining the design of the Hybrid III, which features three aluminum plates connected by an elastomer mold with a steel cable core [3]. The Hybrid III neck design can be seen in Figure 2.

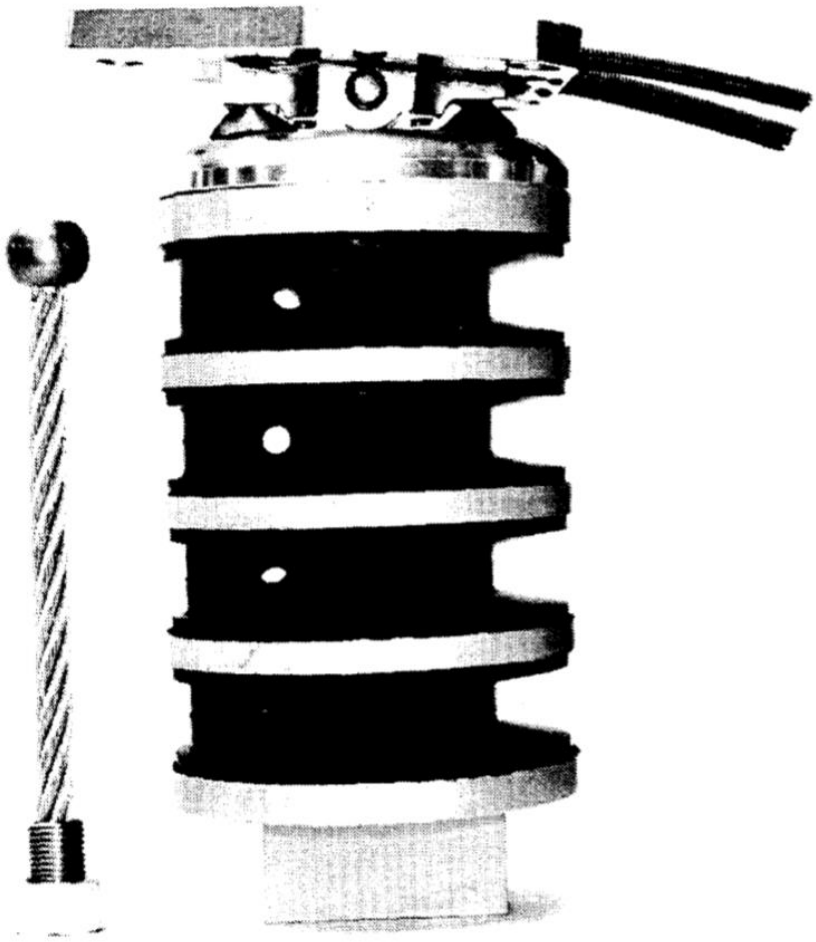

Figure 2: Hybrid III 50th Male Neck Design [3]

The Hybrid III dummy also lacks a thoracic spine, having a rigid, spineless body attached to a mechanical neck at the base of the neck. This is concerning because, when considering passenger safety for rear impacts, a biofidelic ATD should be used as a standard.

When looking to ATD necks that have better biofidelity in comparison to PMHS response, the BioRID II neck prevails among others [37]. This neck features seven cervical vertebrae connected to a complete thoracic spine, each being made of Delrin and connected by hinge joints in combination with elastic urethane components. Spring-damper cable systems, one anterior and one posterior, act as muscle substitutes and are intended to replicate the kinematics

seen in rear impacts [13] [25]. The BioRID II neck (Figure 3) proved to be more biofidelic than the Hybrid III in multiple rear impact scenarios [9].

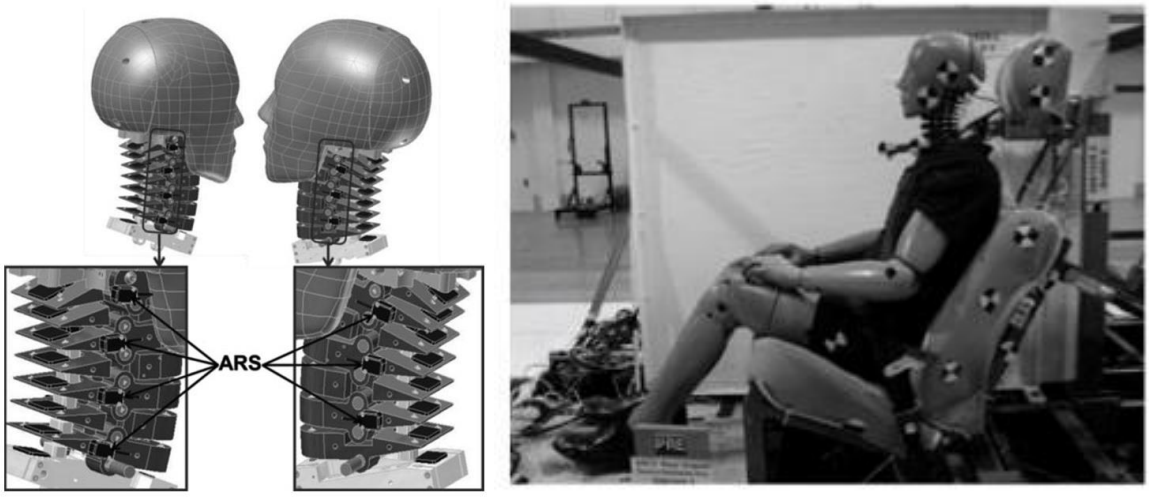

Figure 3: BioRID II ATD neck and dummy [35] [37]

The limitation in the BioRID II neck is that it only permits 2D sagittal plane rotational motion. This is not true to reality, as rear impacts will inevitably force motion that involved much more complex kinematics than 2D sagittal plane kinematics. If an ATD neck were to display the response of the BioRID II with more degrees of freedom, then it should be considered more biofidelic because it is more representative of the motion of a human neck.

1.4 Previous Rear Impact Research

Neck response in rear impacts has always been a topic of interest in injury biomechanics and has thus been the focus of many PMHS studies. One study in particular obtained the biomechanical responses of PMHS in moderate and low speed rear impact conditions [28]. This study, done at the Injury Biomechanics Research Center at The Ohio State University, simulated these rear impact conditions using an experimental seat with a head restraint system. Accelerometers and angular rate sensors were used to capture the kinematics of the event with respect to the center of gravity of the PMHS head. Using fourteen tests with seven PMHS, the

study was able to characterize the inertial response of the head and neck to a low-speed rear impact for an event time of 124 milliseconds. After 124 milliseconds, the PMHS head contacts the padded head restraint and is no longer in isolated movement. This characterization, at the time, was then used to validate the response of an ATD to the same impact conditions. This same PMHS response will now be used to validate the experimental ATD neck designed and fabricated in this study.

1.5 Focus of Thesis

The purpose of this study was to create a biofidelic ATD design for rear impacts that allowed for more realistic kinematics with multiple DOFs. The introduction of more DOFs can make even the most biofidelic neck with one DOF more realistic to a human's response. This research uses undergraduate level engineering curriculum to solve a real-world biomechanics problem. Previous knowledge of design and materials were used to design the new neck for rear impacts. Experience in biomechanics and kinematics were used to analyze whether the new neck design was biofidelic for rear impacts. Finally, this project seeks to establish a design and design process, both virtual and physical, for biofidelic rear impact necks that can be used in future studies.

1.6 Significance of Research

Vehicle crashes today are a problem because they are an enormous cost to society. Based on previous years' data, it was projected that in the first nine months of 2017 alone that an estimated 27,650 fatalities would result from car crashes, which is also a marginal increase from the previous years' numbers [27]. Car crashes are a prominent issue and will continue to be as people continue to drive and as more cars are driven.

The need for a biofidelic ATD neck in industry cannot be understated because of the implications it would have towards improving passenger safety. From 1988 to 1966 alone, 805,581 annual whiplash injuries resulted from crashes in passenger vehicles [10]. About a third of these incidents were the result of a rear impact. Later, in 2002, the average cost of whiplash injuries was $9,994, which corresponded to a total annual cost of $2.7 billion for whiplash injuries [10]. Others have estimated this cost to be higher, ranging from $4.5-7 billion in total expenses [11]. The statistics show that the societal cost of whiplash injuries resulting from car collisions is enormous. Minimizing the amount of whiplash injuries would not only reduce this cost, but it also has potential to provide safer roadways for citizens of the US.

Specifically, rear impacts in passenger vehicles are the main cause of car related whiplash injuries. It has been shown that whiplash injury from a rear impact is twice as likely as the same injury from a frontal impact [12]. In fact, neck related injuries are the most prominent form of injury obtained in a rear end impact, and there is much higher risk for neck injury in a rear impact than there is for any other type of automotive crash [26]. For this reason, it is important that rear impacts are better understood. One way to improve research done in rear impacts is by designing an ATD neck that retains biofidelity while permitting multiple DOF movement. The improved biofidelity would allow for a more humanlike response from ATDs in a rear impact. Also, rear impacts involving real people are complex dynamic scenarios that force a neck response with kinematics in multiple directions. It is paramount that the neck created in this study has more DOF in order to account for this.

1.7 Objectives

This study seeks to develop a design for a biofidelic ATD neck for rear impacts. The thesis will be split into eight chapters. The Chapter 2 will discuss the details of how the human

neck operates and its anatomy's contribution to its function. Chapter 3 will discuss how the neck design was created along with how the neck was modeled using a kinematic software using a design constructed in a computer aided design software. The purpose of this simulation was to evaluate the biofidelity of the design on a preliminary level, utilizing a simulated that used an input provided by a previous PMHS study. After this preliminary validation stage, the neck was fabricated, which will be described in Chapter 4. Chapter 5 will present the results comparing the response of the designed neck to the response of the PMHS in the previous study. Chapter 6 will discuss whether this experimentation validated the new neck design's biofidelity for rear impacts, as well as discussing the feasibility of the design and any limitations that exist in this study. Finally, Chapter 7 will state conclusions and the future work to be done with this project.

Chapter 2: The Anatomy of the Cervical Spine

2.1 Overall Characteristics, Kinematics, and Dimensions

The cervical spine is composed of seven vertebrae and makes up the upper portion of the human spine. The cervical spine protects the spinal cord and provides support for the head. Also, the cervical spine allows for movement of the head in every direction, and the individual vertebrae are responsible for bearing a vertical load. Forms of motion that are particularly important to this project are those of angular flexion, extension, lateral bending, and axial rotation. Figure 4 shows these mechanisms of movement.

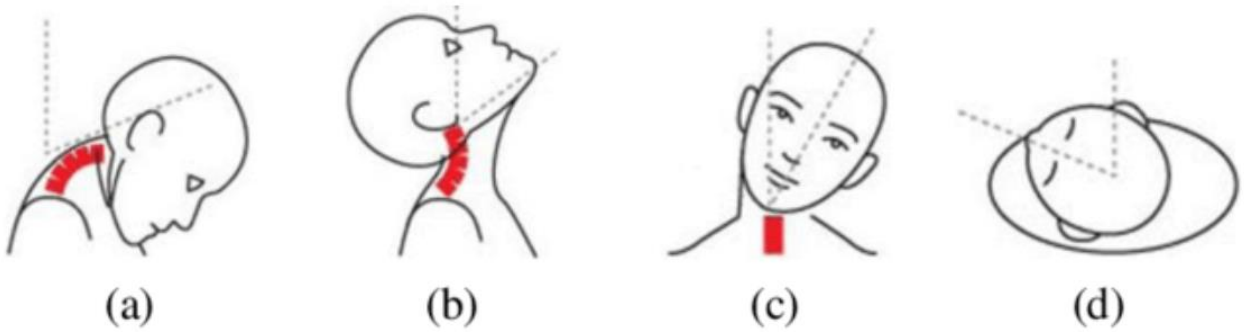

Figure 4: Neck flexion (a), extension(b), lateral bending (c), and axial rotation (d) [14]

All four kinematic scenarios are possible in a rear impact crash, and thus a mechanical neck for an ATD should replicate all four mechanisms. The sign convention for rotation and moments about the three principal axes of the neck is shown in Figure 5.

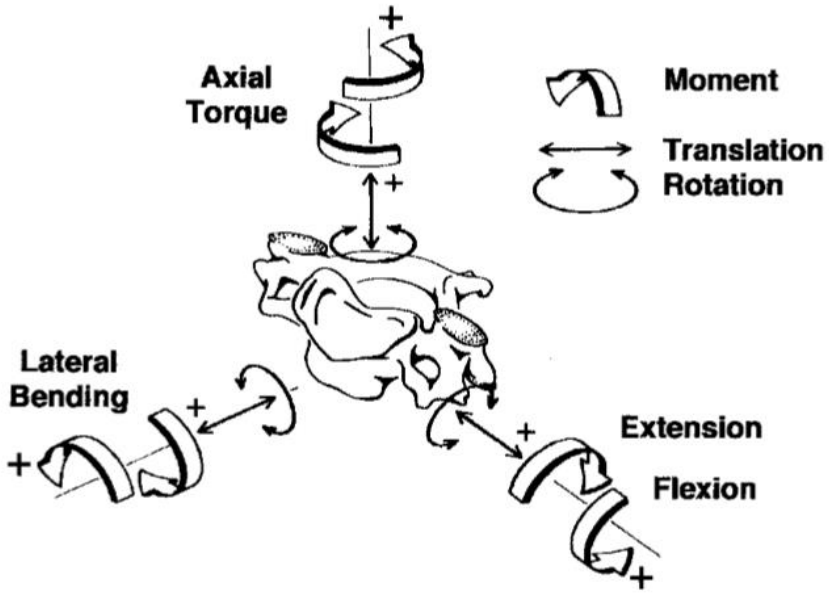

Figure 5: Directions of neck movement with respect to the individual vertebra [15]

The relative rotational displacement of each pair of vertebrae were characterized in a previous study [15]. Values for those displacements can be seen in Table 1.

Table 1: Values for rotational displacement between vertebrae (degrees) [15]

	C0-C1	C1-C2	C2-C3	C3-C4	C4-C5	C5-C6	C6-C7	Total ROM
Flexion	7.2 ± 2.5	12.3 ± 2.0	3.5 ± 1.3	4.3 ± 2.9	5.3 ± 3.0	5.5 ± 2.6	3.7 ± 2.1	41.8 ± 6.4
Extension	20.2 ± 4.6	12.1 ± 6.5	2.7 ± 1.0	3.4 ± 2.1	4.8 ± 1.9	4.4 ± 2.8	3.4 ± 1.9	51.0 ± 9.2
Axial Rotation	9.9 ± 3.0	56.7 ± 4.8	3.3 ± 0.8	5.1 ± 1.2	6.8 ± 1.3	5.0 ± 1.0	2.9 ± 0.8	89.7 ± 6.1
Lateral Bending	9.1 ± 1.5	6.5 ± 2.3	9.6 ± 1.8	9.0 ± 1.9	9.3 ± 1.7	6.5 ± 1.5	5.4 ± 1.5	55.4 ± 4.7

The individual rotational displacement between each pair of vertebrae was summated to represent the overall range of motion of the neck in every form of rotation. The values for axial rotation and lateral bending are a sum of the range of motion of both the left and right side. If a neck is to be biofidelic, is needs to have ranges of motion that are similar to the human neck, which can be validated using this study.

In a previous rear impact study, the neck masses for five PMHS were taken with the soft tissue still attached. The resultant value was 1.5 ± 0.1 kg, and a biofidelic neck should have a similar mass [8].

2.2 Vertebrae

The cervical spine consists of seven vertebrae that vary in structure based on their function and range of motion. One of these functions is protection of the spinal cord, which is seen in the vertebra's construction since it has a large opening in its center. Figure 6 shows the geometry of a typical cervical vertebra

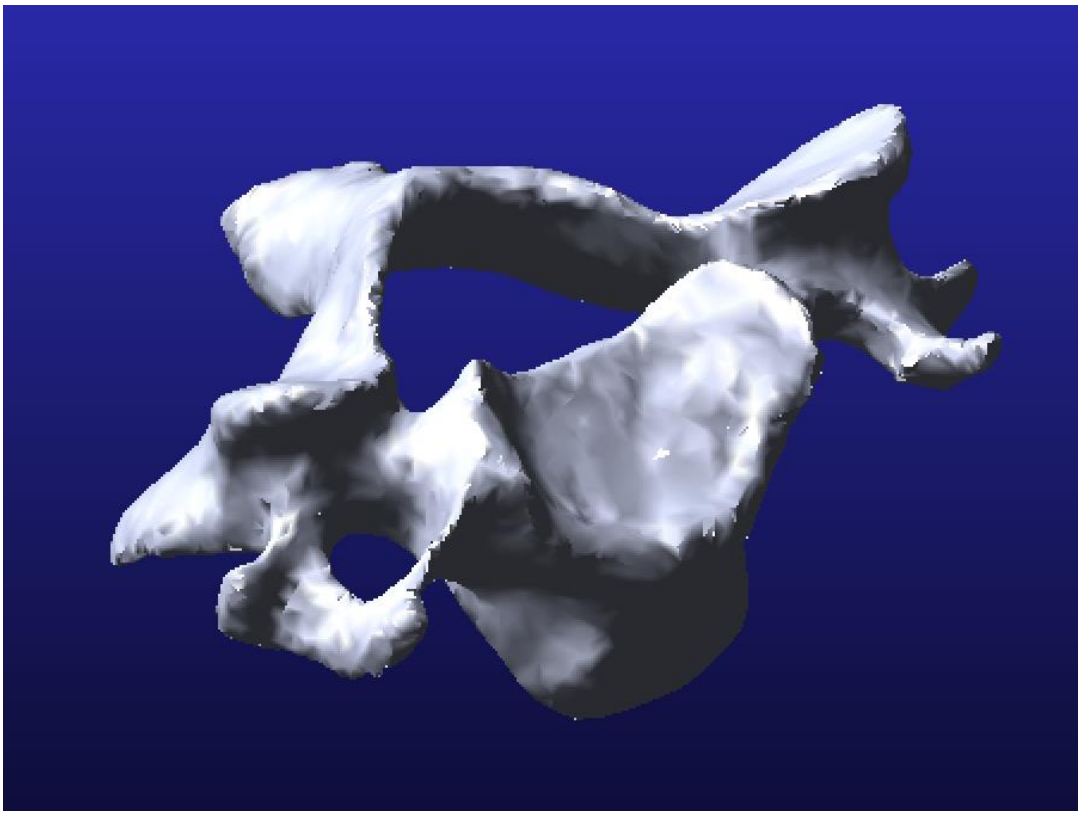

Figure 6: C4 vertebral geometry [23]

This geometry was obtained from a CT scan and imported into MSC Adams. The masses of the vertebrae from this CT model are shown in Table 2.

Table 2: Mass of cervical vertebrae [23]

Segment	Mass (g)
C1	26.59
C2	26.95
C3	18.44
C4	15.24
C5	15.05
C6	17.95
C7	25.29
Average	20.79

It is also clear to see that the geometry is very complex, making it difficult to machine with accuracy. Because of this barrier, a new vertebral geometry was designed and is explained in the next chapter.

Table 3 shows the masses of vertebral bodies of a large sample size of subjects, in order to better represent the population [20].

Table 3: Mass of cervical vertebrae [20]

Segment	Mass (g)
C1	7.6 ± 1.3
C2	8.3 ± 1.4
C3	4.9 ± 1.0
C4	5.2 ± 0.9
C5	5.4 ± 0.9
C6	5.8 ± 1.1
C7	6.6 ± 1.2
Average	6.3 ± 3.0

A reason for the significant difference in average vertebral mass between the CT specimen and the study could be contributed to the presence of additional soft tissue. When considering the total mass of the neck, described earlier as being 1.5 kg, it becomes clear that the soft tissue contributes a great deal to the overall mass. However, in general, cervical vertebrae are very light and durable.

2.3 Ligaments

The neck is a very complex structure with equally complex kinematics. The kinematics in the neck are guided and constrained by intervertebral discs and ligaments. Intervertebral discs are cartilaginous joints that exist between pairs of vertebrae to act as shock absorbers and multi-degree-of-freedom kinematic joints. These discs permit translation and rotation about all three principal axes. When looking further into the anatomy of the neck and cervical spine, it becomes clear that ligaments play an arguably more prominent role in controlling neck kinematics. Figures 7-9 illustrate locations of ligaments of the cervical spine.

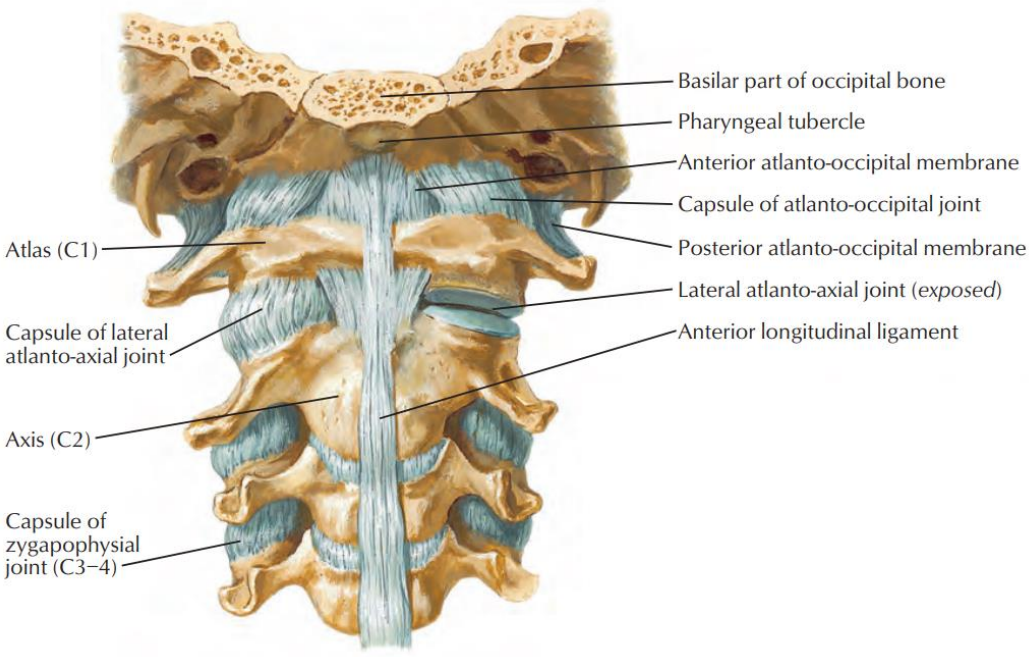

Figure 7: Anterior view of the cervical spine and soft tissue [18]

In the anterior view of the cervical spine, the anterior longitudinal ligament is prominent, with the intervertebral discs being shown on either side. This longitudinal ligament travels down the length of the cervical spine and provides stability to the structure while controlling flexion and extension kinematics. A posterior view of the cervical spine can be seen in Figure 8.

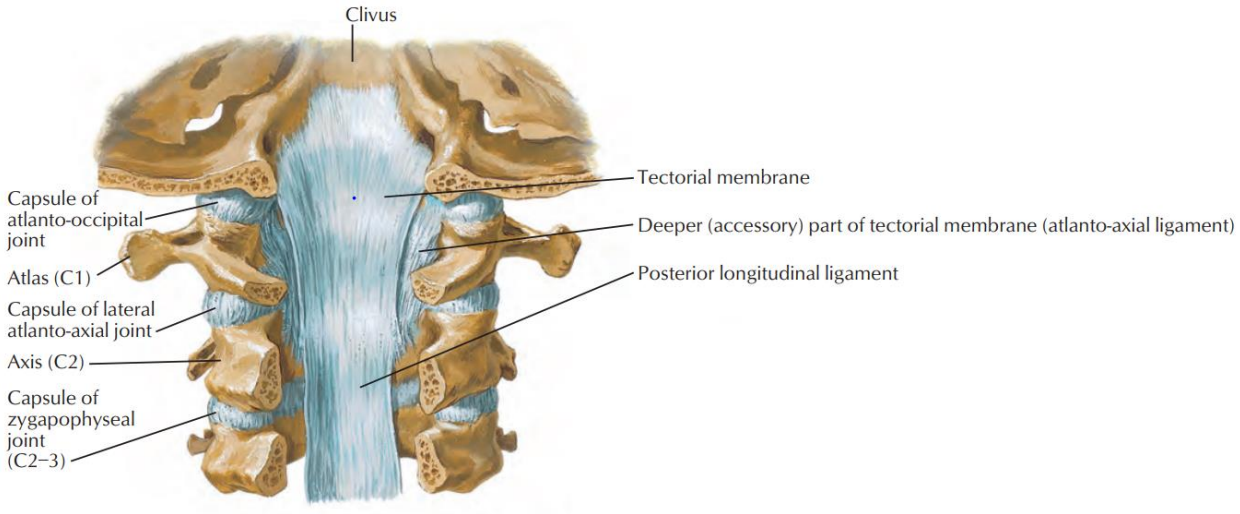

Figure 8: Posterior view of the cervical spine and soft tissue [18]

The posterior longitudinal ligament lies opposite of the anterior longitudinal ligament with respect to the anatomy of the cervical spine. It provides the same function as the anterior longitudinal ligament. There are additional ligamentous structures that affect the kinematics of pairs of vertebrae relative to each other. These ligaments can be seen in the Figure 9.

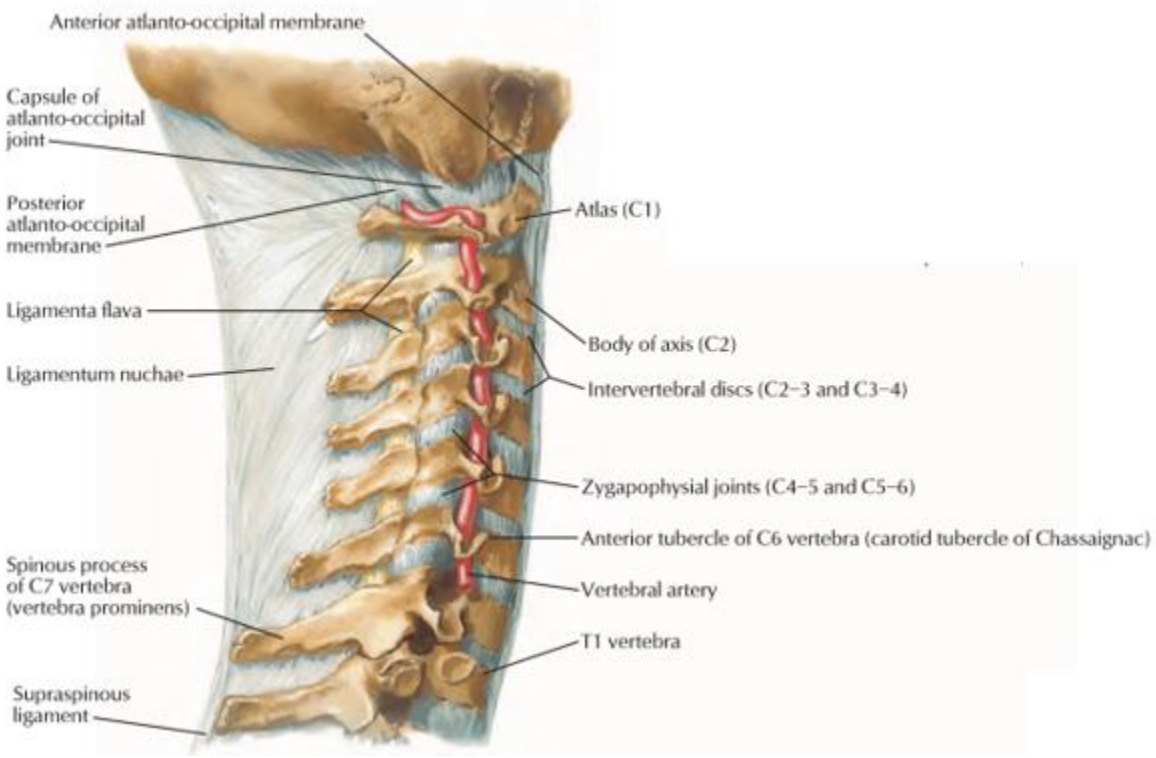

Figure 9: Right lateral view of neck cross-section with ligaments [18]

The supraspinous ligament and the ligamenta flava both have the function of supporting vertebral pairs and affecting their kinematics. Also, interspinous ligaments lie beyond the ligamenta flava and perform the same function.

Actual neck ligaments in the human neck are not a prominent factor in the design for this or any ATD neck. However, understanding the position and function of important neck ligaments can help to characterize how the neck's kinematics are controlled. For this specific study, the main contributors of neck kinematics are the posterior and anterior longitudinal

ligaments, the inter and supraspinous ligaments, the ligamenta flava, and the posterior and anterior occipital membranes.

When considering ligaments and their contribution to head and neck kinematics, it is important to consider the stiffness and damping properties of the soft structures. Dauvilliers et al. also concluded that the damping coefficient of the neck is equal to 2 $\frac{Ns}{mm}$ [24]. Ligamentous stiffness has been investigated by many studies and findings have generally shown that this stiffness varies depending on the ligament, which is sensible when considering that every ligament has varying properties, such as length and cross-sectional area. The stiffness of ligaments of interest in the lower cervical spine were quantified in the Table 4.

Table 4: Stiffness of selected ligaments in lower cervical spine (T1 to C2) [16]

Ligament	Reported Stiffness
Anterior Longitudinal Ligament	16.7 ± 2.7
Posterior Longitudinal Ligament	25.4 ± 7.2
Interspineous Ligament	7.74 ± 1.61
Supraspineous Ligament	-
Ligamenta Flava	25 ± 7.04

The findings come from Yoganandan et al., who characterized ligament stiffness from their individual loading response [16]. Yoganandan had another study to characterize the stiffness of ligaments in the upper cervical spine, and these stiffness values are reported in Table 5.

Table 5: Stiffness of selected ligaments in upper cervical spine (C2 to skull base) [34]

Ligament	Reported Stiffness
Anterior Atlanto-Occipital Membrane	16.9 ± 3.2
Posterior Atlanto-Occipital Membrane	5.7 ± 0.4
Ligamenta Flava	11.6 ± 11.0
Anterior Longitudinal Ligament	24.0 ± 11.7

The stiffness and damping properties of these ligaments will become important when modeling the neck using a multibody dynamics software.

Chapter 3: Design and Modeling

3.1 Initial Design Decisions

The design for the new neck utilized many features, ones that were either inspired by the human anatomy, inspired by previous literature, or incorporated ideas that were novel. The cervical spine in a living person consists of seven vertebrae. Consequentially, a biofidelic, mechanical neck should include the same number of vertebrae. This material should resemble bone, both being lightweight and machinable enough to mimic the geometry of a cervical vertebra. Both the mass of the neck and the distance between T1 and the occipital joint should be similar to that of the human cervical spine. Constraints of the design include having the ability to attach a Hybrid III head to C1 and attaching the bottom of the neck to a six-axis load cell placed on the sliding head and neck fixture used to validate the biofidelity of the physical model. All computer aided design for the final neck design prior to simulation was done using Autodesk Inventor (Autodesk Inc., San Rafael, CA).

3.2 Final Design Features

A final prototype, consisting of seven cervical vertebrae and one thoracic vertebra, was constructed. The vertebrae are aluminum, which serves as a lightweight, durable, and easily machinable material. Since aluminum possesses these traits, it can be considered similar to bone for this purpose. Since a more biofidelic neck would have multiple degrees of freedom between pairs of vertebrae, spherical joints were used in place of the revolute joints seen in the BioRID II. This allows three degrees of freedom, rotation about the x, y, and z, between each vertebra from T1 to C2. Figure 10 shows the model of the full design, while Figure 11 shows the spherical joints between each vertebral pair.

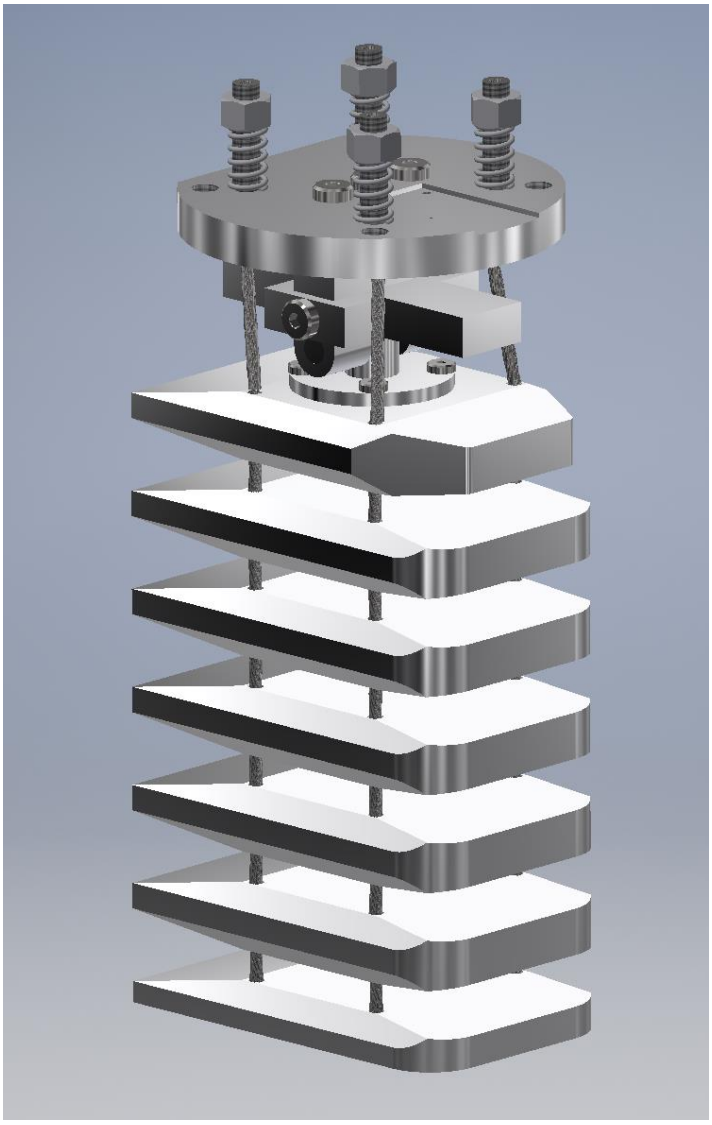

Figure 10: Overall neck design

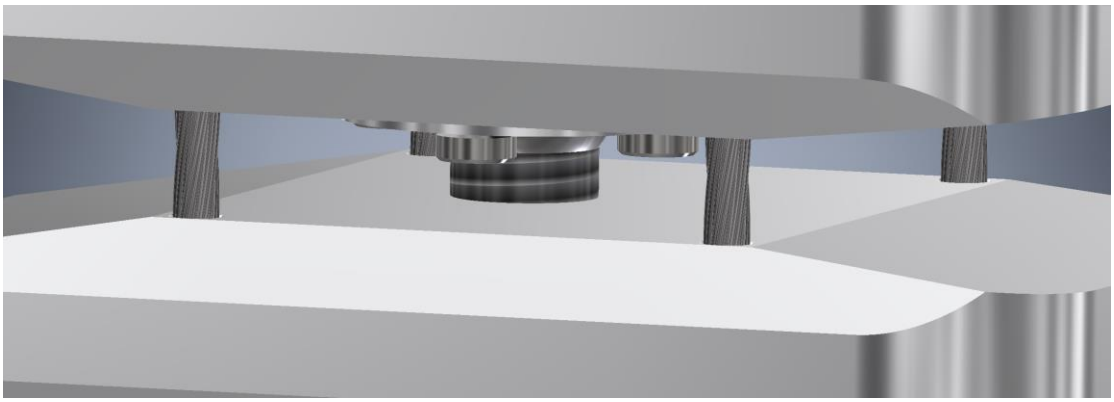

Figure 11: Spherical joints used between each vertebral pair

Because the vertebral geometry was so complex, simplifications were made to the machined vertebrae. An individual vertebra can be seen in the Figures 12 and 13.

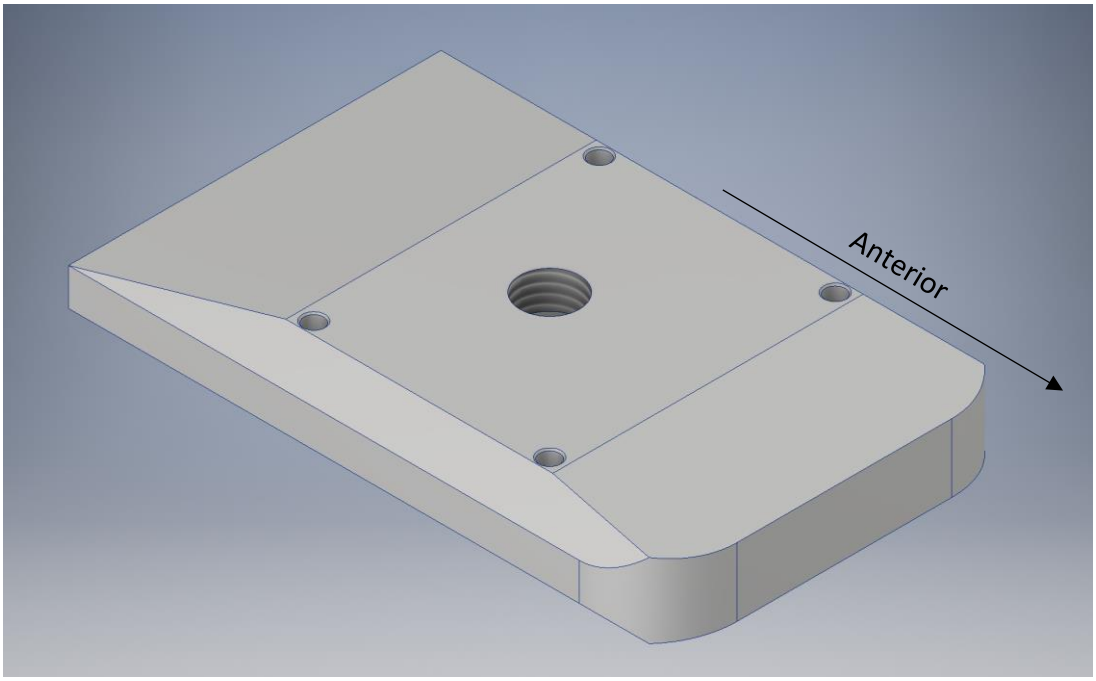

Figure 12: Upper isometric view of vertebral design (C7)

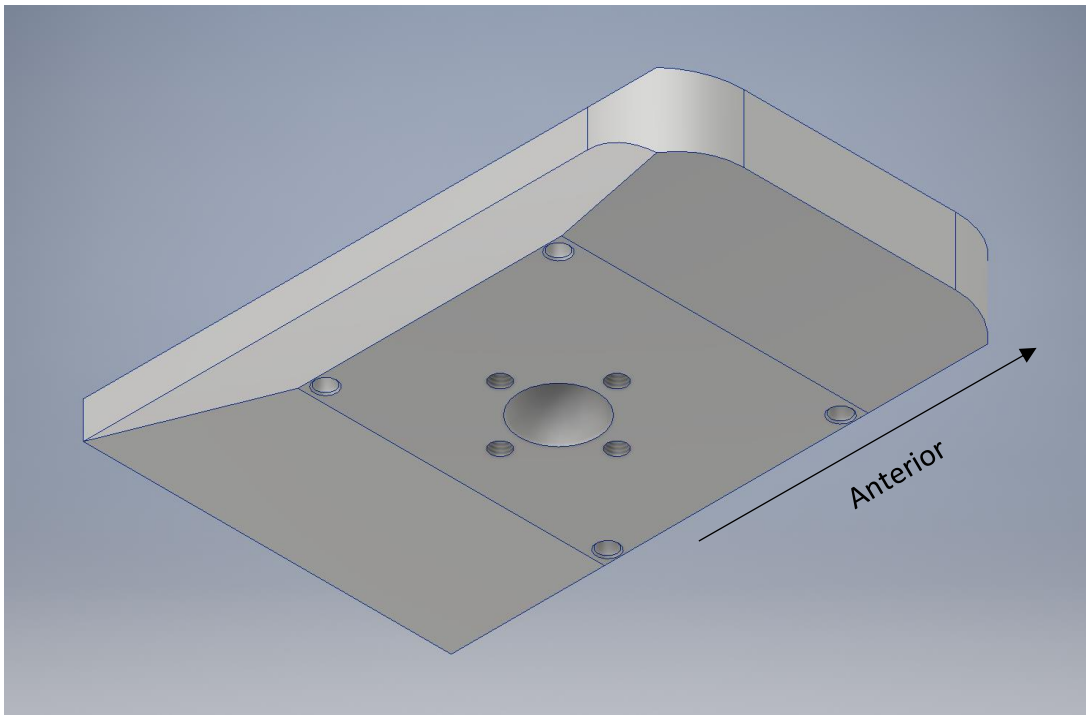

Figure 13: Lower isometric view of vertebral design (C7)

The geometry was simplified by modifying design features of human vertebrae with features that perform the same function. Anterior and posterior rotation was permitted by adding a deep chamfer to the anterior and posterior section of the vertebrae. Lateral rotation was permitted by adding a smaller chamfer to each side of the vertebrae. Since there is no spinal cord, the center of the vertebral body was kept solid except for the hold patterns needed to mate each pair of vertebrae. The vertebrae (C7-C2) have a length of 95 mm, width of 60 mm, and a thickness of 16 mm (for engineering drawings, see Appendix A), which is similar when considering the average dimensions of a cervical vertebra. Each vertebra has a mass of 197.86 grams (with the exception of C2 and T1, which are 183.87 and 126.93 g, respectively), which is much heavier than a human vertebra.

The mating between C2 and C1 consists of a revolute joint about the vertical, as seen in the human cervical spine. Attached to this revolute joint is the lower portion of the occipital joint. The occipital joint permits one degree of rotation about the horizontal axis and serves to rigidly join C1 and the base of the skull, which was fitted to the Hybrid III head. This provides humanlike kinematics between C1 and the base of the skull. Figure 14 shows this assembly.

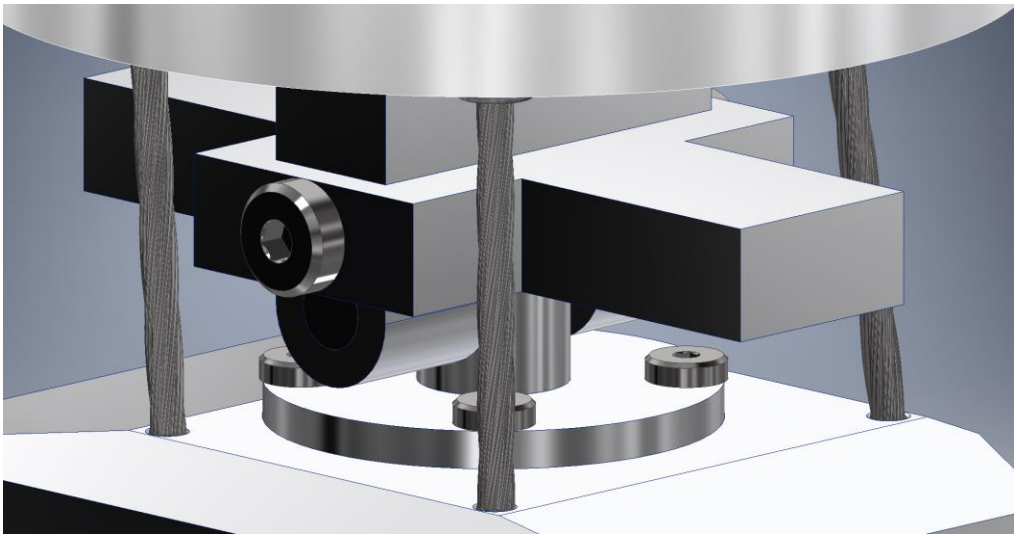

Figure 14: C1 and occipital joint

The neck also features four sets of wire rope, two anterior and two posterior to the intervertebral spherical joints. These wire ropes resist excessive rotation and provide axial support of the neck, giving it a stable structure when held static. A combination of a threaded rod and nuts connect the threaded rod to the skull base, allowing for fine adjustment of the stiffness of these cables to control the kinematics of the neck. These mechanisms can also be used to control the static curvature of the neck and the movement of the physical model during experimentation. Figure 15 shows this mechanism.

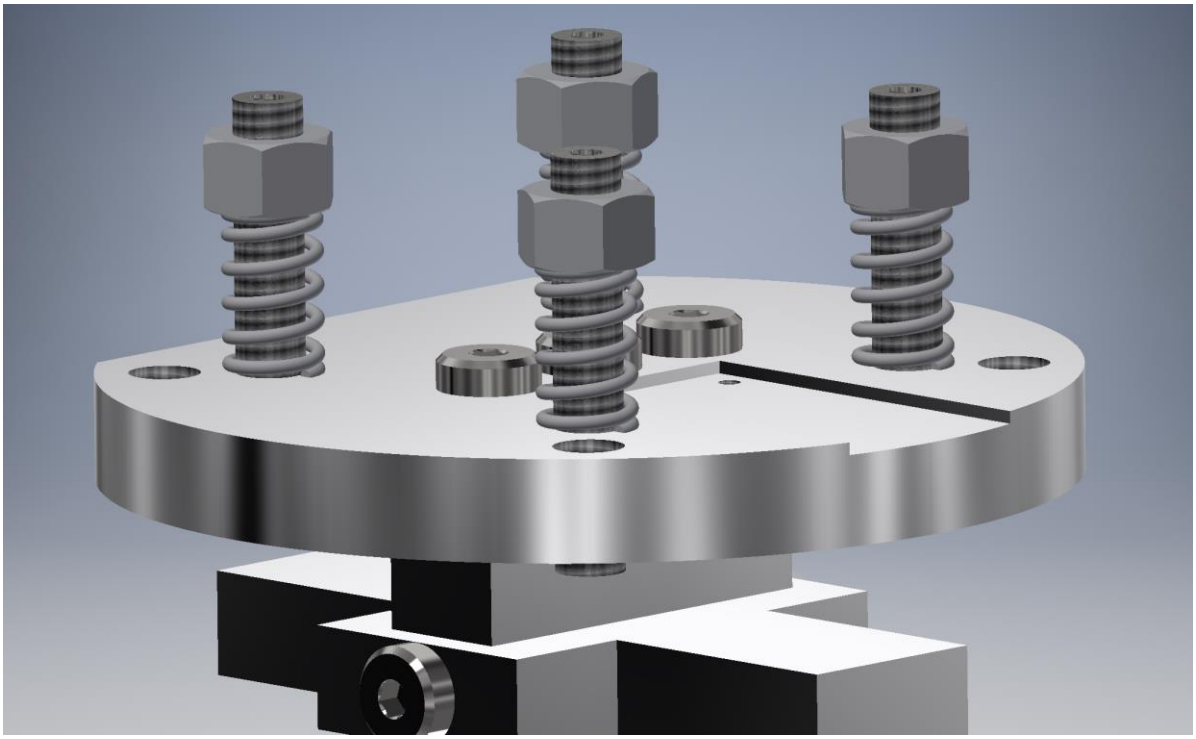

Figure 15: Hybrid III skull base

The skull base acts as a connection of the neck to the Hybrid III head. The head stores the rope adjustment mechanisms that rise from the skull base. These mechanisms house compression springs that allow for control over the stiffness of the four wire ropes. Additionally, three accelerometers and three angular rate sensors (6DX Pro, DTS, Seal Beach, CA) were placed at the center of gravity of the head, which was accounted for when designing its mounting holes in

the base of the skull.

The final design has a mass of 1.726 kg, which is nearly the same mass as that of the human neck with soft tissue still attached (1.5 ± 0.1 kg) from a previous PMHS rear impact study mentioned in Chapter 2 [8]. When excluding T1, the mass is 1.599 kg, which is even more similar. Although the individual vertebrae are much heavier in the designed neck in comparison to a human neck, the change in mass can be corrected for when choosing the stiffness of polymer materials to dampen the neck's movement. When choosing polymer components, stiffer components would be more appropriate for a heavier neck. Additionally, the distance between C7 and the occipital joint is 136.2 mm, which is a larger distance than the same measurement in the BioRID II (115.2 mm), but a smaller distance than the measure in the Hybrid III (143.6 mm) [3] [25].

3.3 Modeling Software

The neck design had to be validated on a preliminary level prior to fabrication and physical testing. For this purpose, a commercial multibody dynamics software (ADAMS, MSC Software, Newport Beach, CA) was used. ADAMS allows for accurate simulation of highly nonlinear kinematics, making use of specific material and part properties in combination with mechanical elements created in the program. It is the software of choice for this project because the focus is on the kinematics of the ATD neck design in response to a kinematic input.

The objective of the simulation is to validate the kinematics of the neck design against the PMHS neck kinematics of another rear impact study [28]. The program will make use of imported geometries and mechanical components, such as spring dampers and revolute joints, to make a realistic model. Since the kinematics of the model neck are controlled entirely by spring dampers, the stiffness and damping coefficients will be variables that control the neck

kinematics. Making use of optimizations, utilizing a generalized reduced gradient method (GRG) with an objective function, will identify the values of these variables that make the model neck response closest to the PMHS response. The resulting stiffness and damping information from the virtual optimization will then be transposed to the physical model. Ideally, the model neck will have the same response as the PMHS study. However, this is not a realistic goal, so a corridor will be used to characterize the model's response in comparison to the PMHS study.

3.4 MSC ADAMS Simulation and Response

To simulate a realistic motion seen in a rear impact, a displacement and rotation spline, resulting from an input in the previous PMHS rear impact study, was used [28]. The input can be seen in Figure 16.

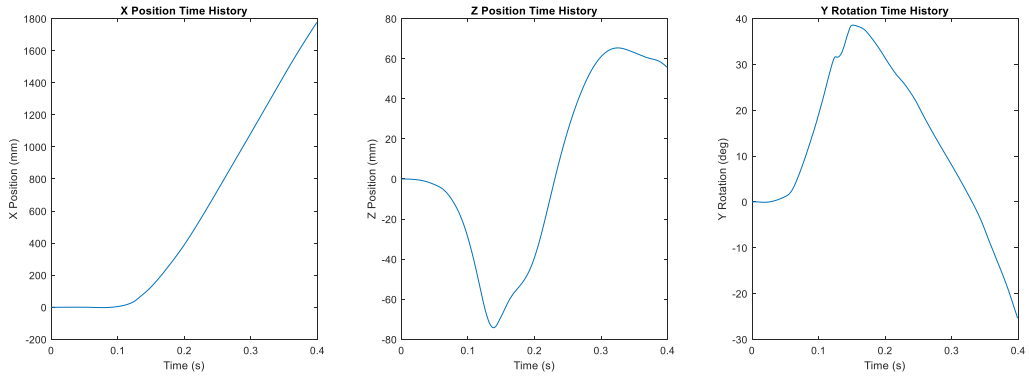

Figure 16: Displacement and rotation applied by input

These input pulses were the resultant kinematics of the T1 vertebrae during the rear impact simulated in the previous PMHS study. The inputs shown above were according to SAE J211 which is seen in Figure 17.

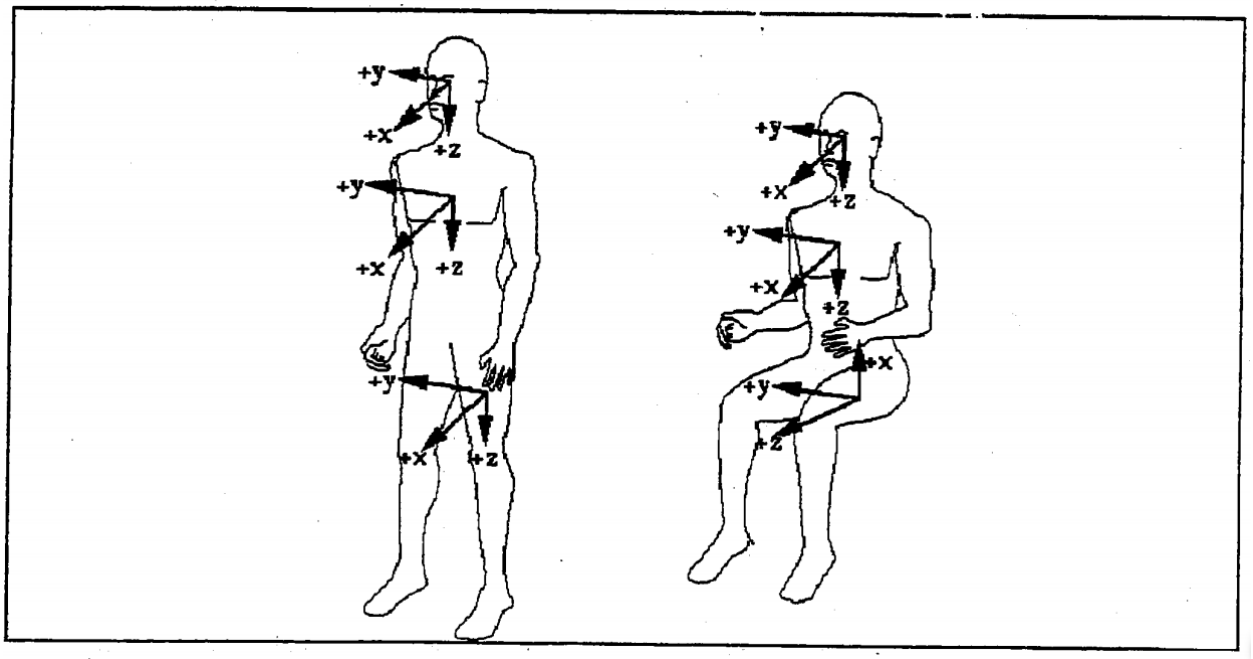

Figure 17: SAE J211 physical coordinate system orientation used [33]

SAE J211 is the standard coordinate system for automotive biomechanics testing and will be used throughout the duration of this thesis.

When performing analysis using ADAMS, corridors consisting of the mean PMHS response from the previous study were used [28]. The response of the model neck will be compared to the study's entire corridor, including the upper and lower standard deviation, after simulation. The corridors can be seen in Figures 18-21.

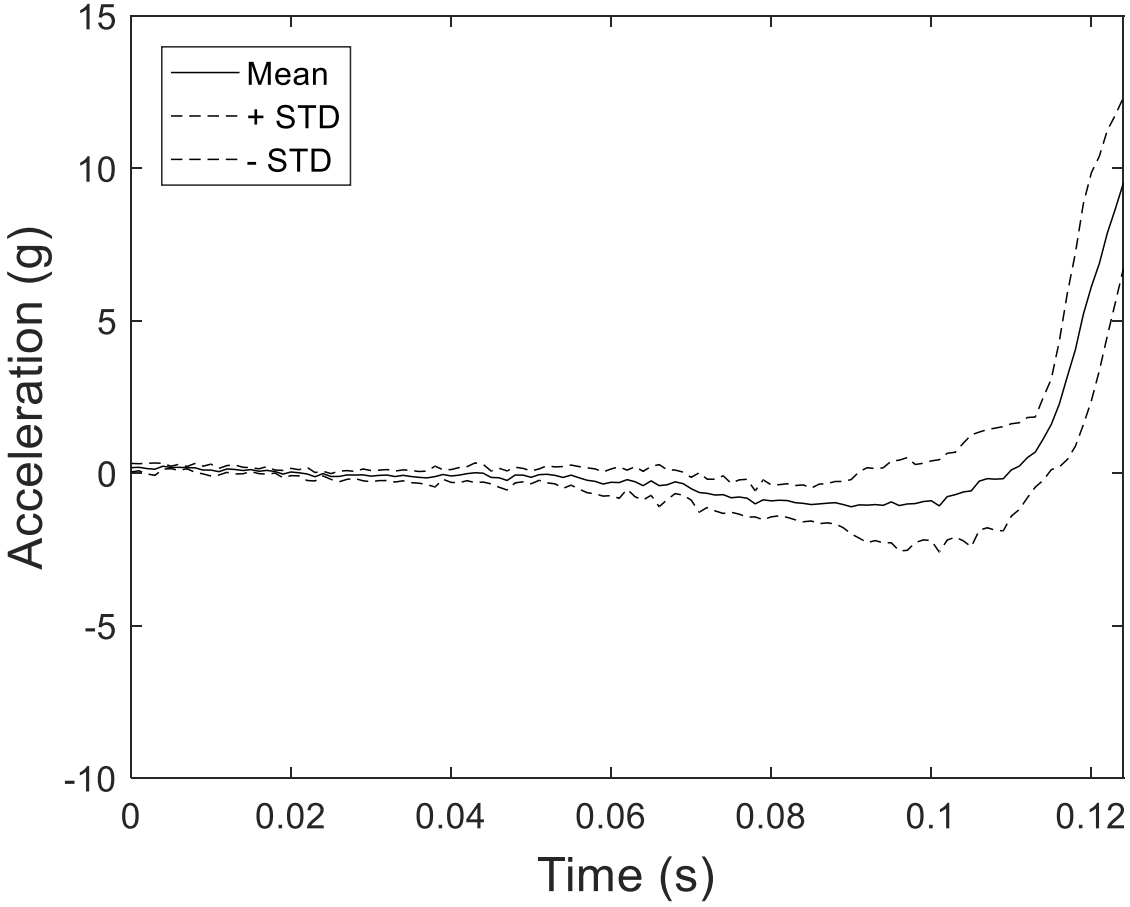

Figure 18: X acceleration PMHS corridor [28]

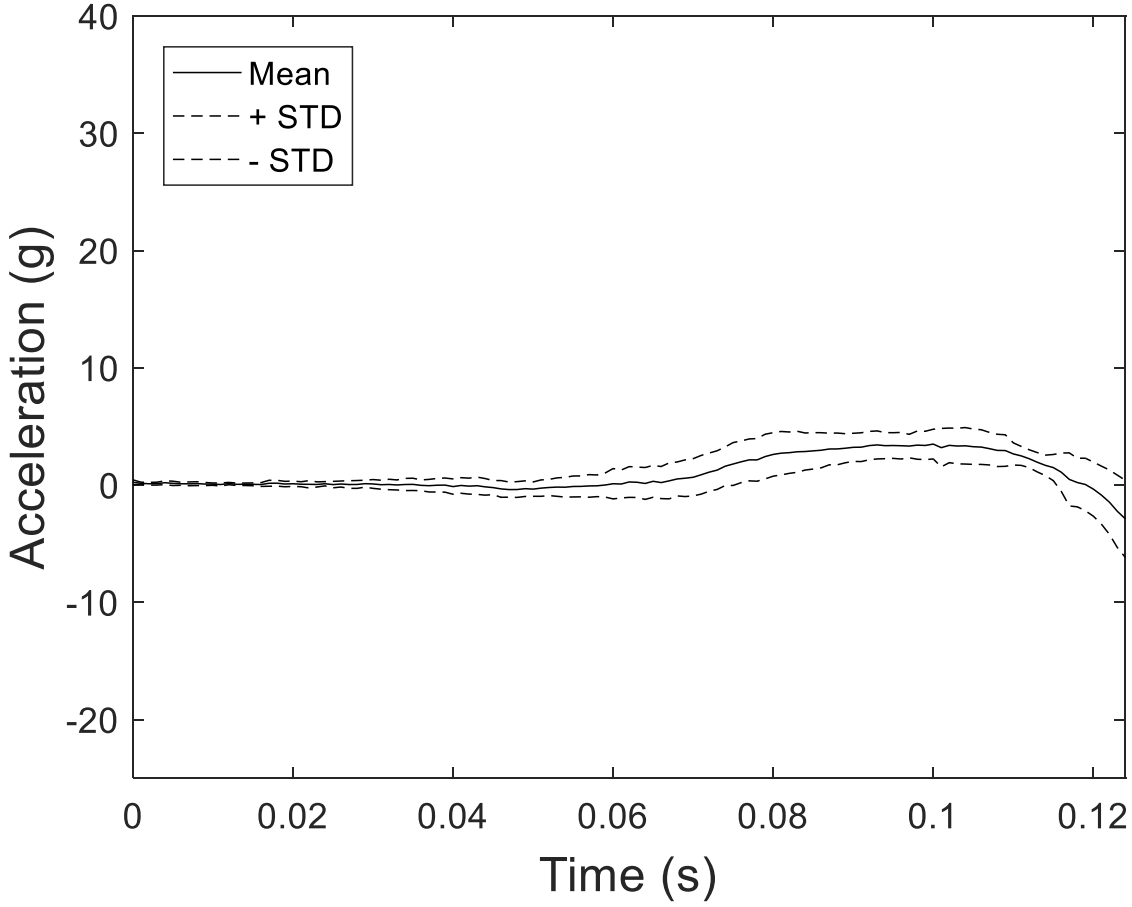

Figure 19: Z acceleration PMHS corridor [28]

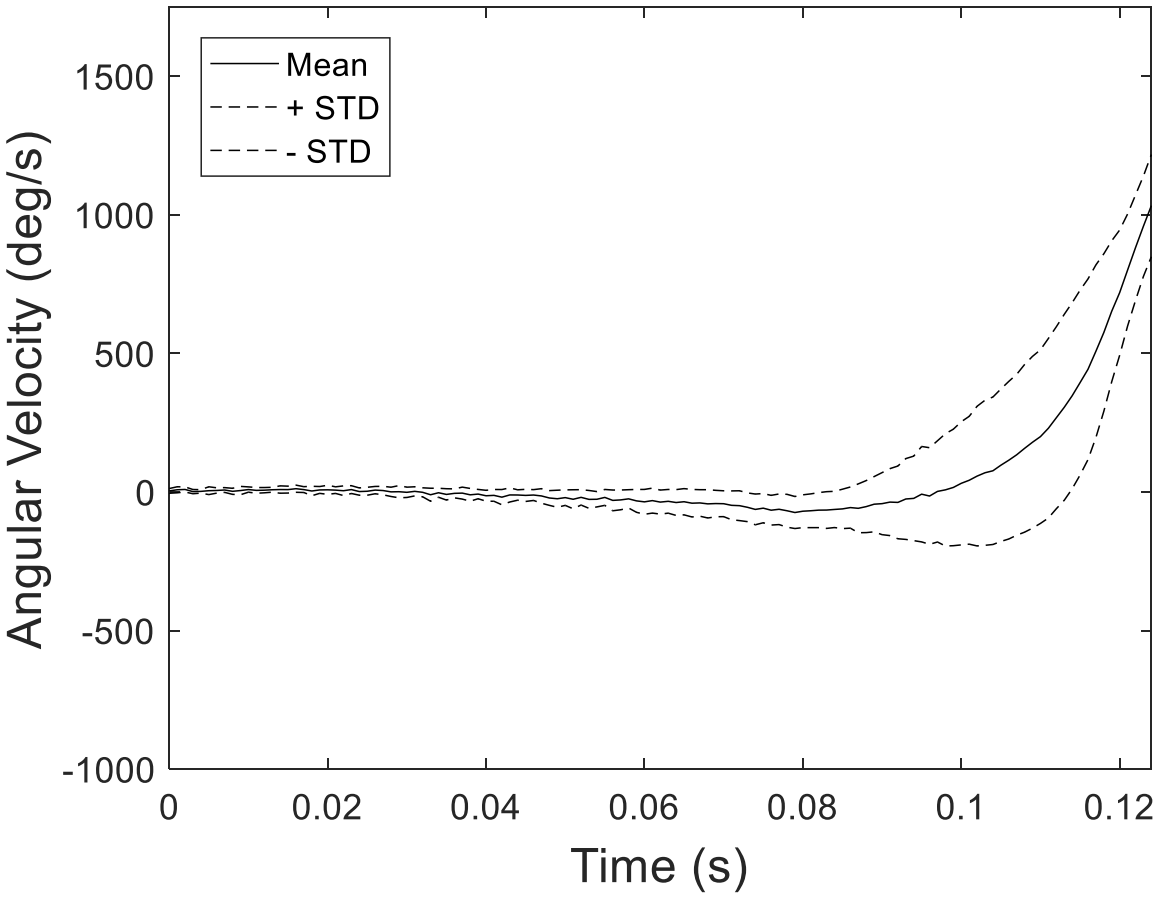

Figure 20: Y angular velocity PMHS corridor [28]

3.4.A CT Model

In a previous study, a CT model of a PMHS subject was created and imported to ADAMS with the intention to replicate a low speed rear impact head and neck response [23]. A similar method of utilizing spring dampers to represent ligaments and control the kinematics of the neck was used. The model can be seen in Figure 21.

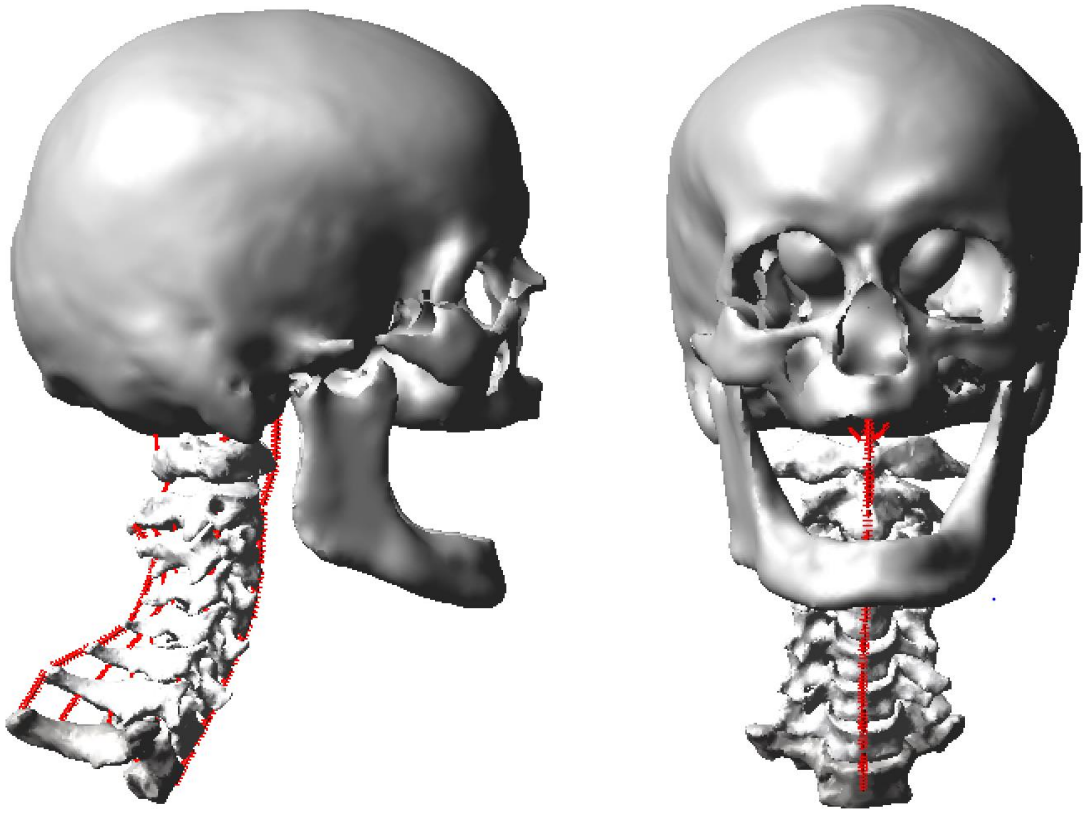

Figure 21: CT model with spring dampers [23]

Five spring dampers were placed in between vertebral pairs, with three lying posterior to the spinal cord and two on the anterior side. The input conditions mentioned earlier were applied to the T1 vertebrae. The response of this system and the average PMHS response were downsampled to 1,000 Hz from 20,000 Hz and compared. These results can be seen in Figures 22-24.

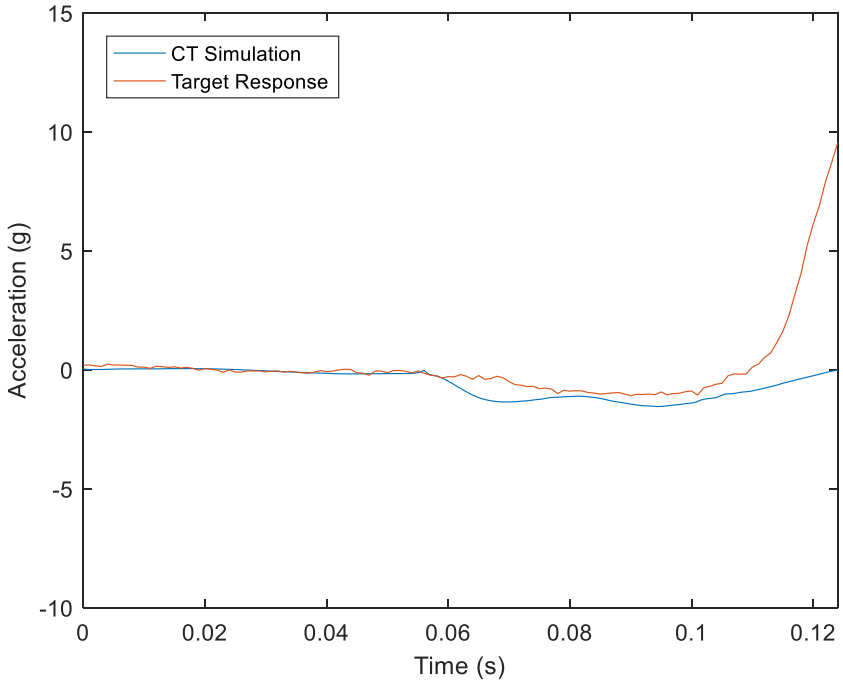

Figure 22: CT model X acceleration against representative PMHS response

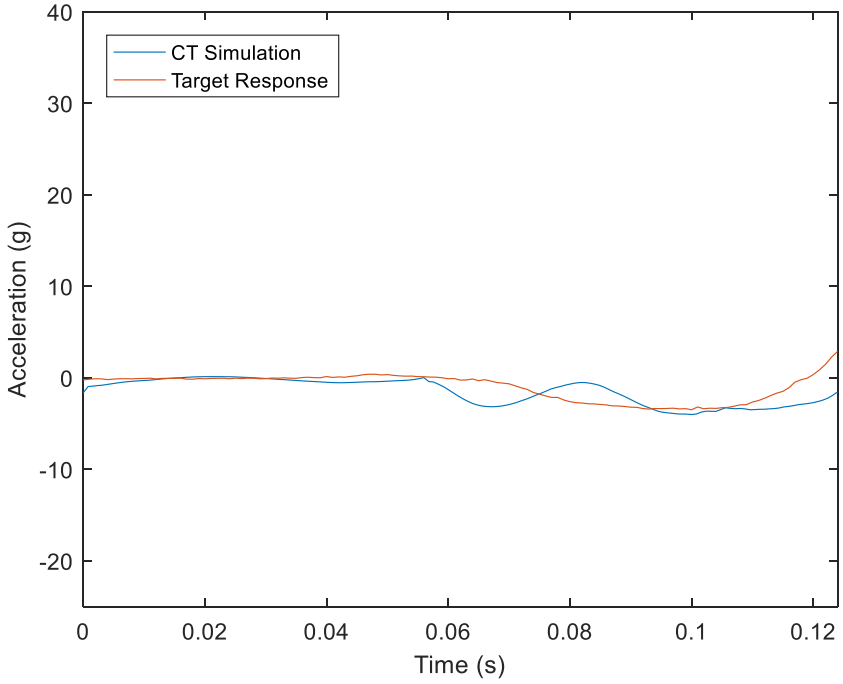

Figure 23: CT model Z acceleration against representative PMHS response

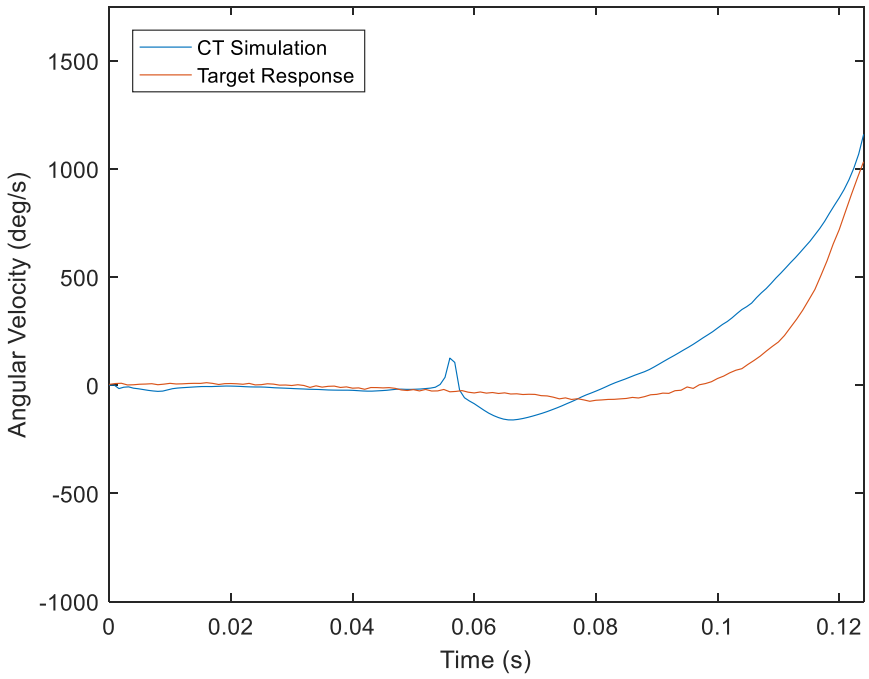

Figure 24: CT model angular velocity about Y against representative PMHS response

The model does fairly well in following the trends of the experimental acceleration data from the previous study. The event time of 0.124 seconds, as previously mentioned, is due to the contact of the head with the rigid seatback after 0.124 seconds in the experiment [28]. The event ends here because the kinematics are no longer solely a function of the ATD head and neck.

3.4.B Base Model

The CAD model of the new ATD neck design was imported into ADAMS for preliminary analysis. All solid bodies, including the vertebrae, components of the occipital joint, and skull were used. The mass and inertia relative to the center of gravity of these parts were accounted for prior to analysis. The spherical joints located between each pair of vertebrae were modeling using abstract connections of the same kind at identical locations. Revolute joints about their respective axes were used to connect C2 to C1 and C1 to the occipital. Figure 25 shows this virtual model.

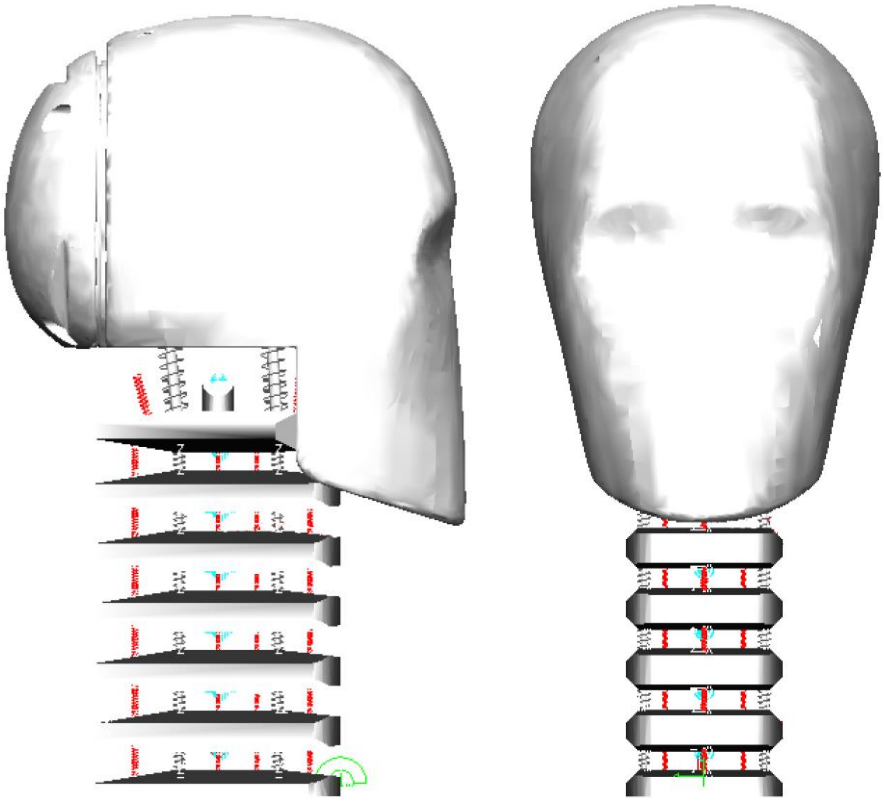

Figure 25: Base model with spring dampers

Polymer stiffness components that were designed into the physical model were represented using spring dampers in the same location. Initially, two spring dampers were placed anteriorly and posteriorly to the spherical joint, respectively. One of these pairs had the primary function of controlling neck flexion and extension, while the other pair prevented contact between the anterior and posterior angled surfaces between vertebrae. Two spring dampers were also placed lateral to the spherical joints, having one on each side. Spring configurations between main vertebral bodies can be observed in Figure 26.

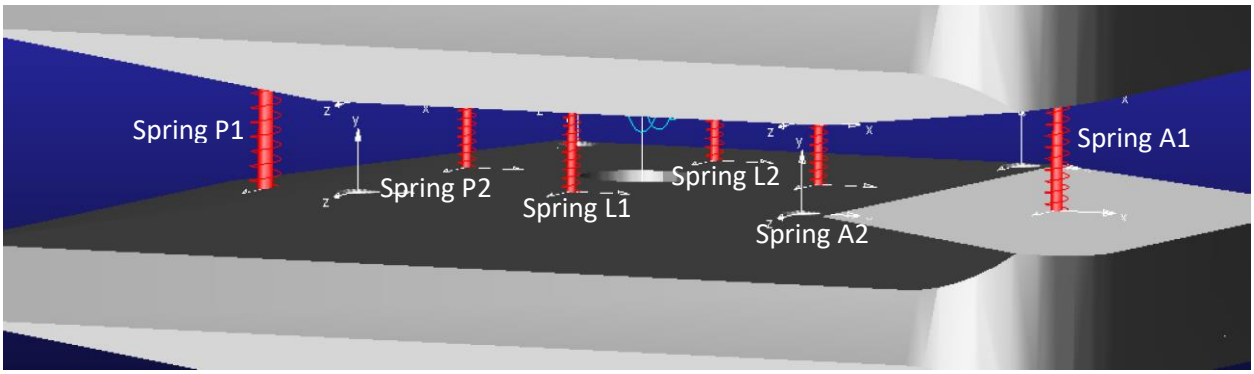

Figure 26: Intervertebral spring damper placement

The springs beginning with a ‘P’ represent the posterior springs, while those starting with an ‘L’ or ‘A’ represent the lateral and anterior springs, respectively. The objective of this study is to provide the ability of lateral and other types of neck movement, but only to validate neck flexion and extension response in a low-speed rear impact, so the two lateral springs will be largely ignored. The spring configurations characterizing the movement of the skull with respect to C2 can be seen in Figure 27.

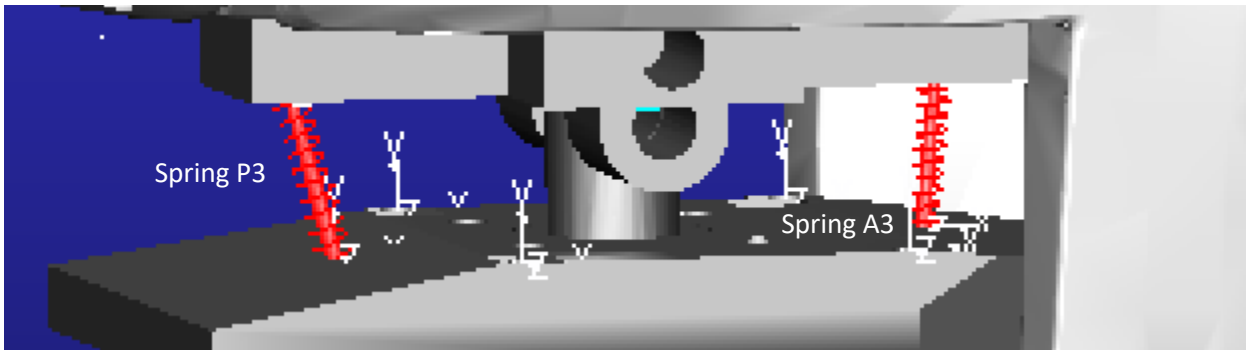

Figure 27: Intervertebral spring damper placement

Only two spring dampers, one anterior and one posterior (P3 and A3), were used to control the rotation of C1 relative to C2. To model the wire ropes that support the cervical spine from the base of T1 to the base of the skull, one-way spring dampers were used. These were used to simulate the stiffness in tension of a wire rope while not allowing for a force to develop in compression. When added to the virtual model, its locations can be seen in Figures 28 and 29.

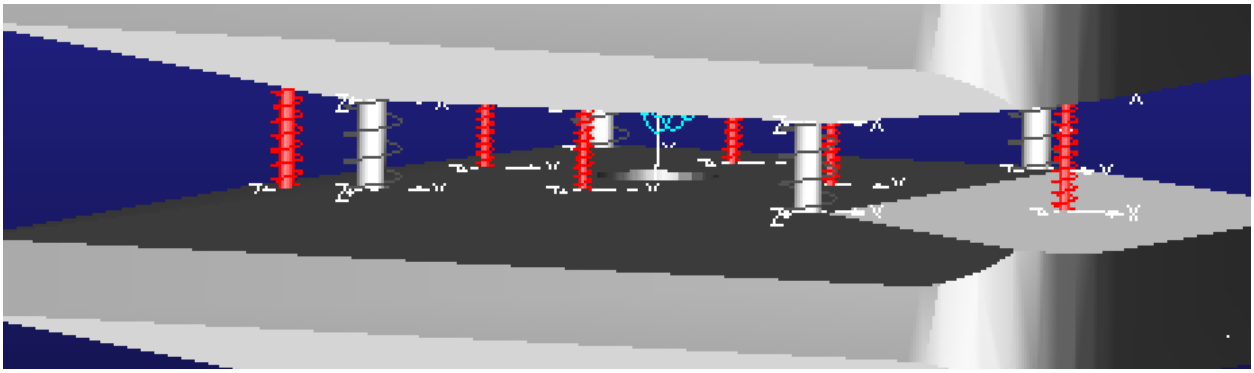

Figure 28: Intervertebral spring damper placement with wire rope mechanisms

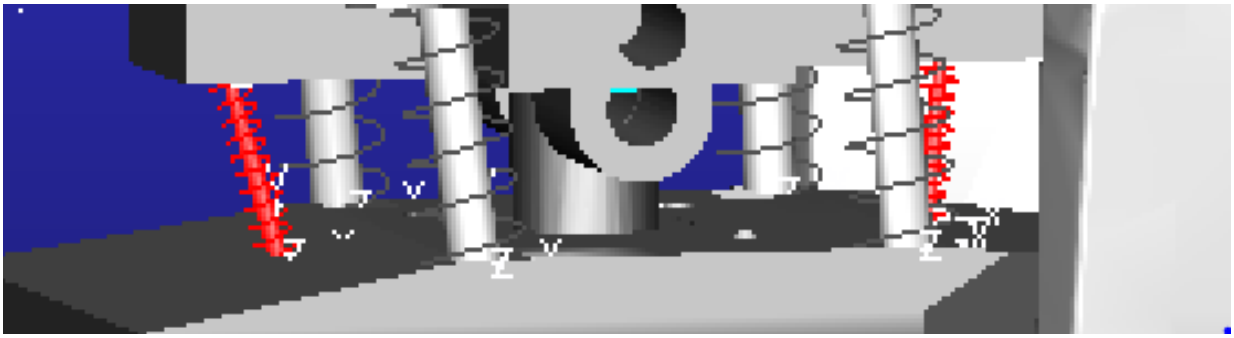

Figure 29: Intervertebral spring damper placement with wire rope mechanisms in upper cervical spine

The stiffness function of the one-way spring dampers that represented the wire ropes was modeled in three phases. For forces of compression, the deflection of the rope was taken to be infinite. For forces of tension, up to the force that the springs used on the skill base bottom out, the stiffness of the respective springs was used. For positive forces greater than this bottoming out force, the stiffness of the wire rope was used and calculated from the following equation (1).

(1) $$k = \frac{AE}{L}$$

$$where\ d_r = \frac{1}{8}\ in\ ,$$

$$A = 0.384 d_r^2\ ,$$

$$L = 149.5\ mm\ ,$$

$$and\ E = 11.7 \times 10^6\ MPa$$

Values for approximation of the stiffness were taken from previous experimental approximations [19]. The stiffness of the rope is orders of magnitude greater than the stiffness of the spring. Figure 30 shows a plot of deflection and force applied characterizes the stiffness of the wire rope in the model.

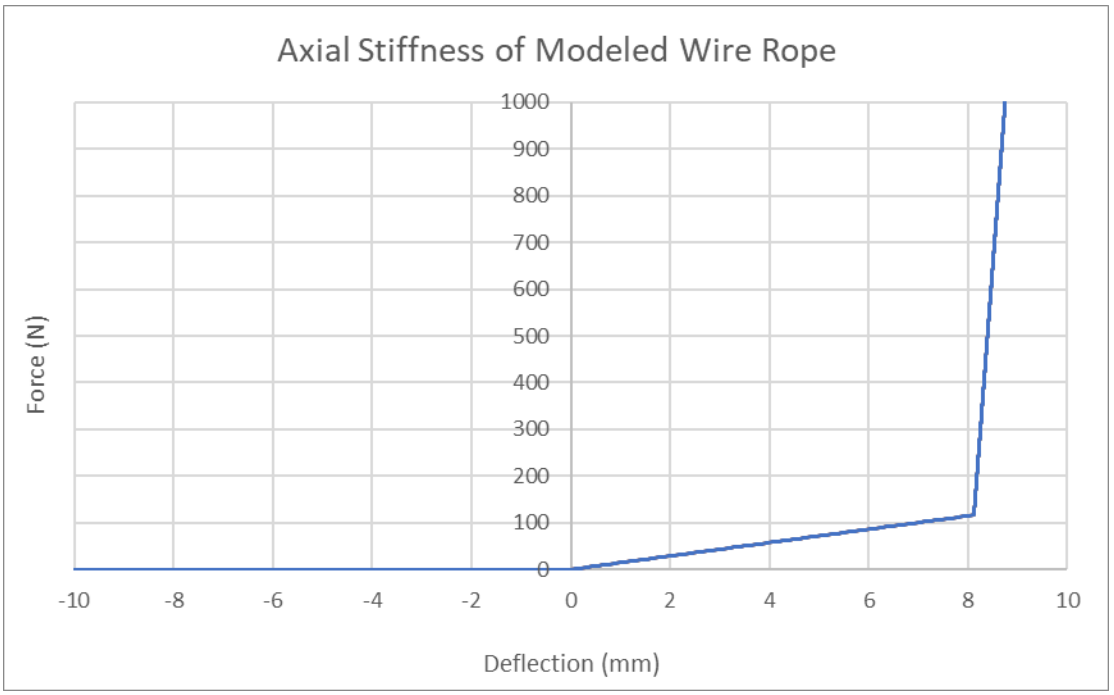

Figure 30: Stiffness function used to describe wire rope

When choosing initial values for the spring stiffness, stiffness and damping properties for cervical ligaments discussed in Chapter 2 were considered. Firstly, for every spring damper, the damping coefficient was set to a constant 2 $\frac{Ns}{mm}$. When selecting stiffnesses for the springs, an initial guess was taken for the scaling factor based on the average mass of the CT model vertebrae and the vertebrae from literature [23] [20]. This initial guess was scaled by a factor of 15, because the mass of a single aluminum vertebrae (197.86 g) was about fifteen times greater than the average vertebral mass of the two combined studies (13.55 g). Stiffness values used in this base model can be seen in Tables 6 and 7.

Table 6: Stiffness of model springs in comparison to equivalent ligaments in lower cervical spine (T1 to C2) [16]

Ligament	Reported Stiffness	Base Model Stiffness	Spring
Anterior Longitudinal Ligament	16.7 ± 2.7	16.7 × 15	A1
Posterior Longitudinal Ligament	25.4 ± 7.2	25.4 × 15	P1
Interspineous Ligament	7.74 ± 1.61	7.74 × 15	P2
Supraspineous Ligament	-	7.74 × 15	P1
Ligamenta Flava	25 ± 7.04	25 × 15	P2

Table 7: Stiffness of model springs in comparison to equivalent ligaments in upper cervical spine (C2 to skull base) [34]

Ligament	Reported Stiffness	Base Model Stiffness	Spring
Anterior Atlanto-Occipital Membrane	16.9 ± 3.2	16.9 × 15	A3
Posterior Atlanto-Occipital Membrane	5.7 ± 0.4	5.7 × 15	P3
Ligamenta Flava	11.6 ± 11.0	11.6 × 15	P3
Anterior Longitudinal Ligament	24.0 ± 11.7	24 × 15	A3

It should be noted that not all the springs seen in the model were used during every simulation. Because neck flexion is the primary response expected to be seen during the event, it is only necessary to activate only the anterior or posterior springs in the model prior to the simulation. The posterior springs consist of P1, P2, and P3, which are meant to represent the posterior longitudinal ligament, interspinous ligament, supraspinous ligament, and ligamenta flava. When using only the anterior springs, only springs A1 and A were used, representing the contribution of the anterior longitudinal ligament and the anterior atlanto-occipital membrane.

When simulating the neck, it is important to provide the most realistic loading patterns. It was determined visually that only the posterior springs provided the most realistic neck response when activated. This can be attributed to the unstable behavior of the neck during trials where only the anterior springs were activated. The difference between the two simulations can be seen in Figures 31 and 32.

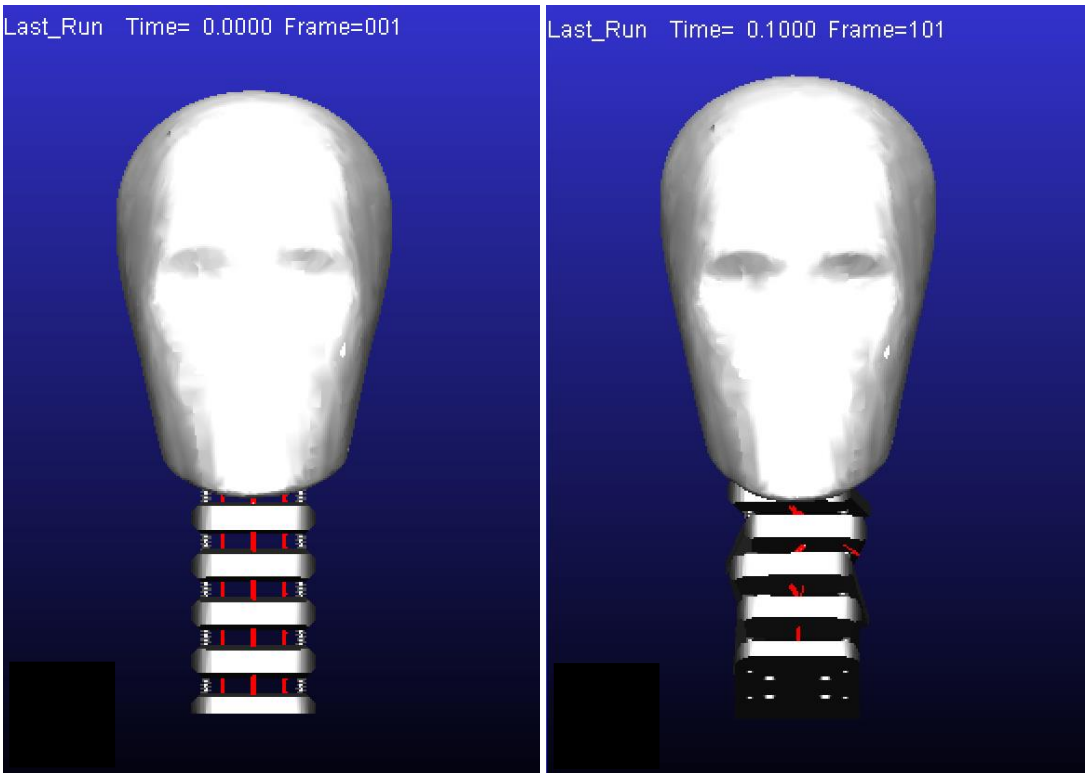

Figure 31: Stills of anterior only spring simulation with the base model

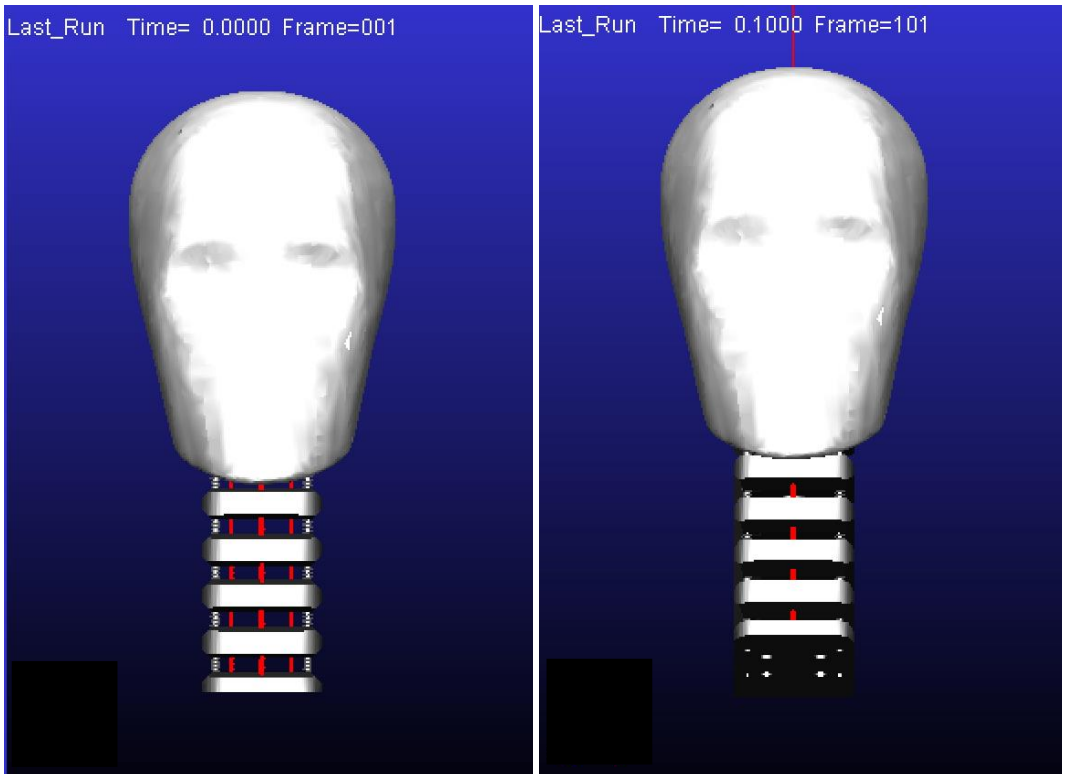

Figure 32: Stills of posterior only spring simulation with the base model

It is clear from the simulation that the model with only the posterior springs activated will give the most desirable response, the response being one that is realistic to how the physical model may respond. This is because the animation of the model with the posterior springs activated saw less rotation of vertebral bodies, which is prominent in the anterior spring model.

The base model without the scaling factor was simulated, resulting in the animation seen in Figure 32.

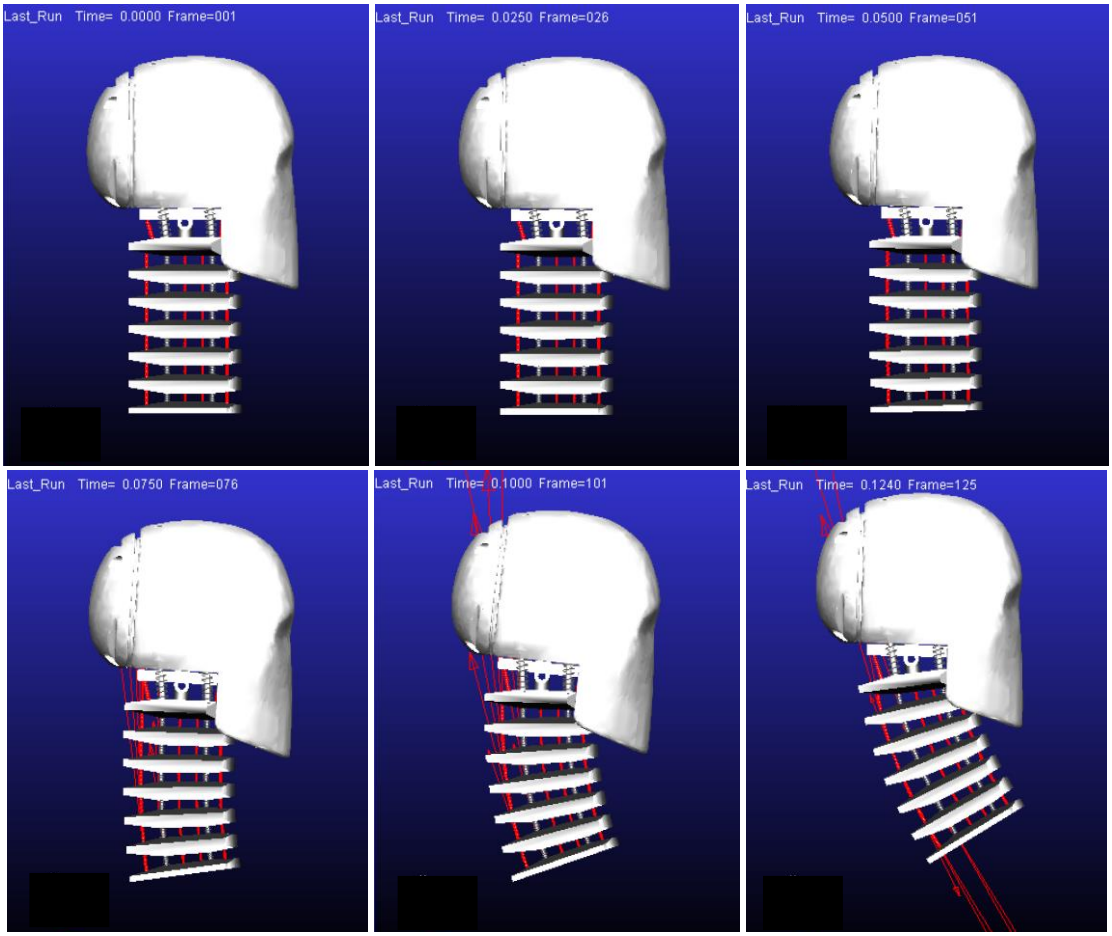

Figure 33: Base model still animation (0 to 124 ms)

The neck undergoes a great deal of flexion when using the base spring stiffnesses discussed in Chapter 2. The position of the head changes in the z direction, but it does not change a significant amount in the x direction. Acceleration responses can be seen in Figures 34 and 35.

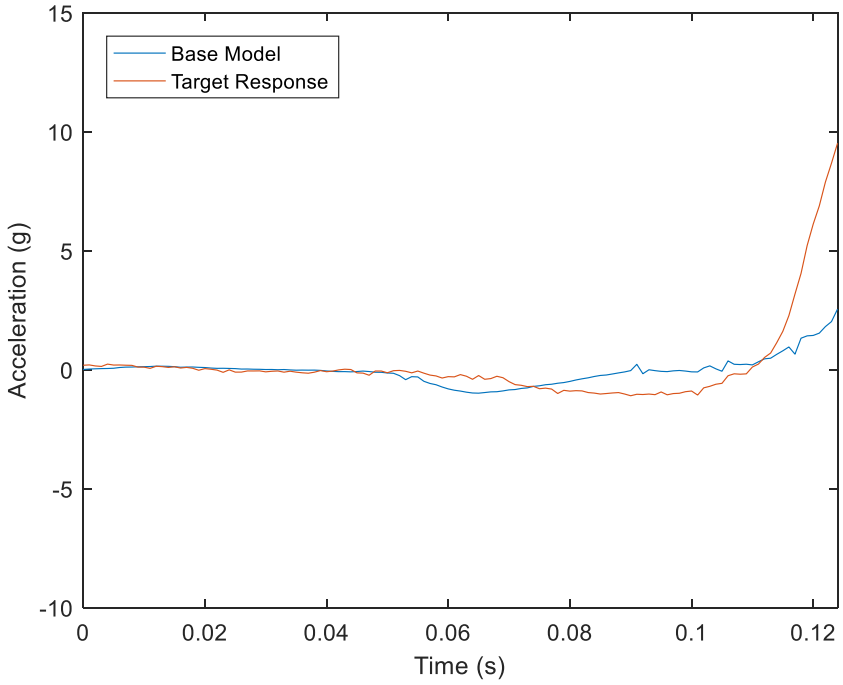

Figure 34: Base model X acceleration against average PMHS response

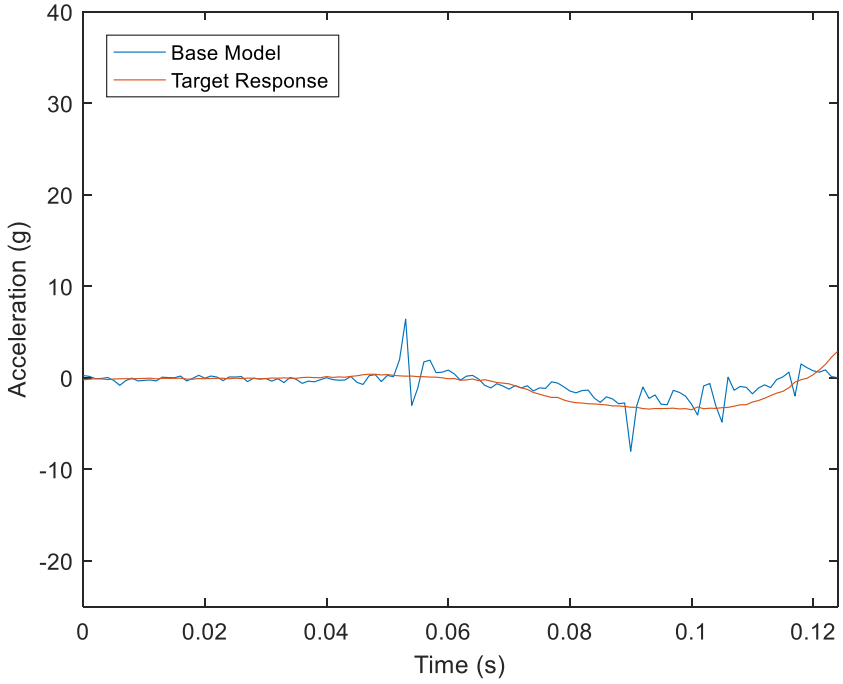

Figure 35: Base model Z acceleration against average PMHS response

The angular velocity about the y axis was also measured for this model and can be seen in Figure 36.

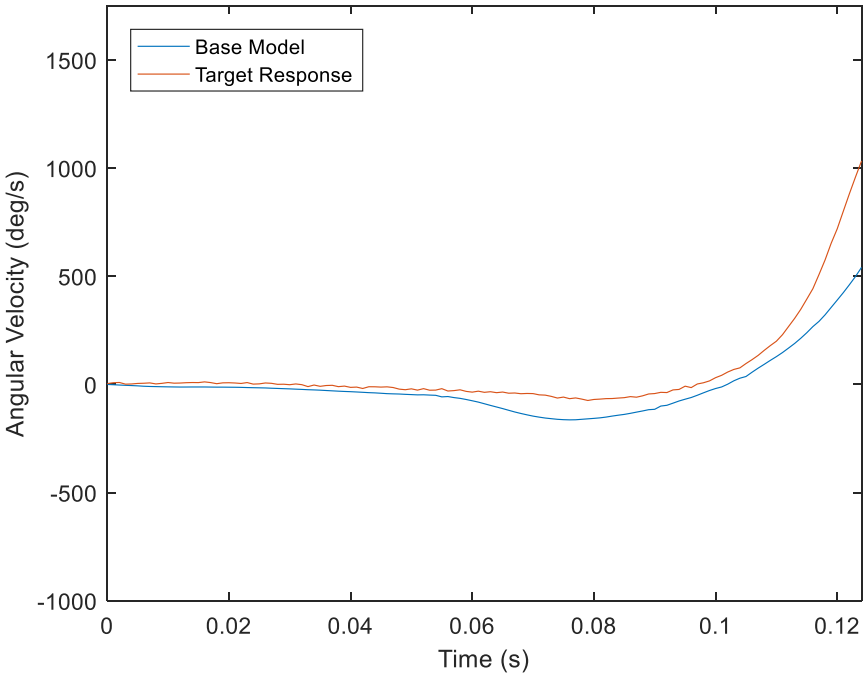

Figure 36: Base model angular velocity about Y against average PMHS response

The unscaled base model follows the trends of the experimental data fairly well. In the x direction, the acceleration appears to follow the curve well in the first 60 ms while deviating slightly after that point. Both the z acceleration and angular velocity about the y also show these characteristics.

The scaling factor of 15, based on the mass of the aluminum vertebrae in relation to a human vertebra, was then added to the spring stiffnesses in the model to attempt to achieve a better guess of a spring stiffness to follow the experimental response accurately. The resultant simulation is shown in Figure 37.

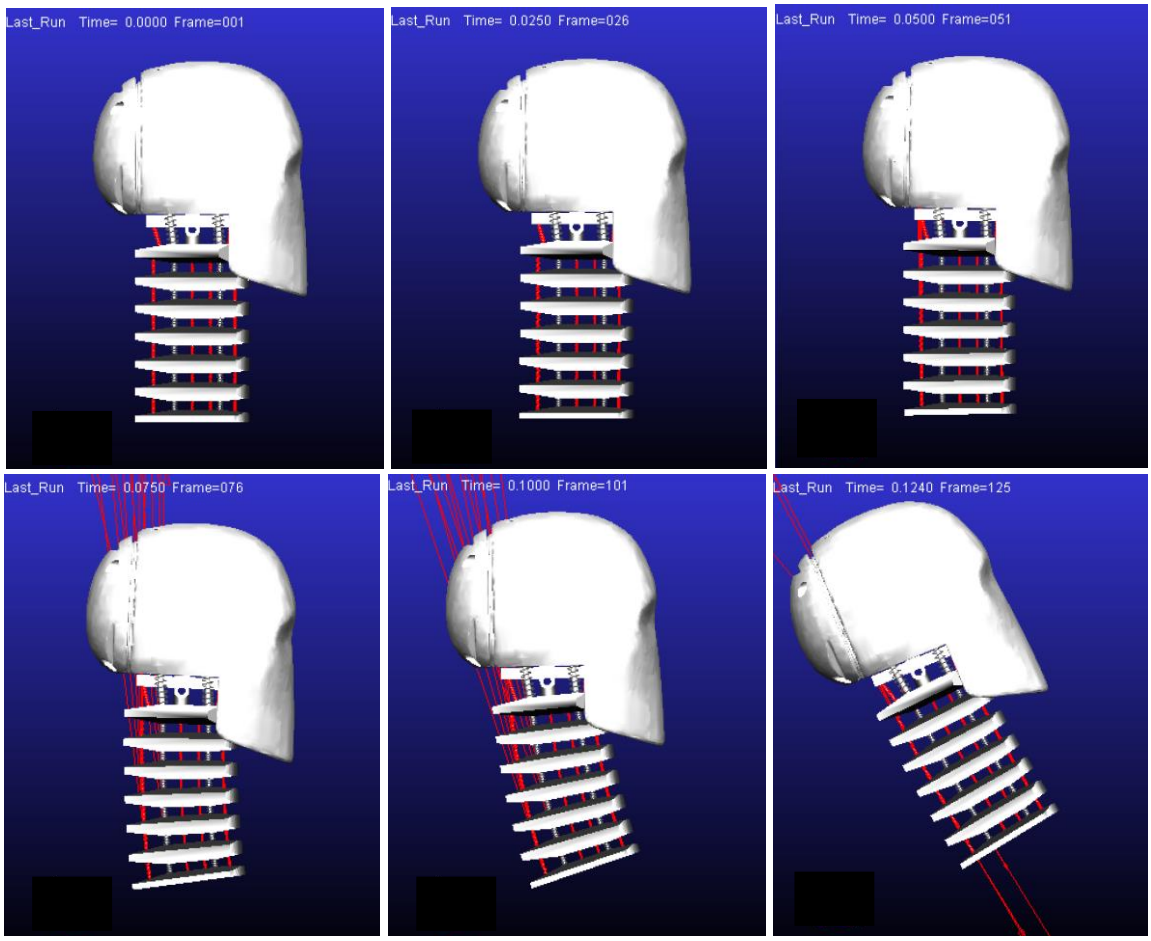

Figure 37: Scaled base model still animation (0 to 124 ms)

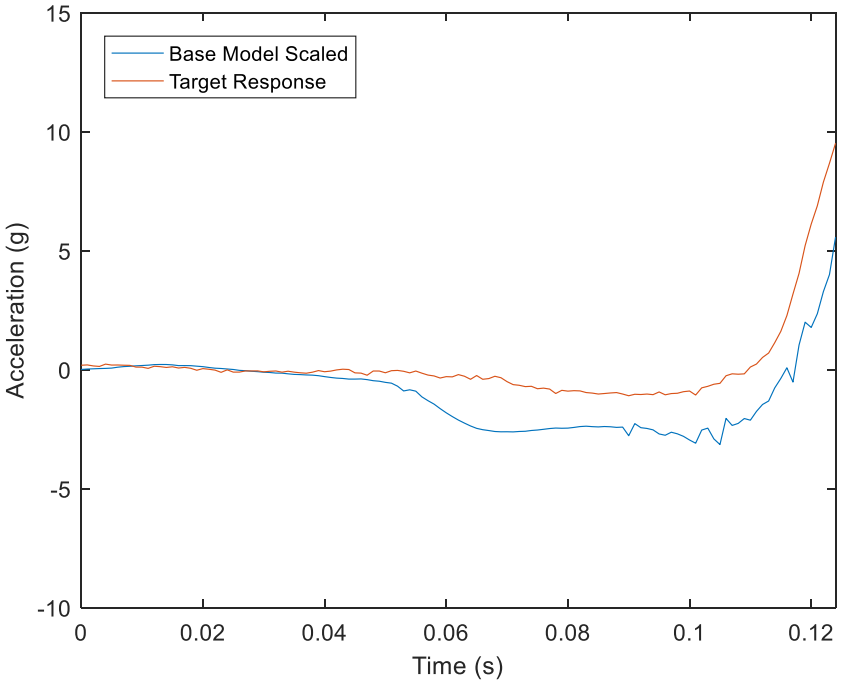

Figure 38: Scaled base model X acceleration against average PMHS response

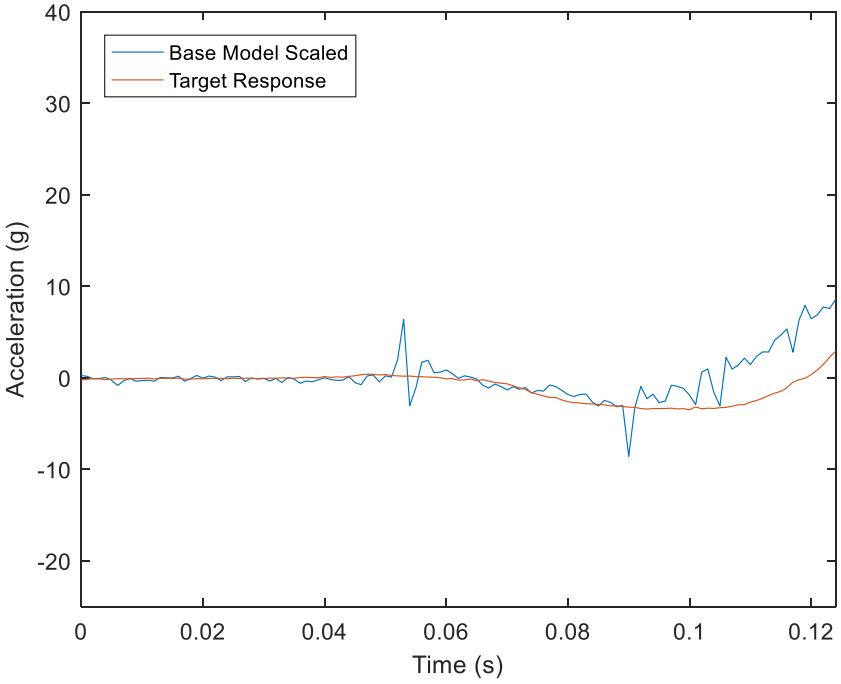

Figure 39: Scaled base model Z acceleration against average PMHS response

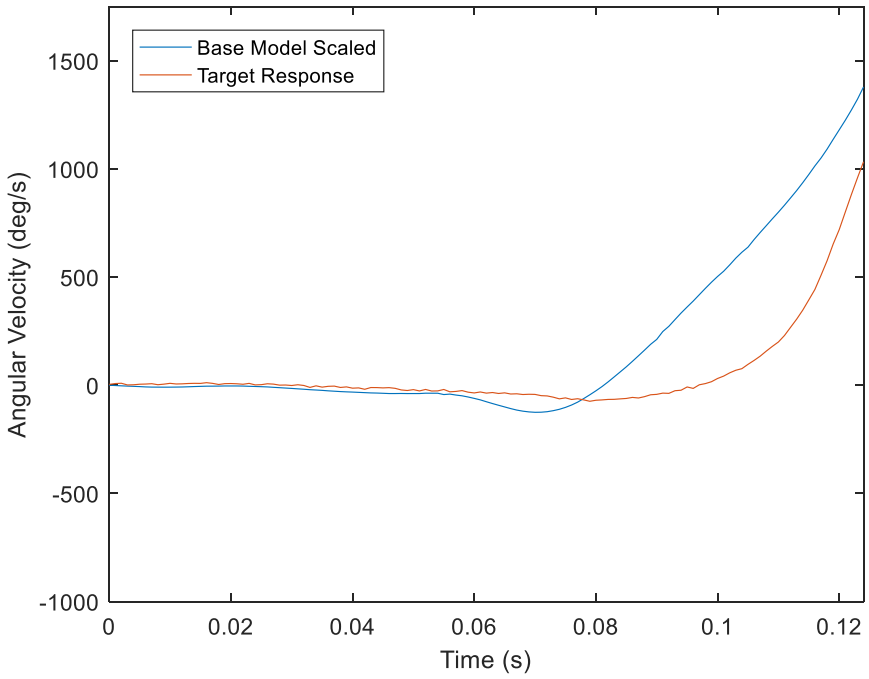

Figure 40: Scaled base model angular velocity about Y against average PMHS response

It is immediately noticeable that the x acceleration for the scaled base model follows the trend of the experimental response much closer than the unscaled base model. The z acceleration provides about the same response as the unscaled base model, and the y angular velocity follows the experimental trend well, but not better than the scaled model. Since the stiffnesses in the scaled model are closer in value to prospective stiffnesses of the polymer components, the scaled model will be used in the optimization of the virtual model.

3.4.C Optimized Model

The built-in simulation optimization function in MSC ADAMS was pivotal in determining the best stiffness configuration in order to improve the biofidelity of the model. Utilizing the base model, a series of optimization functions were created to change the spring stiffness values, while holding the damping coefficients constant, to values that provide a more

biofidelic response in comparison to the experimental data. The following functions, which are displayed with respect to the x direction (2-4), were created.

(2) $$\left|MAX\left(a_{x,scaled}\right) - MAX\left(a_{x,exp}\right)\right|$$

(3) $$\left|MIN\left(a_{x,scaled}\right) - MIN\left(a_{x,exp}\right)\right|$$

(4) $$\left|MEAN(a_{x,scaled}) - MEAN(a_{x,exp})\right|$$

Functions were then created that utilized the response in the x and z direction in combination with the angular velocity about the y axis.

(5) $$\left|\frac{MAX(a_{x,scaled}) - MAX(a_{x,exp})}{MAX(a_{x,exp})}\right| + \left|\frac{MAX(a_{z,scaled}) - MAX(a_{z,exp})}{MAX(a_{z,exp})}\right| + \left|\frac{MAX(\omega_{y,scaled}) - MAX(\omega_{y,exp})}{MAX(\omega_{y,exp})}\right|$$

(6) $$\left|\frac{MIN(a_{x,scaled}) - MIN(a_{x,exp})}{MIN(a_{x,exp})}\right| + \left|\frac{MIN(a_{z,scaled}) - MIN(a_{z,exp})}{MIN(a_{z,exp})}\right| + \left|\frac{MIN\left(\omega_{y,scaled}\right) - MIN\left(\omega_{y,exp}\right)}{MIN\left(\omega_{y,exp}\right)}\right|$$

(7) $$\left|\frac{MEAN(a_{x,scaled}) - MEAN(a_{x,exp})}{MEAN(a_{x,exp})}\right| + \left|\frac{MEAN(a_{z,scaled}) - MEAN(a_{z,exp})}{MEAN(a_{z,exp})}\right| + \left|\frac{MEAN(\omega_{y,scaled}) - MEAN(\omega_{y,exp})}{MEAN(\omega_{y,exp})}\right|$$

The functions make use of either the maximum, minimum, or mean value of the array of values corresponding to the model's response or the experimental response. The functions were created in this way because optimization in ADAMS only allows the use of one numerical value at a time. Because of this, the objective of the overall optimization was to minimize the average value of these equations.

In equations 2-4, the objective was to minimize the difference in the maximum, minimum, or mean value for each curve with respect to one another. This was done for the x acceleration, z acceleration, and angular velocity about the y axis. To combine the three respective responses into one objective function, the difference in the maximum, minimum, or mean values were normalized and summated. These functions correspond to equations 5-7.

The optimizations had varying results based on the objective function, which can be seen in Tables 8-11.

Table 8: Optimizations utilizing acceleration in the x direction

Optimization	Objective Function	Base Model Value (g)	Optimized Model Value (g)	Percent Improvement (%)
MAX-X	$\lvert MAX(a_{x,scaled}) - MAX(a_{x,exp})\rvert$	3.945	0.0191	99.5
MIN-X	$\lvert MIN(a_{x,scaled}) - MIN(a_{x,exp})\rvert$	2.051	0.001579	99.9
MEAN-X	$\lvert MEAN(a_{x,scaled}) - MEAN(a_{x,exp})\rvert$	1.17672	0.0775695	93.4

Table 9: Optimizations utilizing acceleration in the z direction

Optimization	Objective Function	Base Model Value (g)	Optimized Model Value (g)	Percent Improvement (%)
MAX-Z	$\lvert MAX(a_{z,scaled}) - MAX(a_{z,exp})\rvert$	5.08949	3.982	21.8
MIN-Z	$\lvert MIN(a_{z,scaled}) - MIN(a_{z,exp})\rvert$	5.640	3.52031	37.6
MEAN-Z	$\lvert MEAN(a_{z,scaled}) - MEAN(a_{z,exp})\rvert$	1.06925	0.2926	72.6

Table 10: Optimizations utilizing angular velocity about the y direction

Optimization	Objective Function	Base Model Value (deg/s)	Optimized Model Value (deg/s)	Percent Improvement (%)
MAX-Y	$\lvert MAX(\omega_{y,scaled}) - MAX(\omega_{y,exp})\rvert$	346	4	99
MIN-Y	$\lvert MIN(\omega_{y,scaled}) - MIN(\omega_{y,exp})\rvert$	51	5	90.9
MEAN-Y	$\lvert MEAN(\omega_{y,scaled}) - MEAN(\omega_{y,exp})\rvert$	129	0.87	99.3

Table 11: Optimizations utilizing normalization of maximum, minimum, and mean values

Optimization	Objective Function	Base Model Value	Optimized Model Value	Percent Improvement (%)
NORM-MAX	$\left\|\frac{MAX(a_{x,scaled}) - MAX(a_{x,exp})}{MAX(a_{x,exp})}\right\| + \left\|\frac{MAX(a_{z,scaled}) - MAX(a_{z,exp})}{MAX(a_{z,exp})}\right\| + \left\|\frac{MAX(\omega_{y,scaled}) - MAX(\omega_{y,exp})}{MAX(\omega_{y,exp})}\right\|$	2.207	1.862	15.6
NORM-MIN	$\left\|\frac{MIN(a_{x,scaled}) - MIN(a_{x,exp})}{MIN(a_{x,exp})}\right\| + \left\|\frac{MIN(a_{z,scaled}) - MIN(a_{z,exp})}{MIN(a_{z,exp})}\right\| + \left\|\frac{MIN(\omega_{y,scaled}) - MIN(\omega_{y,exp})}{MIN(\omega_{y,exp})}\right\|$	4.513	2.309	48.8
NORM-MEAN	$\left\|\frac{MEAN(a_{x,scaled}) - MEAN(a_{x,exp})}{MEAN(a_{x,exp})}\right\| + \left\|\frac{MEAN(a_{z,scaled}) - MEAN(a_{z,exp})}{MEAN(a_{z,exp})}\right\| + \left\|\frac{MEAN(\omega_{y,scaled}) - MEAN(\omega_{y,exp})}{MEAN(\omega_{y,exp})}\right\|$	10.280	1.655	83.9

The tables show the improvement of the initial base model value of the objective function throughout the optimization and quantify its percent improvement. Of the twelve optimizations, some were able to minimize this objective function more effectively than others.

Chapter 4: Fabrication and Assembly

4.1 Materials

Aluminum is the primary material of which the neck is composed. The grade of aluminum used was 6061 machinable aluminum. The material was chosen primarily because everything needed to be machined by hand. To minimize the risk of breaking tools during complex operations, the decision was made to use the material. Despite being easy to machine, the material is durable enough to withstand physical experiments in a low-speed impact.

4.2 Machining

The neck design featured many types of parts. Circular components were turned using a lathe and cut with high speed cutting tools. All other finishing operations were done on a milling

machine using either a drill or an end mill [30]. Engineering drawings and individual pictures of the created parts can be found in the appendix.

4.3 Assembly

In addition to machining the materials for the neck design, assembly was required. Most parts were joined using fasteners. The spherical joints consisted of a steel ball welded to the end of a small piece of all thread. All welding was done using a TIG welder [31]. A welded joint is shown in Figure 41.

Figure 41: Welded joint in final physical model assembly

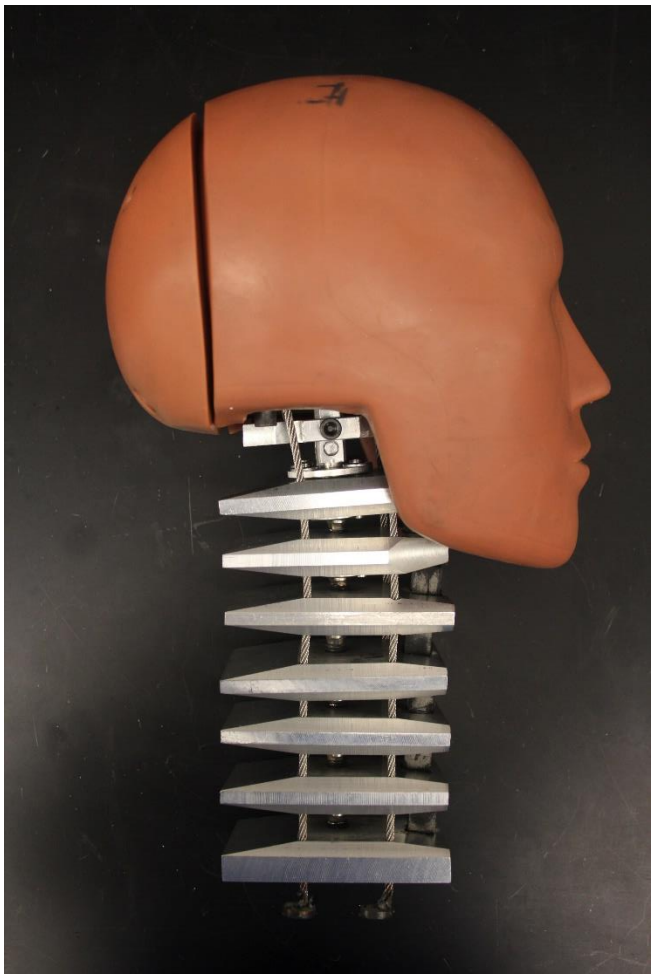

Figure 42: Final physical model assembly

Durometer 80A Polyurethane was used as the dampening component between vertebral bodies [22]. The elastic modulus of this material has been experimentally determined to be 2 to 3 MPa [21]. In order estimate a more specific value for the elastic modulus, equation 8 was used.

(8) $$E = e^{0.0235 \times D - 0.6403} = e^{0.0235 \times 80 - 0.6403} = 3.45\ MPa$$

$$where\ D = Shore - A\ Durometer = 80$$

Unfortunately, this is only a rough estimate of the elastic modulus and not a certain value. In order to determine the modulus confidently, dynamic compression tests need to be performed on a known cross section of the selected material.

4.4 Cost

The cost of the neck was kept to a minimum throughout the entire project. The cost of all the parts can be seen in the table below, which excludes the cost of the tools needed to machine the prototype as seen in Table 12.

Table 12: Project parts list and cost

Part	Part Number	Function	Length (in)	Quantity	Cost
304 Stainless Steel Ball 1/2" Diameter	9291K54	Spherical Joint	-	15	$11.61
18-8 Stainless Steel Wire Flexible Rope, Lubricated 1/8" Diameter	3461T466	Wire Rope	120	1	$6.30
Low-Strength Steel Threaded Rod 1/4"-20	98790A320	Wire Rope Adjustment	12	1	$0.62
6061 Aluminum 3-1/2" Diameter	1610T129	Skull Base	0.50	1	$6.96
6061 Aluminum 1/2" Thick x 1-1/4" Wide	8975K801	Upper Occipital	6	1	$3.56
Tight-Tolerance 6061 Aluminum Rod 1/4" Diameter	9062K344	Occipital	6	1	$4.62
6061 Aluminum 3/8" Diameter	8974K249	Lower Occipital	6	1	$1.99
6061 Aluminum 3/8" Thick x 1-3/4" Wide	8975K888	Occipital Damper	6	1	$3.60
6061 Aluminum 3/4" Diameter	8974K299	Occipital Mate	6	1	$3.17
6061 Aluminum 1" Diameter	8974K269	Spherical Constraint	6	2	$5.32
Class 10.9 High-Strength Steel Threaded Rod M10 x 1.5 mm	1078N13	Spherical Joint	1 (m)	1	$10.00
6061 Aluminum 5/8" Thick x 2-1/2" Wide	8975K622	Vertebral Bodies	36	1	$30.71
6061 Aluminum 1-1/2" Diameter	1610T13	Occipital Constraint	0.5	1	$2.57
DIN 17223 & 2095 Precision Compression Spring Music-Wire Steel, CF End	94125K612	Wire Rope Adjustment	15 (mm)	5	$10.36
Abrasion-Resistant Polyurethane Rubber Sheet 6"x6" 1/2" Thick 80A	8716K58	Polymer Dampers	-	1	$31.21
				TOTAL	$132.60

The total cost of the neck was $132.60. About a quarter of the cost can be attributed to the rubber damping components, and another half of the cost to the aluminum needed for machining.

Chapter 5: Results

A more detailed quantification of the optimization results is shown below by calculating the biorank from the representative PMHS curve for each optimization, shown in Table 13.

Table 13: Biorank of all optimizations and base models

Optimization	Biorank a_x	Biorank a_z	Biorank ω_y	Average Biorank
BASE	0.863	0.819	0.758	0.813
BASE-SCALED	1.635	1.425	1.767	1.609
MAX-X	1.719	1.782	2.349	1.950
MIN-X	0.838	0.815	0.613	0.755
MEAN-X	0.958	0.800	0.600	0.786
MAX-Z	1.540	1.348	1.438	1.442
MIN-Z	1.297	1.077	1.171	1.182
MEAN-Z	0.897	0.791	0.504	0.731
MAX-Y	1.029	0.892	0.841	0.921
MIN-Y	1.964	2.003	2.741	2.236
MEAN-Y	0.896	0.813	0.587	0.765
NORM-MAX	1.705	1.770	2.341	1.939
NORM-MIN	0.898	0.782	0.510	0.730
NORM-MEAN	0.958	0.800	0.600	0.786

The NHTSA biorank calculates the deviation of the model's response relative to one standard deviation from the average response of the PMHS corridor. Equation 9 was used to calculate biorank.

(9) $$BR = \frac{\sum_{i=1}^{n} |x_{i,model} - x_{i,avgPMHS}|}{\sum_{i=1}^{n} x_{i,stdPMHS}}$$

The biofidelity of the response of the ADAMS simulation can be visualized by plotting the response with respect to the corridors describing the PMHS response in the previous study [28]. Plots including the base model, scaled base model, and the three optimizations with the lowest biorank score can be seen in the Figure 43.

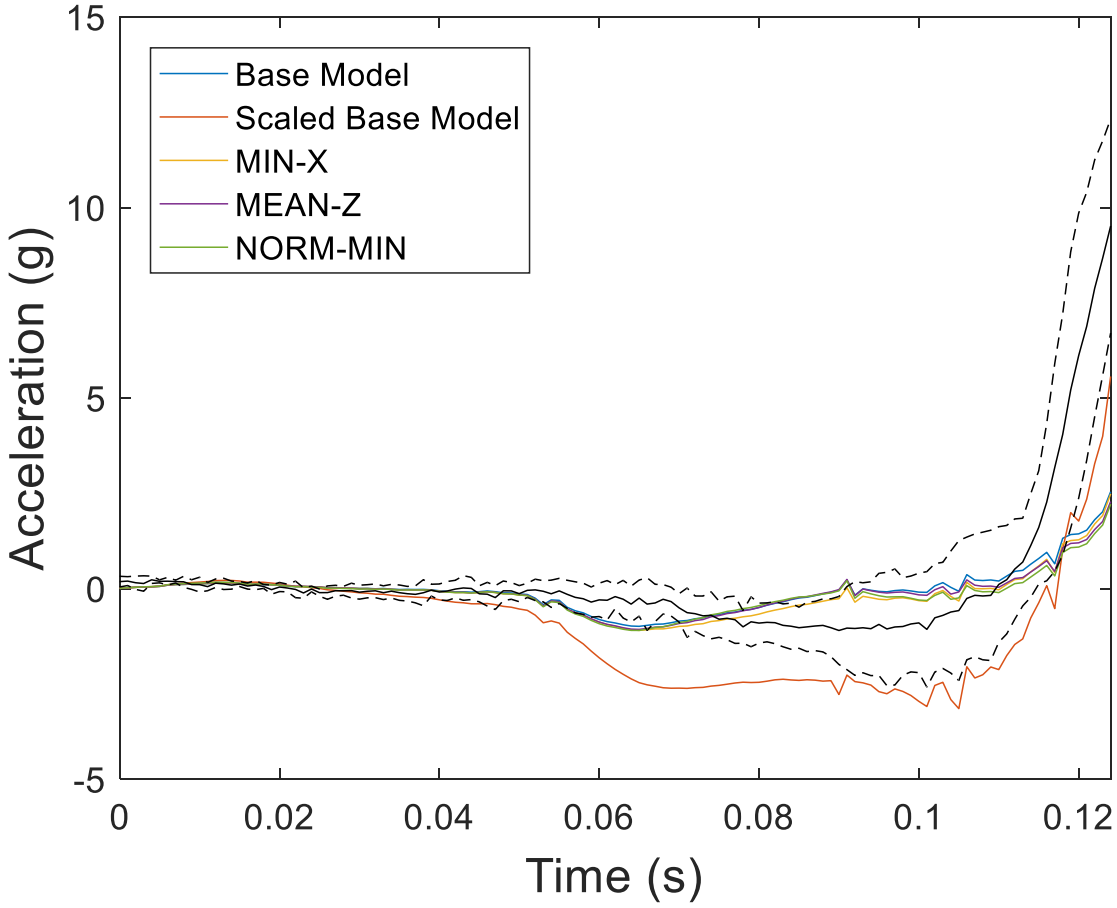

Figure 43: Simulations' X acceleration against PMHS corridor [28]

The acceleration in the x direction of the model neck of the most biofidelic optimizations correlate well with the unscaled base model. There is a trend of the x acceleration of the center of gravity of the head being negatively oriented initially (neck extension) before moving in the positive direction (neck flexion).

The z axis acceleration of the best optimizations against the PMHS corridor can be seen in Figure 44.

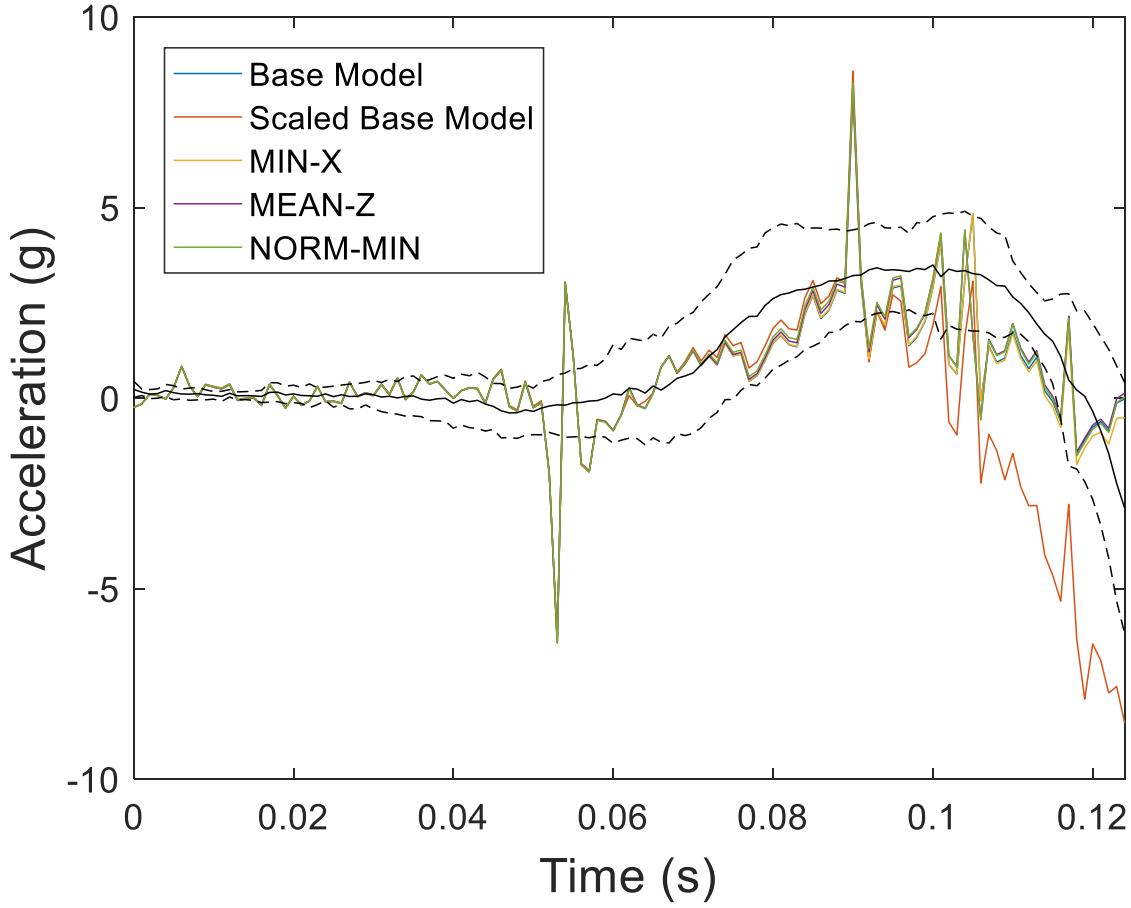

Figure 44: Simulations' Z acceleration against PMHS corridor [28]

The z axis acceleration follows the general trend of the PMHS mean curve. Interestingly, the scaled base model deviated slightly from the corridor towards the end of the event.

The angular velocity about the y axis during the optimization can be seen in the Figure 45.

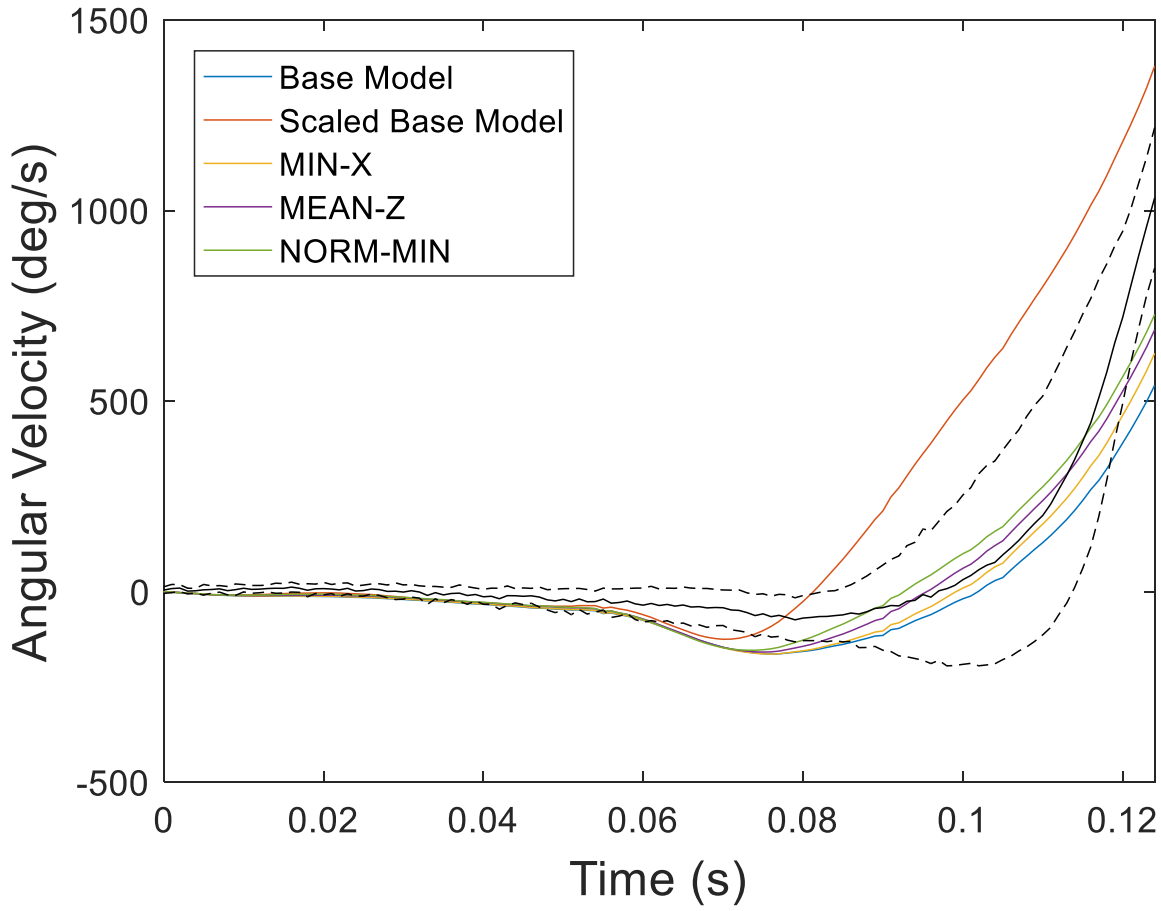

Figure 45: Simulations' angular velocity about Y against PMHS corridor [28]

The results of the angular velocity are like the other two criteria because the scaled base model deviated significantly from the optimizations and unscaled base model, which see a similar response. Figure 46 is a visualization of one of the optimization simulations (NORM-MIN) in comparison to the PMHS response.

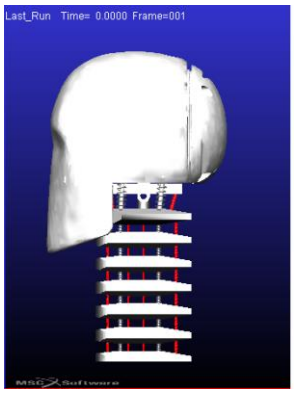
Last_Run Time= 0.0000 Frame=001


S101209-1
TRC

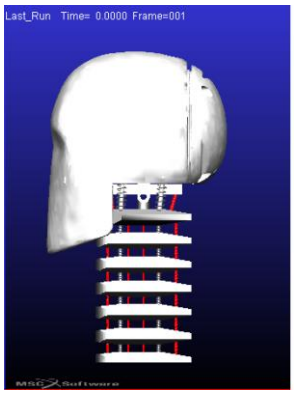
Last_Run Time= 0.0000 Frame=001


S101209-1
TRC

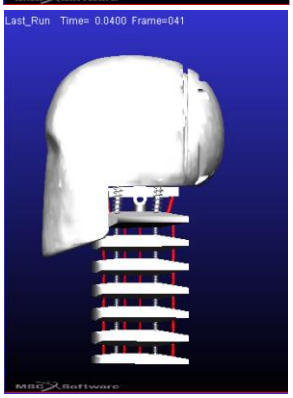
Last_Run Time= 0.0400 Frame=041


S101209-1
TRC

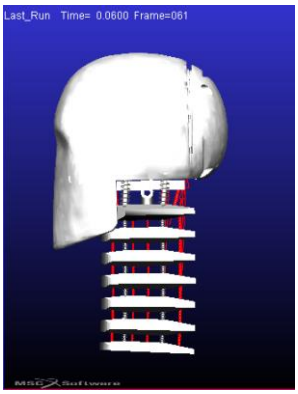
Last_Run Time= 0.0600 Frame=061


S101209-1
TRC

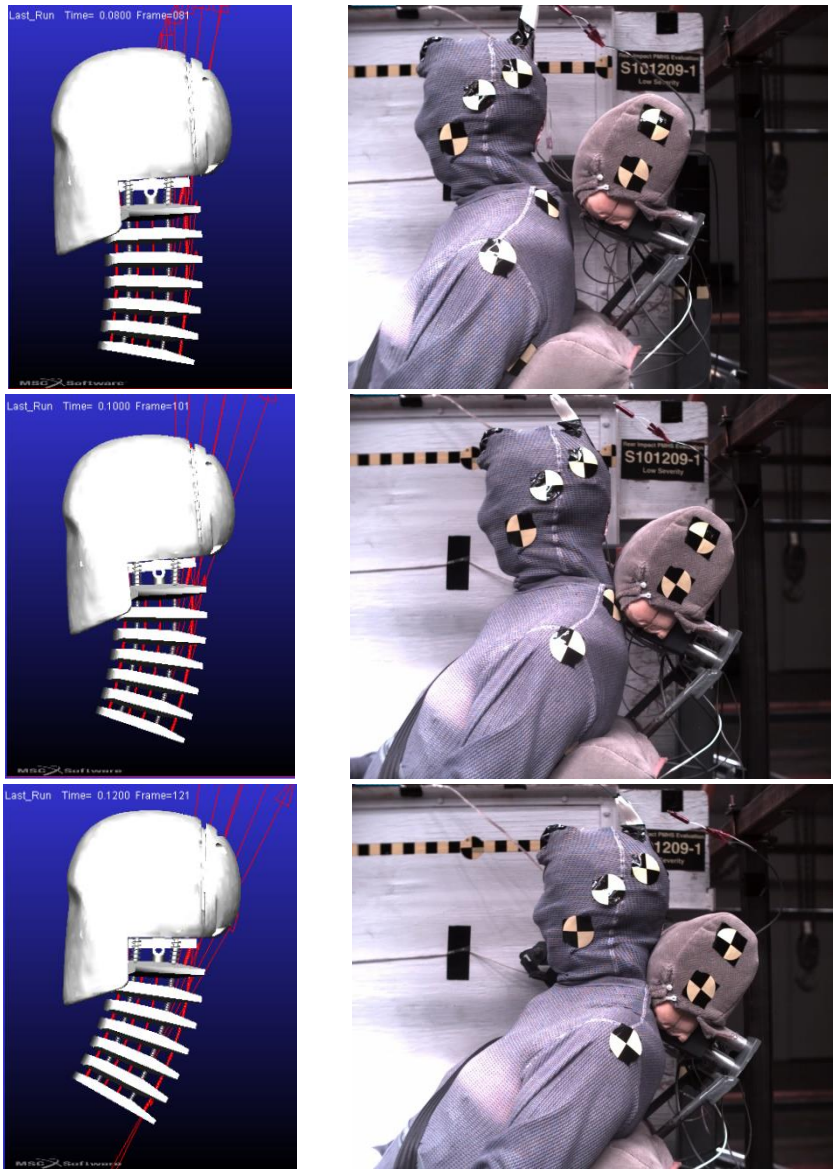

Figure 46: NORM-MIN optimization simulation animation in contrast to PMHS experiment [28]

Because the three optimizations discussed (MIN-X, MEAN-Z, and NORM-MIN) have the lowest biorank, they correspond to the stiffness configurations that will result in the most biofidelic response for the physical model. The resulting stiffnesses from these optimization scan be seen in the Table 14.

Table 14: Resulting stiffnesses from best optimizations

Optimization	Spring	Initial Stiffness (N/mm)	Final Stiffness (N/mm)
MIN-X	P1	497.1	1.651
	P2	491.1	328.7
	P3	259.5	26.02
MEAN-Z	P1	497.1	0
	P2	491.1	269.3
	P3	259.5	187.1
NORM-MEAN	P1	497.1	9.507
	P2	491.1	264.1
	P3	259.5	511.4

The stiffness of spring P1, the most posterior spring, resulted in having a very small value with respect to the two other springs, P2 and P3.

Chapter 6: Discussion

6.1 Initial Design Decisions

Prior to designing the neck, several assumptions were made. The first corresponds to the neck material, which is 6061 aluminum. This was chosen because it is lightweight, machinable, and durable. Although aluminum is a lightweight metal, it is not light in comparison to bone, seeing that the mass of the vertebral body design was a factor of 15 larger than a human vertebra. This problem was accounted for initially by multiplying the stiffnesses of the base model by a factor of 15. However, Figures 42-44 in the previous chapter show that the unfactored base model had a response that was much closer to the most biofidelic optimizations. This shows that the factored spring stiffnesses were not necessary, and that the experimentally determined stiffness of human ligaments in the neck can be used in this neck design if available. However, for this study, the stiffness values of one of the optimizations is used when inserting the polymer damping components to the physical model.

6.2 Design Biofidelity

The response of the three best optimizations had an average biorank of less than 1 across the three measures of interest. This means that, when compared to the data corridor, on average, the responses of these three optimizations fall within a standard deviation of the mean PMHS response. When considering biorank, a biorank of less than 2 is generally recognized as biofidelic. This means that this neck design is considerably biofidelic in comparison to rear impact PMHS experiments. Because the model is so biofidelic, it is justified that the design can be fabricated and physically experimented.

6.3 Limitations

One limitation exists in the spherical joints between the vertebrae, which permit three degrees of rotation. When considering intervertebral disks in the human neck, they permit three degrees of rotation and three directions of translation, meaning that the mating between vertebrae in this neck design is not humanlike. These spherical joints were also created using a welder, which has a disadvantage in creating perfect alignment of the ball with respect to the threaded rod. Because of this, the spherical joints of the physical model may have had a slightly different position than the spherical joints in the virtual model.

Another limitation of this study lies in the optimization functions used for optimizing the spring stiffness of the virtual model. These functions could only optimize a single point across an entire response curve. If a function were created to minimize the difference between the entire curves for the model response and the PMHS response rather than the difference between single points on each curve, then the stiffness configuration for the most biofidelic design could have been revealed. However, because this was not possible, the resulting configurations that correspond to a biorank of less than 1 are used instead.

Because of the timeline of this project, the physical prototype provision suffers. The prototype was created entirely by hand in a student machine shop, meaning that there is dimensional variation across parts on a small scale. If the design's parts were to be programmed to a CNC machine, this variation among dimensions could be minimized, making for a more effective physical model to be used in the physical experimentation portion of this project. Additionally, more precise, secure attachments, such as clamps or threading, can be used instead of welding in the spherical joints and the wire rope.

Chapter 7: Conclusion

7.1 Contributions

This project has successfully validated the biofidelity of a virtual ATD model neck design that allows for more kinematic degrees of freedom, making it a more realistic design than other necks seen in use in industry. This validation also justifies the experimentation of the physical model to validate the prototype. The prototype is a hand-machined draft of what the final physical model will look like and serves only as a prototype with which the neck design can by physically validated. Despite this fact, the future provision of this validated physical prototype design, rather than the prototype itself, is extremely important moving forward because it will provide the automotive industry with a better tool with which they can design passenger safety systems in cars, such as occupant head restraint systems. The improvement of this safety feature will ultimately make automobiles safer for occupants and contribute to a reduction in people injured in car crashes, and specifically it will reduce the amount of people that are hurt in rear impact collisions.

7.2 Additional Applications

The neck in this project was created with the intention to be more versatile than previous biofidelic necks. This versatility is found in the provision of neck movement in multiple directions. Because of this capability, this neck design is not limited to usage in rear impacts. In a similar method used in this study, the neck design can be validated in other impact scenarios, such as a side impact, oblique impact, or a frontal impact crash. If every common crash scenario is accounted for in the final design of this prototype, then it will be the closest surrogate to a human neck available to the automotive industry. This has astounding implications in improving safety systems in vehicles in the future, which may see unique seating configurations for vehicle occupants. Because this neck can provide any direction of movement, if the biofidelity in that direction is validated, it can be used for injury assessment in the respective vehicle collision.

7.3 Future Work

The immediate next step in the ongoing project is to validate the physical model. This will be done using an experimental setup to simulate a low speed rear end collision that has been used in previous studies [8] [29]. The experimental fixture consists of a mount that slides on linear rails along a flat surface. On the mount is the ATD head and neck, with the T1 vertebra being connected to a load cell attached to the mount and the head hanging freely. The sliding mount is forced to a speed seen in low speed rear impacts by a pneumatic ram system. The free hanging head and neck then impacts the end of the fixture. This part of the fixture is intended to represent the rigid seatback that the posterior part of the head strikes during the event. The fixture can be seen in the Figure 47.

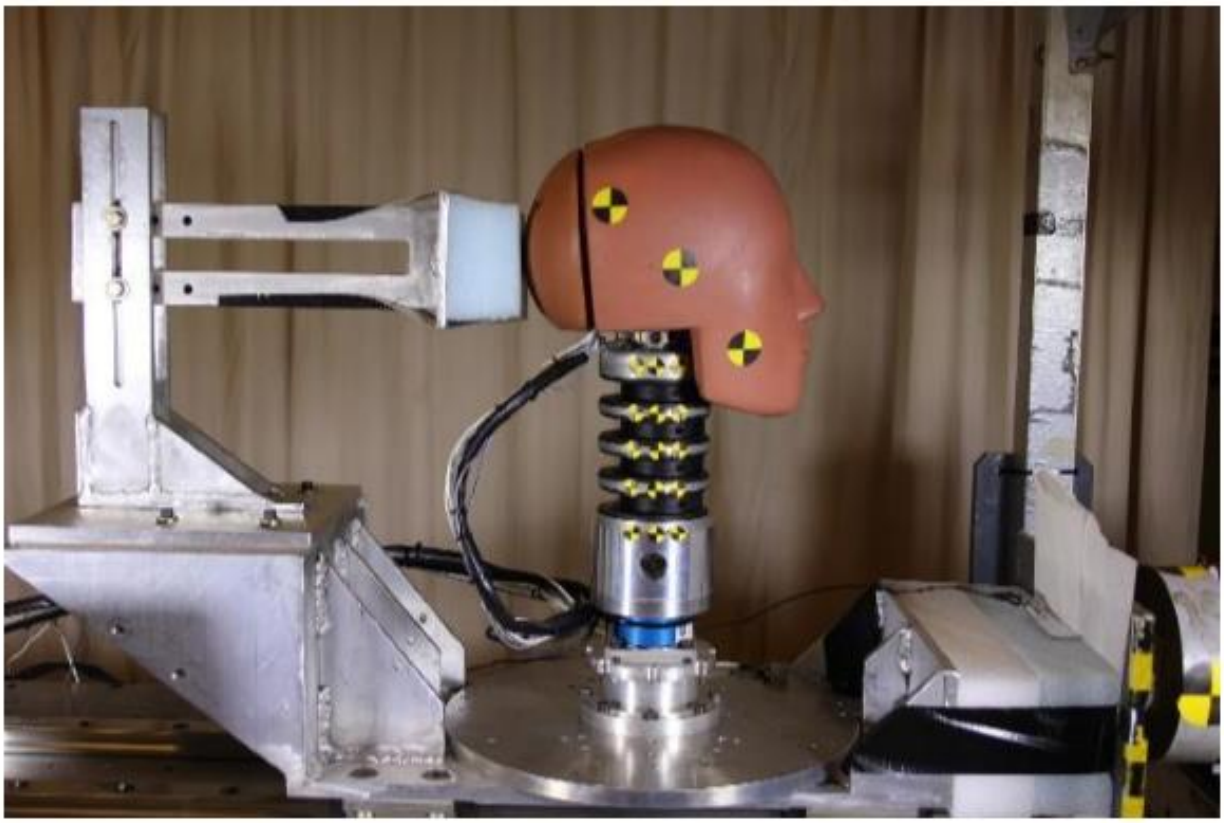

Figure 47: Experimental fixture with Hybrid III head and neck mounted

The instrumentation used during experimentation needs to return the same measures as the simulation. A six degree-of-freedom (DTS 6DX Pro) will be used for data acquisition with a high-speed data acquisition system (SlicePro, 20 kHz) [32]. This sensor is capable of returning the acceleration in the x and z direction, as well as rotation about the y direction (SAE J211).

The physical model will first be experimented on in a rear impact scenario to validate the design used in this study. However, when moving forward with design validation, other directions of impact can be included in order to create the most biofidelic neck possible. In addition to this response, the static response of the neck can be validated using the angles of flexion, extension, and rotation seen in Table 1 in Chapter 2 of this thesis.

Also, further refinement of the ADAMS model is needed to create a better and more biofidelic physical model. This included further experimentation and optimization with different

optimization functions that better reflect the overall shape of the target x and z axis accelerations and y axis angular velocity. This will primarily change the polymer damping components between vertebrae.

Finally, there is more work to be done concerning future physical prototypes. Firstly, the ball joints can be replaced with threaded balls attached to a threaded rod to ensure proper alignment. This will ensure that the intervertebral joints do not alter the kinematics of the entire system because they are misaligned. Secondly, the stiffness and damping properties of the polyurethane material used can be experimentally determined using static and dynamic testing with a drop tower, using a falling mass as the input to the system. This will give the most accurate estimate of the polymer component stiffness, instead of relying on theoretical values.

7.4 Summary

The purpose of this study was to design a neck for an anthropomorphic test device that adds kinematic degrees of freedom, while the objective of the study was to validate the biofidelity of this design. This was done in response to current necks in industry having limitations either in biofidelity or range of motion, which consequentially can affect the neck's biofidelity. This study successfully provided the design for this type of neck, and furthermore the neck was validated on a preliminary level using ADAMS. The virtual models received a biorank score of less than one. Because the neck was fabricated, the physical model will be physically validated in a low-speed rear impact environment. If validated, the automotive industry will be provided with a physical ATD neck that has significant implications in improving passenger safety in rear impacts.

REFERENCES

[1] Davidsson, J., Flogard, A., Lovsund, P. and Svensson, M. Y., "BioRID P3 – Design and Performance compared to Hybrid III and Volunteers in Rear Impacts at ΔV=7 km/h," SAE Technical Paper 99SC16, 1999.

[2] Scott, M. W., McConnell, W. E., et al., "Comparison of Human and ATD Head Kinematics During Low-Speed Rearend Impacts," SAE Technical Paper 930094, 1993.

[3] Foster, J. K., Kortage, J. O., Wolanin, M. J., "Hyrbid III – A Biomechanically Based Crash Test Dummy," SAE Technical Paper 770938, 1977.

[4] Prasad, P., Kim, A., Weerappuli, D.P.V., "Biofidelity of Anthropomorphic Test Devices for Rear Impact," SAE Technical Paper 973342, 1997.

[5] Mertz, H. J., Patrick, L. M. "Strength and Response of the Human Neck," SAE Technical Paper 710855, 1971.

[6] Culver, C. C., Neathery, R. F., Mertz, H. J., "Mechanical Necks with Humanlike Responses," SAE Technical Paper 720959, 1972.

[7] Mertz, H. J., Patrick, L. M., "Investigation of the Kinematics and Kinetics of Whiplash," SAE Technical Paper 670919, 1967.

[8] Kang, Yun-Seok, et al. "PMHS Lower Neck Load Calculation using Inverse Dynamics with Cervical Spine Kinematics and Neck Mass Properties." *International Research Council on Biomechanics of Injury* (2016).

[9] Moorhouse, Kevin, et al. "Evaluation of the Internal and External Biofidelity of Current Rear Impact ATDs to Response Targets Developed from Moderate-Speed Rear Impacts of PMHS." *Stapp Car Crash Journal*, 6, 171-229, 2012.

[10] NHTSA, "Federal Motor Vehicle Safety Standards; Head Restraints (FMVSS 202a)" Federal Register 49 CFR Part 571, Docket no. NHTSA-2004-19807, December 14, 2004.

[11] EEVC. "Dummy Requirements and Injury Criteria for a Low-speed Rear Impact Whiplash Dummy." Working group 12 report, 2007.

[12] Kuppa, S. "Injury Criteria and Anthropomorphic Test Devices for Cervical Spine Injury Assessment." NHTSA Docket No. 19807, 2004.

[13] Humanetics Innovative Solutions. BioRID (50^{th} Male) Rear Impact.

[14] Penčić, Marko et al. "Assistive Humanoid Robot MARKO: Development of the Neck Mechanism." *MATEC Web of Conferences*, 121:08005-1-08005-8, 2017.

[15] Panjabi, Manohar M. et al. “Mechanical Properties of the Human Cervical Spine as Shown by Three-Dimensional Load-Displacement Curves.” *SPINE* Vol. 26, Num. 24, pp 2692-2700, 2001.

[16] Yoganandan, Narayan, Kumaresan, Srirangam & Pintar, Frank A. “Geometric and Mechanical Properties of Human Cervical Spine Ligaments.” *Journal of Biomechanical Engineering*, Vol. 122 pp 623-629, 2000.

[17] Dibb, Alan T. et al. “Tension and Combined Tension-Extension Structural Response and Tolerance Properties of the Human Male Ligamentous Cervical Spine.” *Journal of Biomechanical Engineering*, Vol. 131 pp 23-629, pp 081008-1-11. 2009.

[18] Netter, Frank H., MD. *Atlas of Human Anatomy – 6th Edition.* Philadelphia, Saunders Elsevier. Print. 2014.

[19] Collins, Jack A., Busby, Henry and Staab, George. *Mechanical Design of Machine Elements and Machines: A Failure Prevention Perspective – 2nd Edition.* John Wiley & Sons, Inc. Print. 2010.

[20] Lowrance, E. W., Latimer, Homer B. “Weights and Variability of Components of the Human Vertebral Column.” *The Anatomical Record,* Vol. 159 pp. 83-88. 1967.

[21] *Materials Data Book - 2003 Edition*. Cambridge University Engineering Department. PDF. 2003.

[22] *Abrasion-Resistant Polyurethane Rubber Sheet.* 8716k58. McMaster Carr. March 2018

[23] Keller, Michael J. “Development of a Cervical Spine Model for Rear Impact Conditions.” *Ohio State Honors Undergraduate Thesis.* 2010.

[24] Dauvilliers, F., Bendjellal, F. Weiss, M. LAvaste, F. er al. “Development of a Finite Element Model of the Neck.” *SAE Technical Paper.* 942210, 1994

[25] Davidsson, Johan, Svensson, Mats Y et al. “BioRID I – A New Biofidelic Rear Impact Dummy.” *IRCOBI Conference Paper.* 1998.

[26] Lundell, Björn, Jakobsson, Lotta, Alfredsson, Bo et al. “The Whips Seat – A Car Seat for Improved Protection Against Neck Injuries in Rear End Impacts.” 98-S7-O-08. 1998.

[27] “Early Estimate of Motor Vehicle Traffic Fatalities for the First Nine Months of 2017.” *NHTSA.* DOT S 812 490. 2018.

[28] Kang, Yun-Seok, Bolte IV, John H et al. “Biomechanical Responses of PMHS in Moderate-Speed Rear Impacts and Development of Response Targets for Evaluating the Internal and External Biofidelity of ATDs.” *STAPP Car Crash Journal.* Vol. 56, pp. 105-170. 2012.

[29] Stammen, Jason, Moorhouse, Kevin et al. “The Large Omnidirectional Child (LODC) ATD: Biofidelity Comparison with the Hybrid III 10 Year Old.” *STAPP Car Crash Journal.* Vol. 60 pp. 16S-11-43. 2016.

[30] Robert O. Webster Machine Shop. *Department of Mechanical and Aerospace Engineering at The Ohio State University.*

[31] Astronomy Machine Shop. *Department of Astronomy at The Ohio State University.*

[32] *DTS 6DX Pro Product Datasheet.* DTS, Seal Beach, California, USA. DTS-003 Rev 3. 2015.

[33] *SAE J211-1 Surface Vehicle Recommended Practice.* RevMAR95. 1995

[34] Yoganandan, N., Kumaresan, S., and Pintar, F.A. “Biomechanics of the cervical spine Part 2. Cervical spine soft tissue responses and biomechanical modeling.” *Clinical Biomechanics* 16(1) pp. 1-27. 2001.

[35] Kang, Yun Seok, Moorhouse, Kevin, Herriott, Rod, and Bolte IV, John H. “Comparison of Cervical Vertebrae Rotations for PMHS and BioRID II in Rear Impacts.” *Traffic Injury Prevention.* Vol 14, S13-S147. 2013.

[36] Rhule, Heather, Donnelly, Bruce, Moorhouse, Kevin, and Kang, Yun Seok. “A Methodology for Generating Objective Targets for Quantitatively Assessing the Biofidelity of Crash Test Dummies.” *Enhanced Safety of Vehicles*. 13-0138. 2013.

[37] Moorhouse, Kevin et. al. “Evaluation of the Internal and External Biofidelity of Current Rear Impact ATDs to Response Targets Developed from Moderate-Speed Rear Impacts of PMHS.” *Stapp Car Crash Journal.* Vol. 56, pp. 171-229. 2012.

APPENDIX A

The following figures shown are the Inventor drawings made for each fabricated part of the physical model, as well as pictures of the actual parts. Units and drawing standards were chosen at convenience depending on the dimensions of the part.

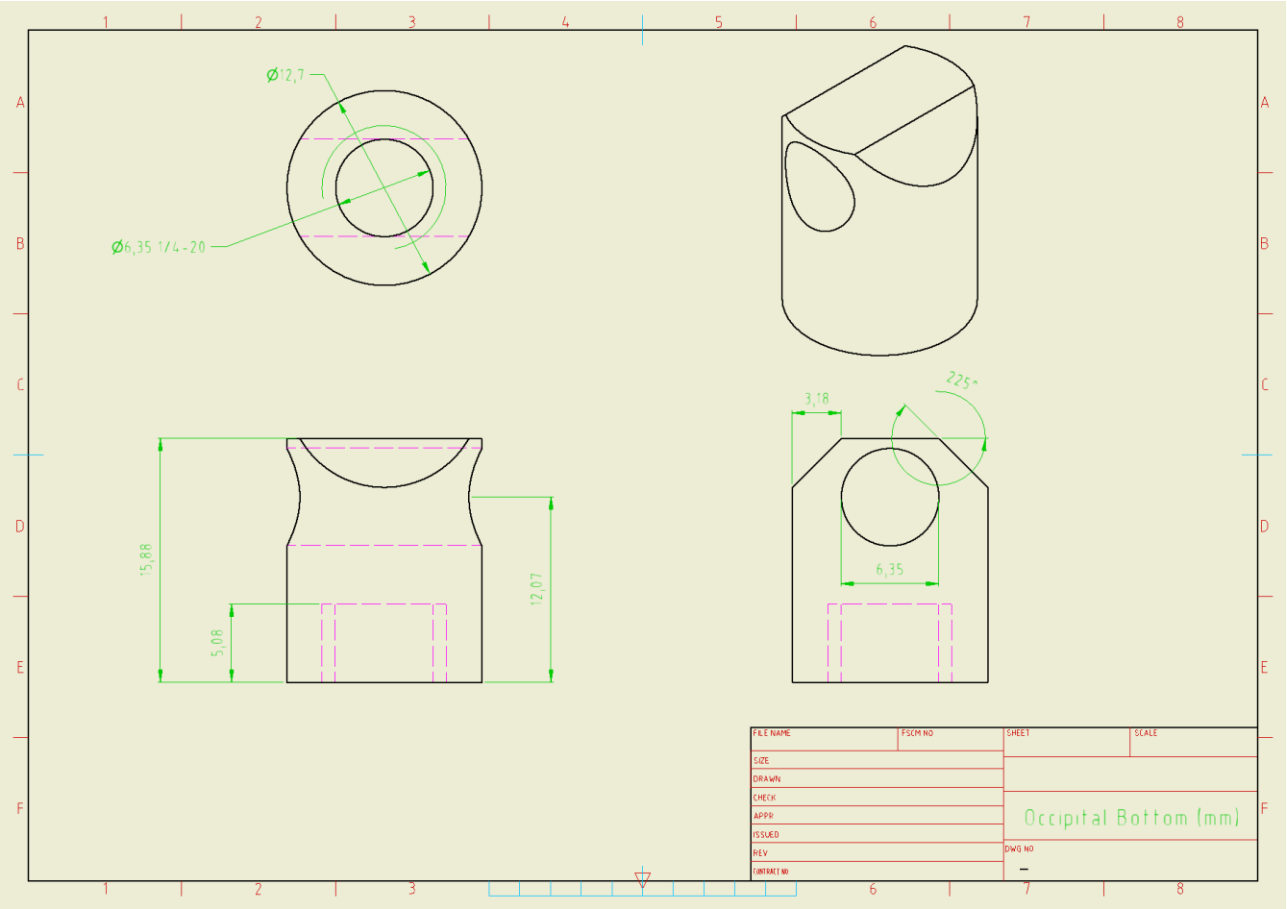

Figure 48: Lower occipital drawing (Aluminum, AM_BSI)

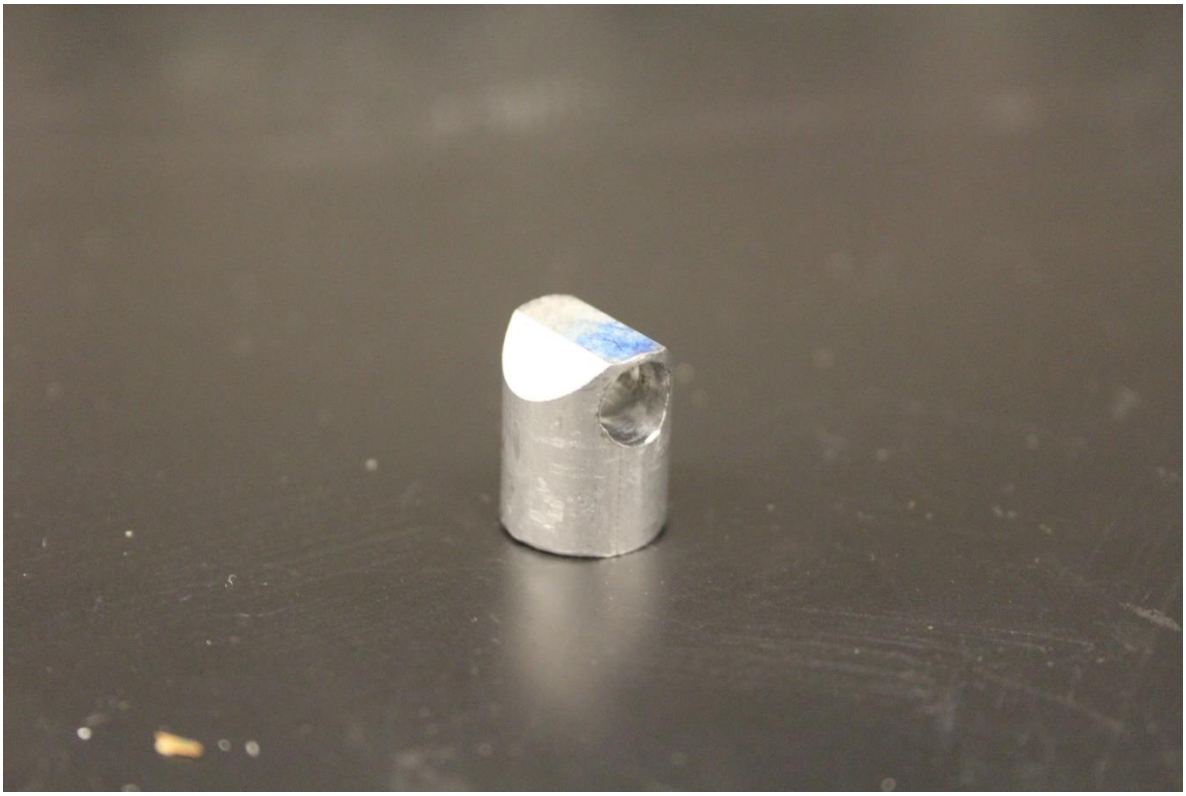

Figure 49: Lower occipital part

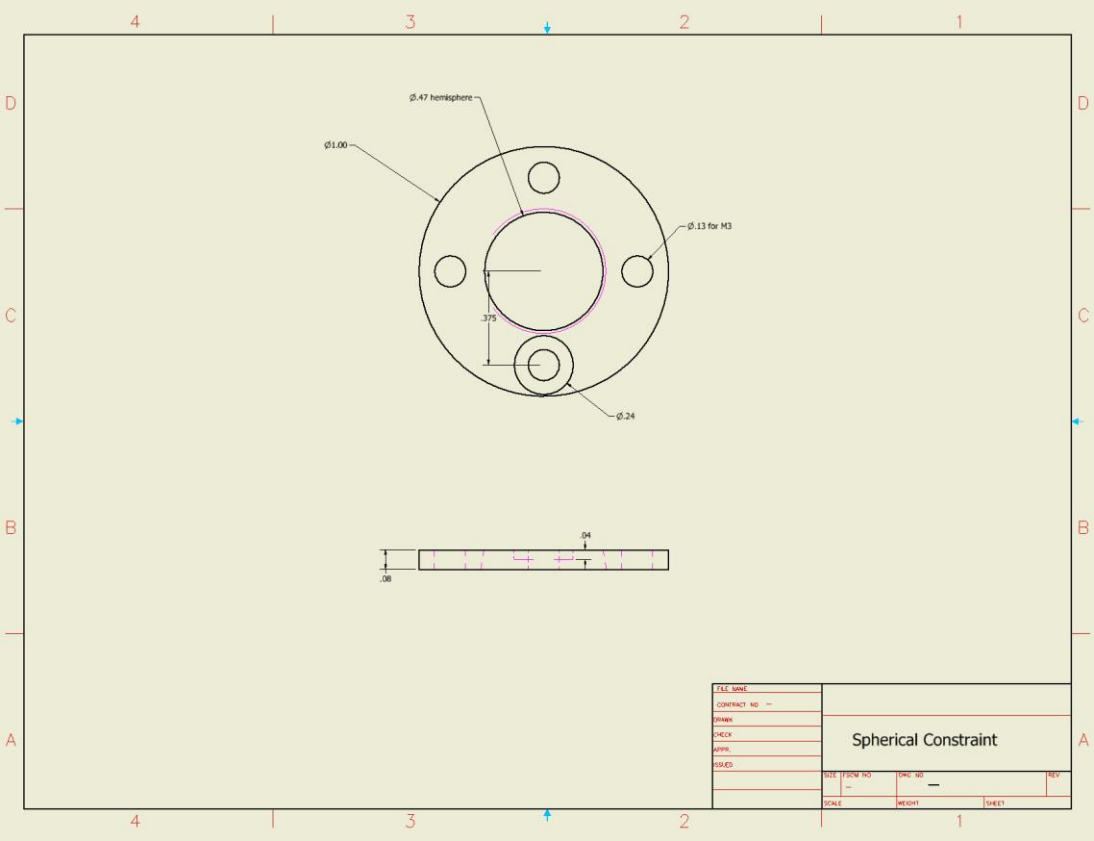

Figure 50: Spherical constraint drawing (Aluminum, AM_ANSI)

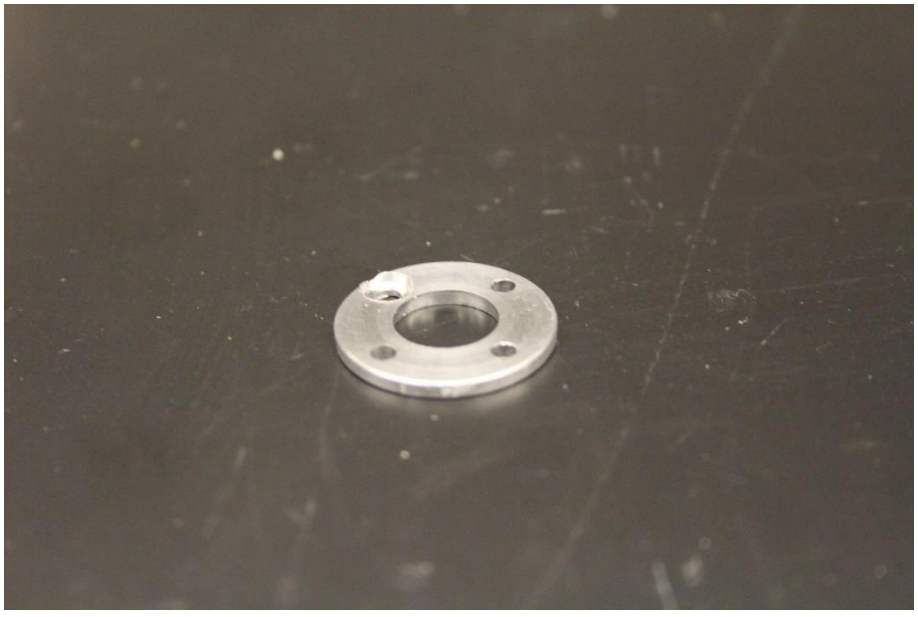

Figure 51: Spherical constraint part

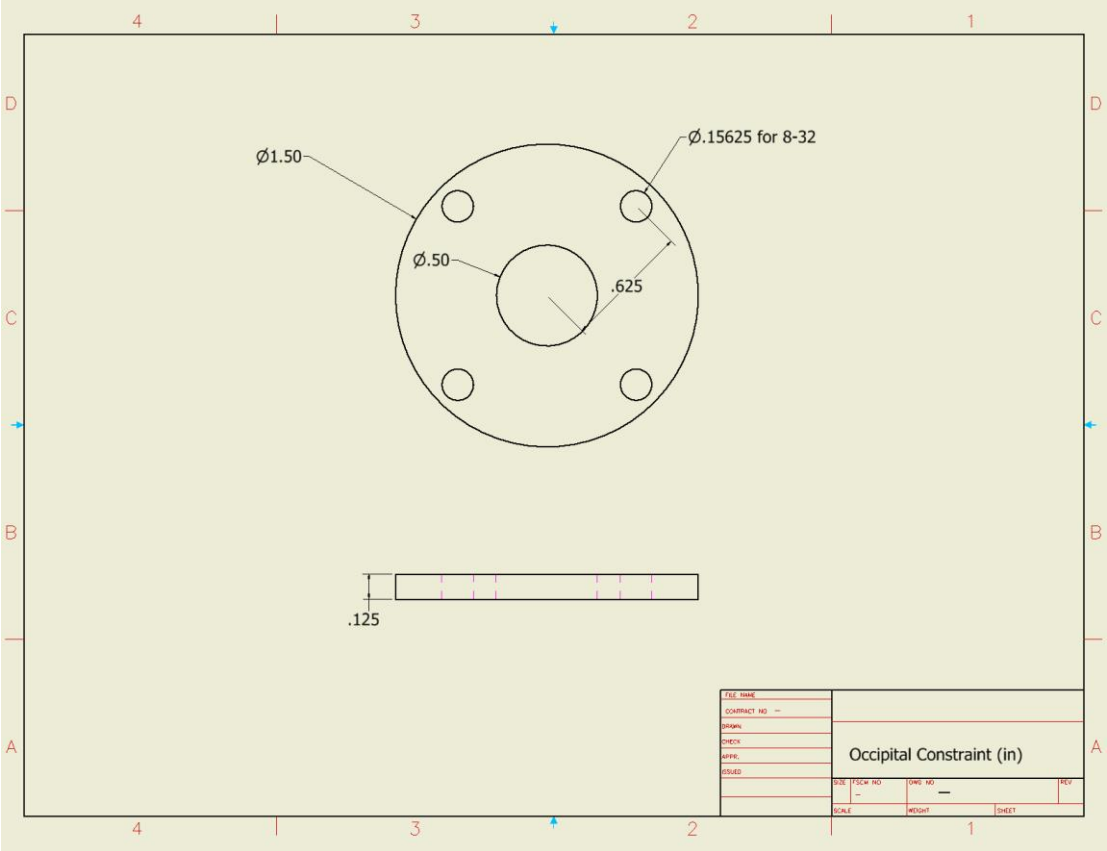

Figure 52: Occipital constraint drawing (Aluminum, AM_ANSI)

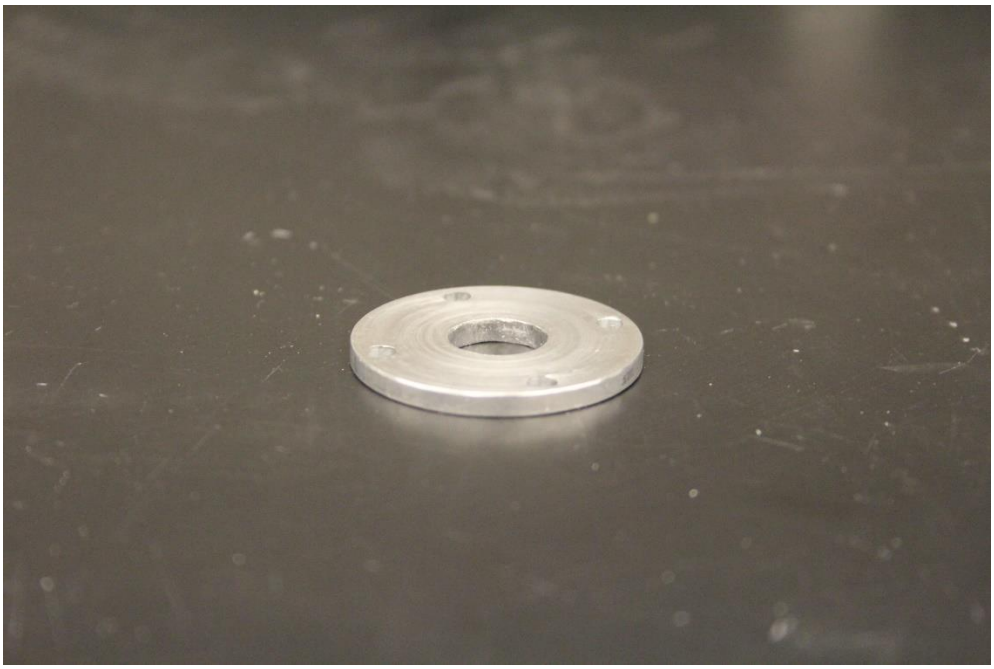

Figure 53: Occipital constraint part

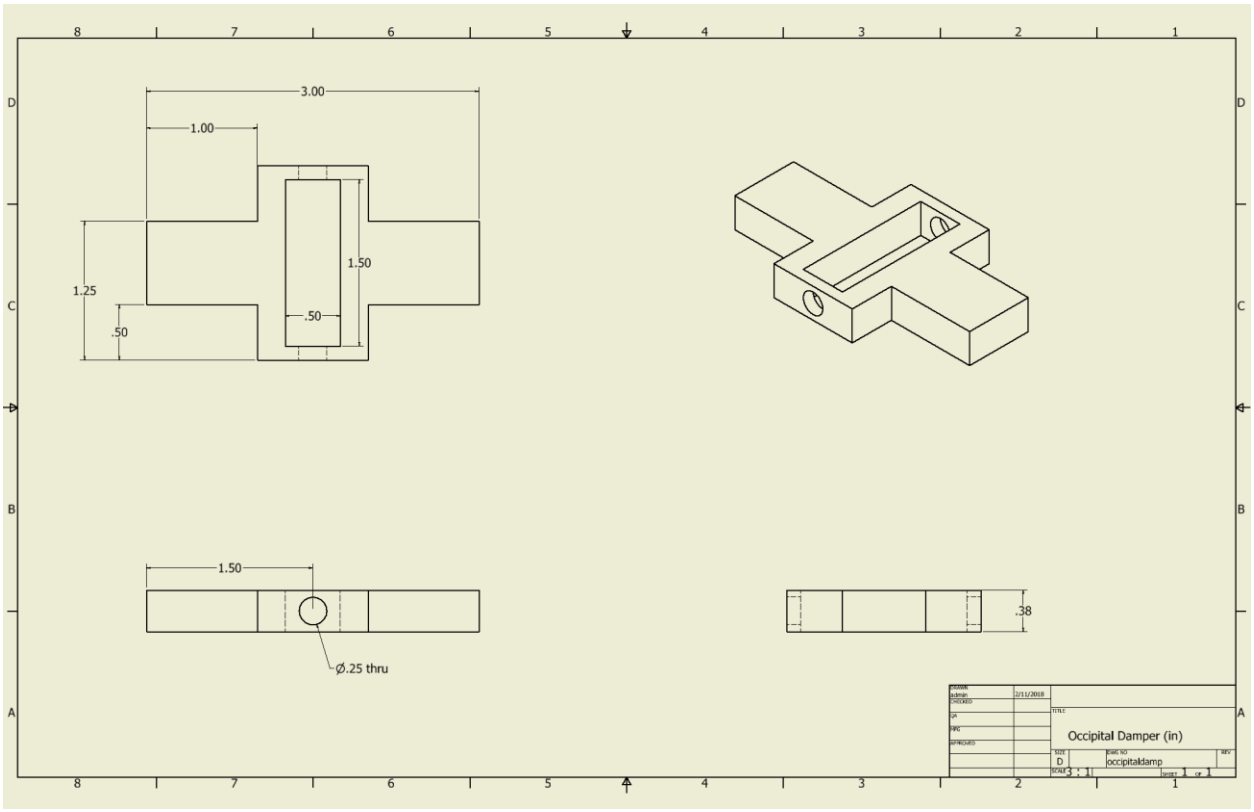

Figure 54: Occipital damper drawing (Aluminum, ANSI)

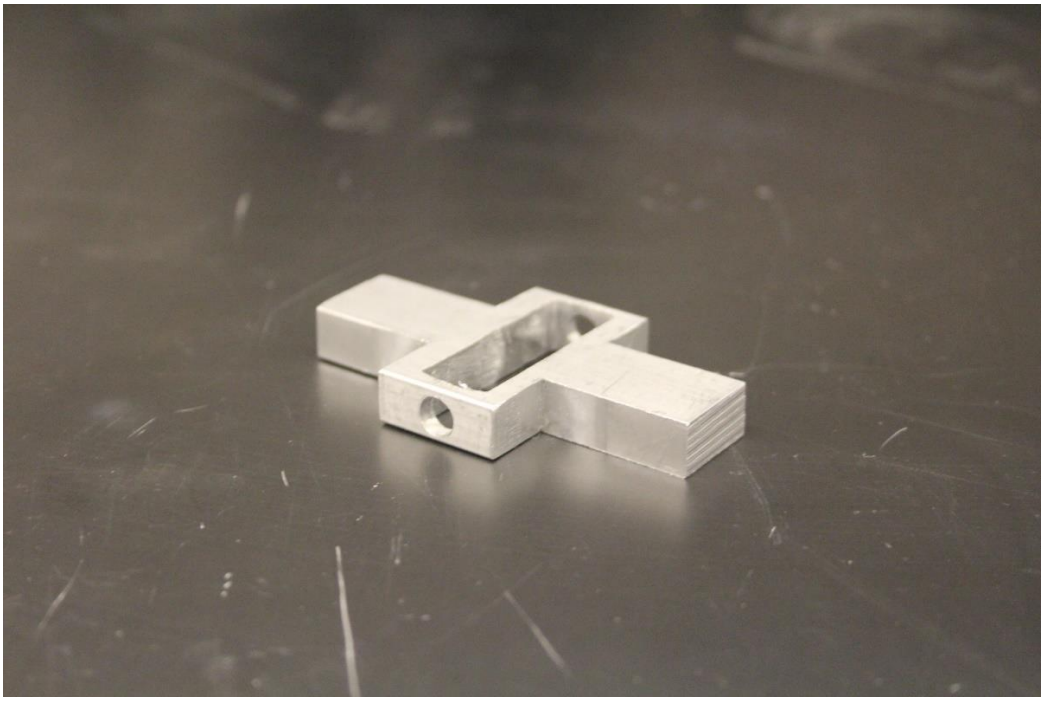

Figure 55: Occipital damper part

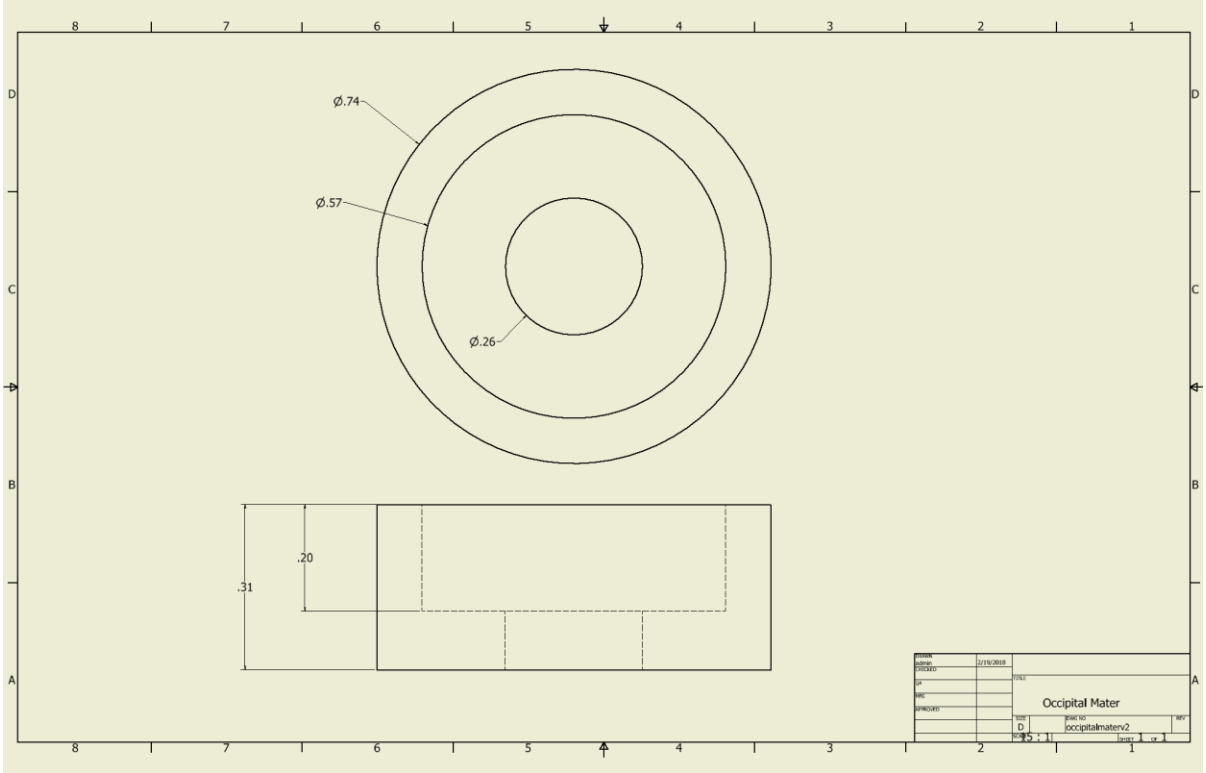

Figure 56: Occipital mater drawing (Aluminum, ANSI)

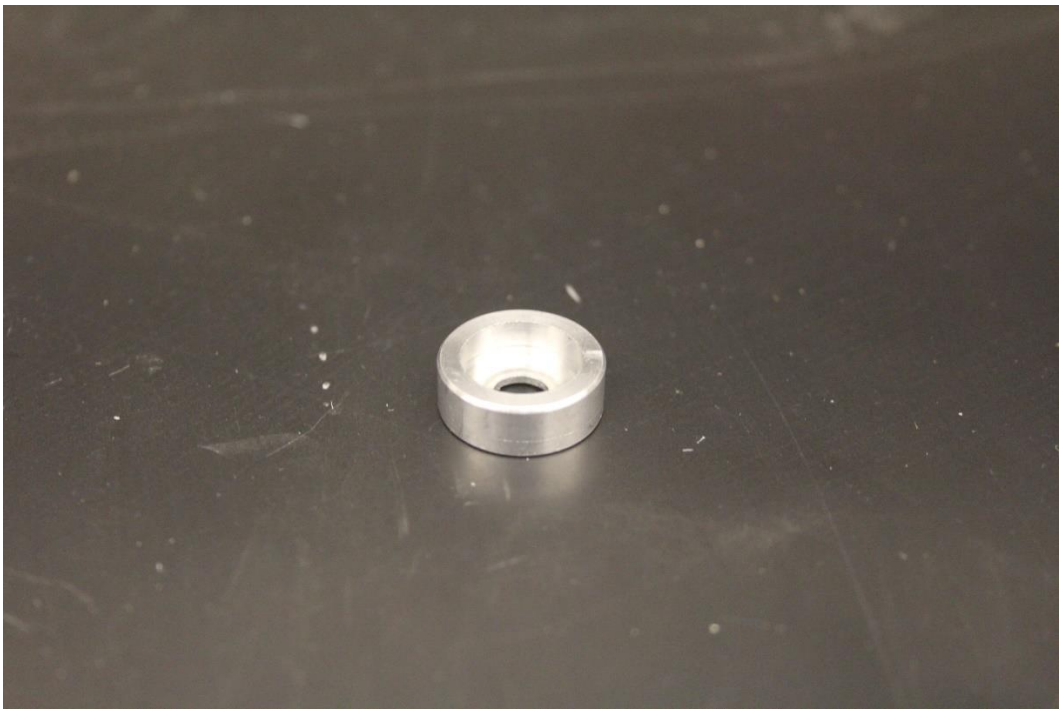

Figure 57: Occipital mater part

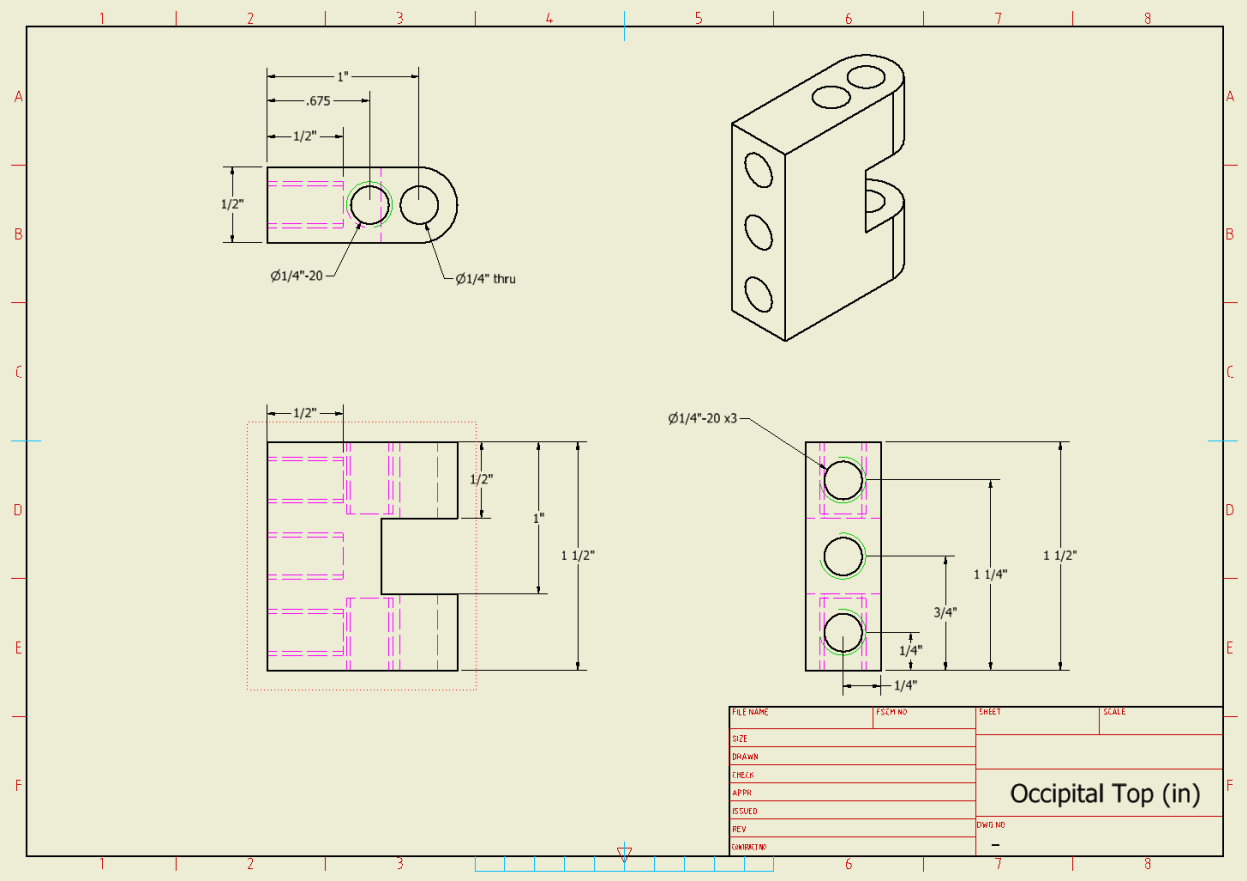

Figure 58: Occipital top drawing (Aluminum, AM_ANSI)

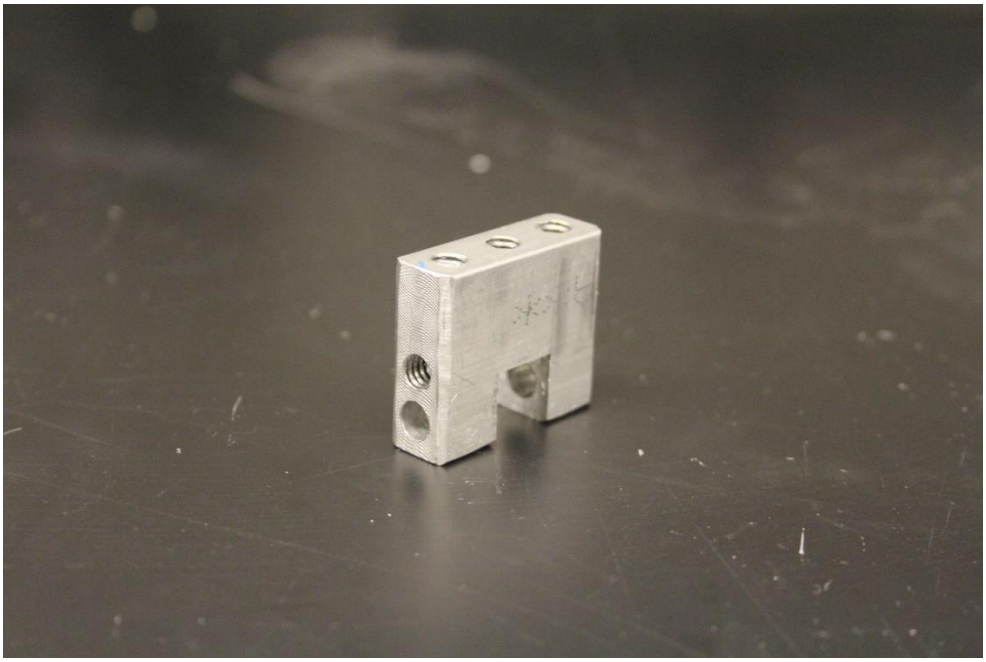

Figure 59: Occipital top part

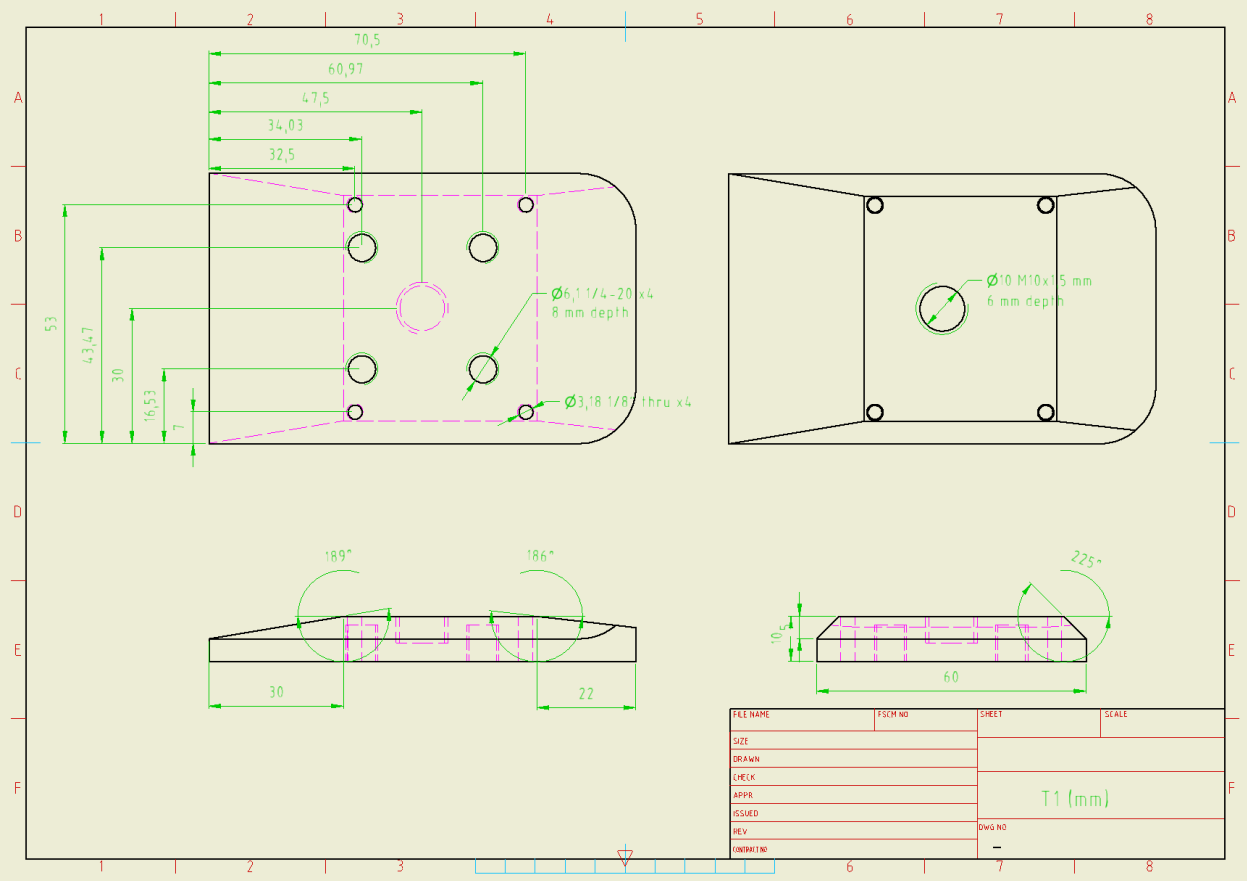

Figure 60: T1 drawing (Aluminum, AM_BSI)

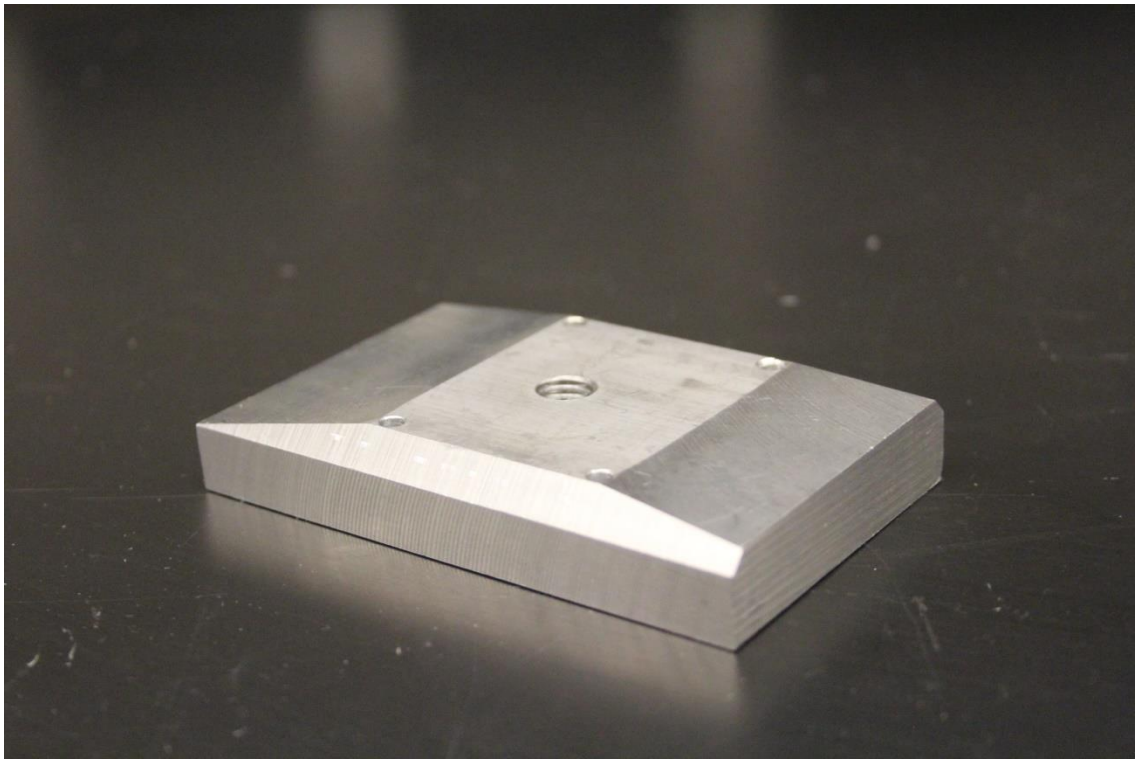

Figure 61: T1 part (top)

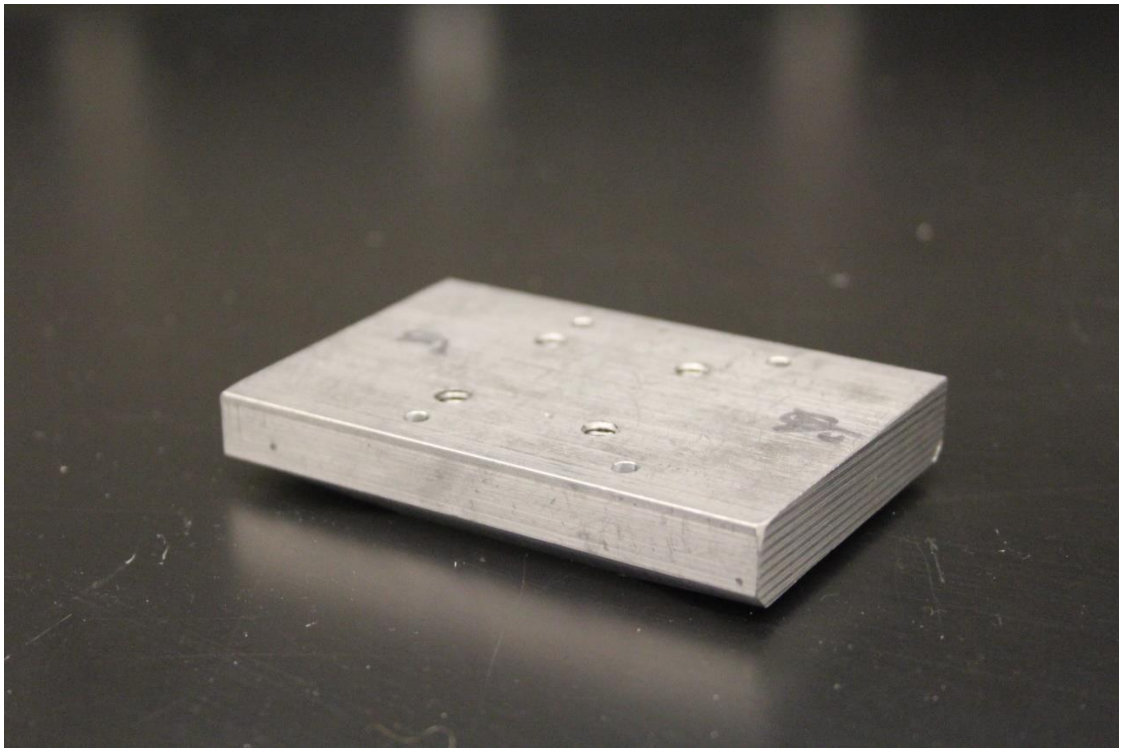

Figure 62: T1 part (bottom)

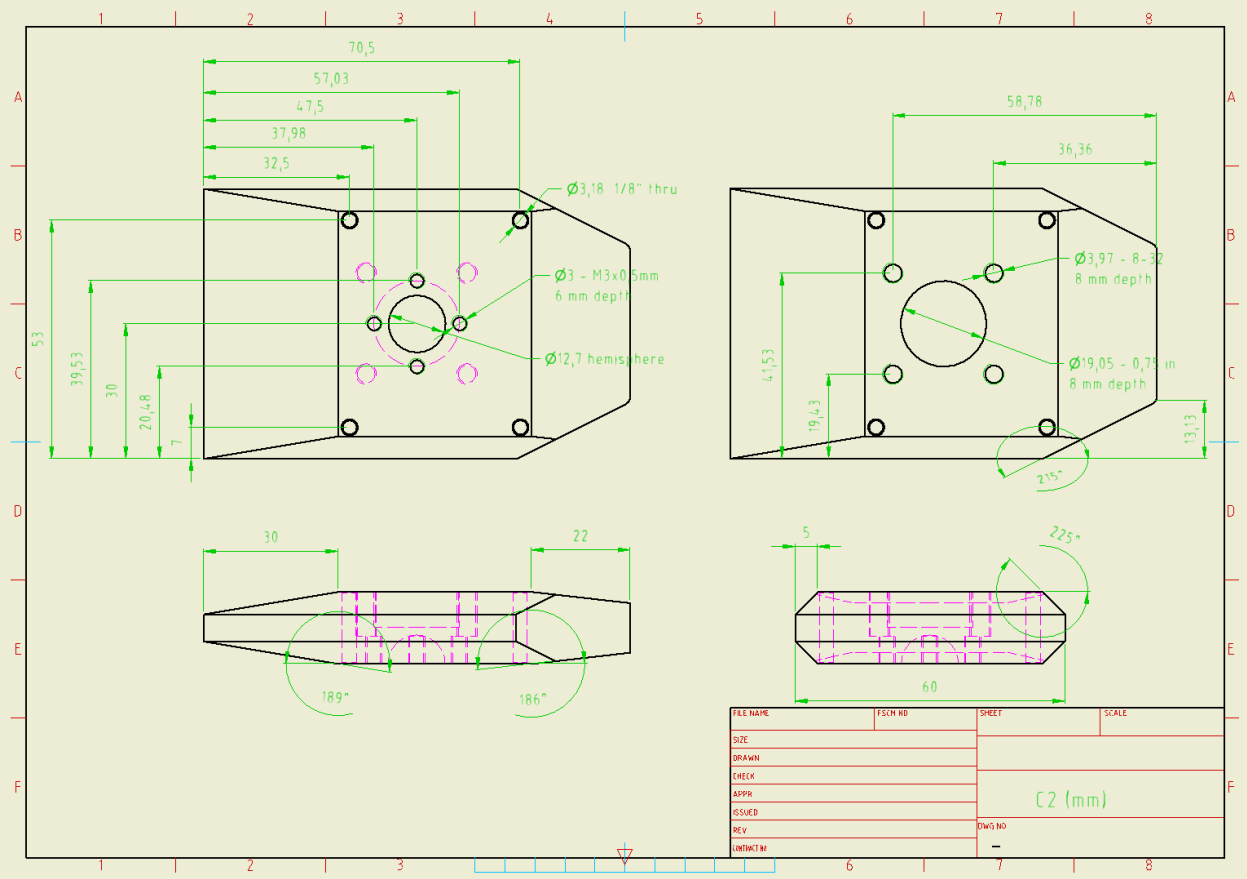

Figure 63: C2 drawing (Aluminum, AM_BSI)

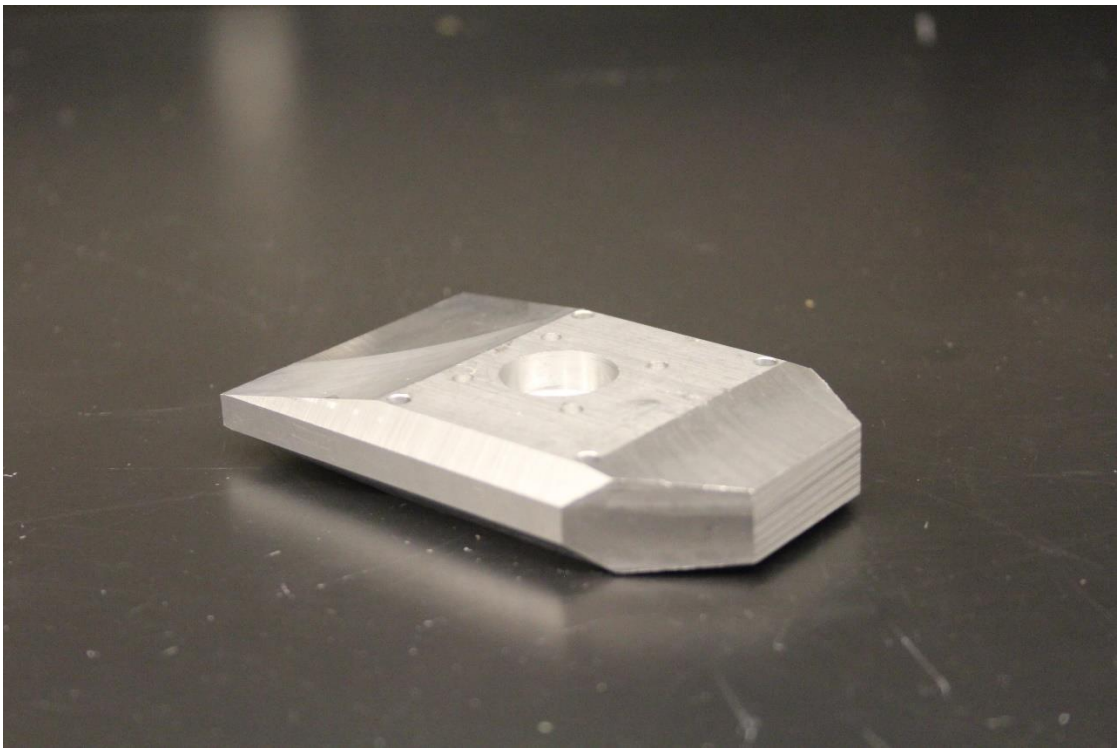

Figure 64: C2 part (top)

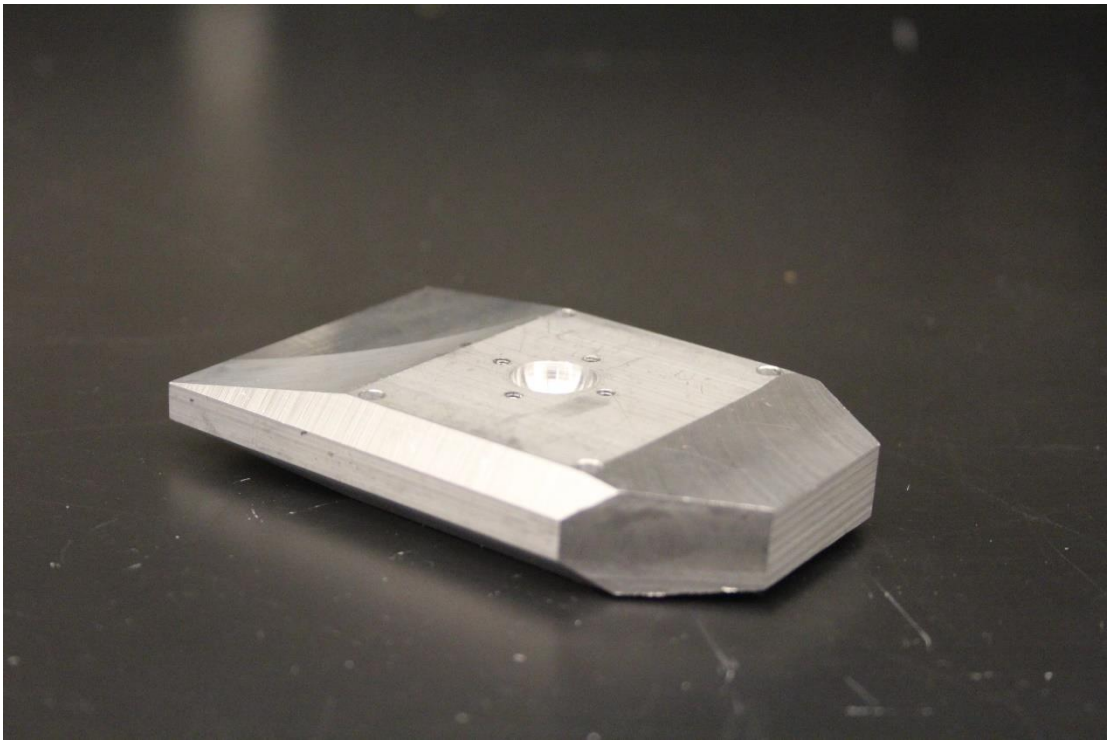

Figure 65: C2 part (bottom)

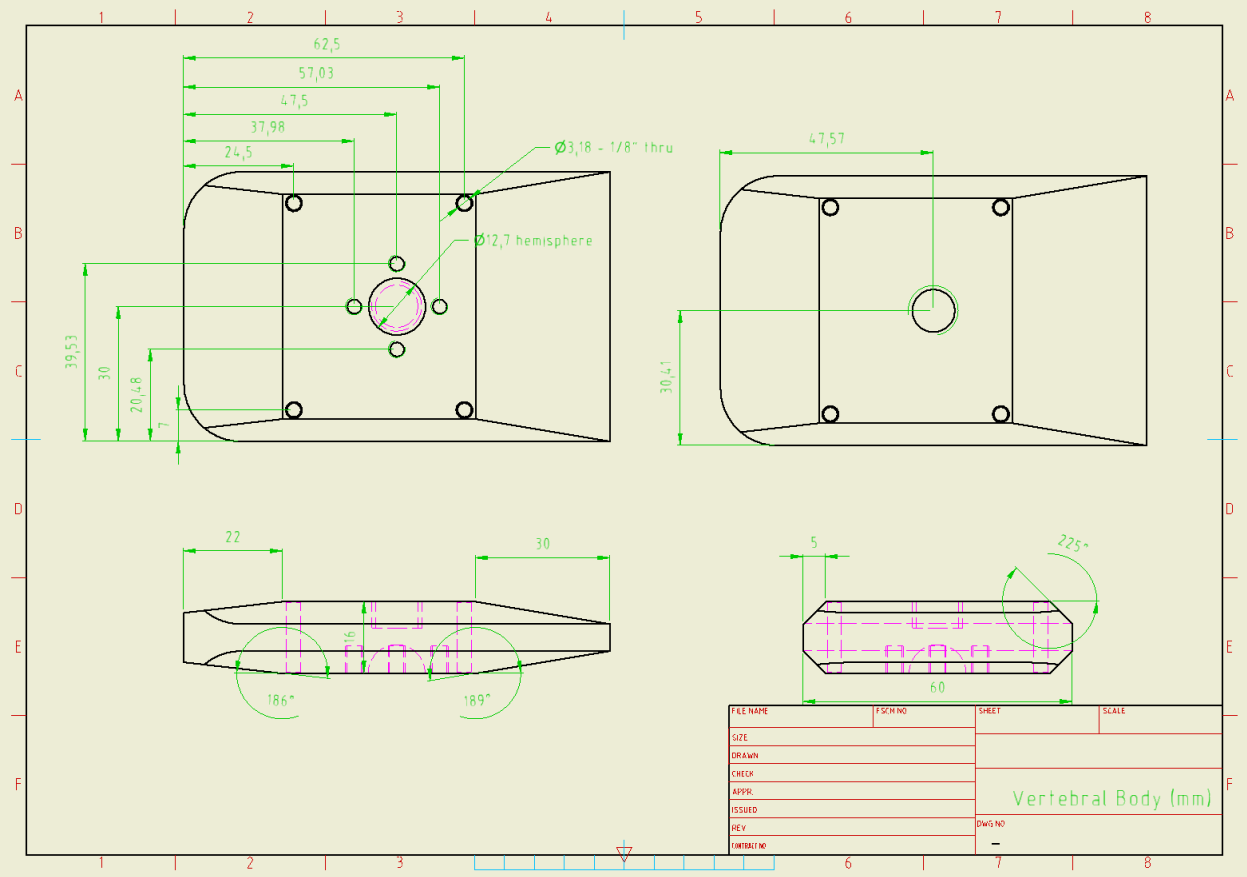

Figure 66: Vertebral body drawing (Aluminum, AM_BSI)

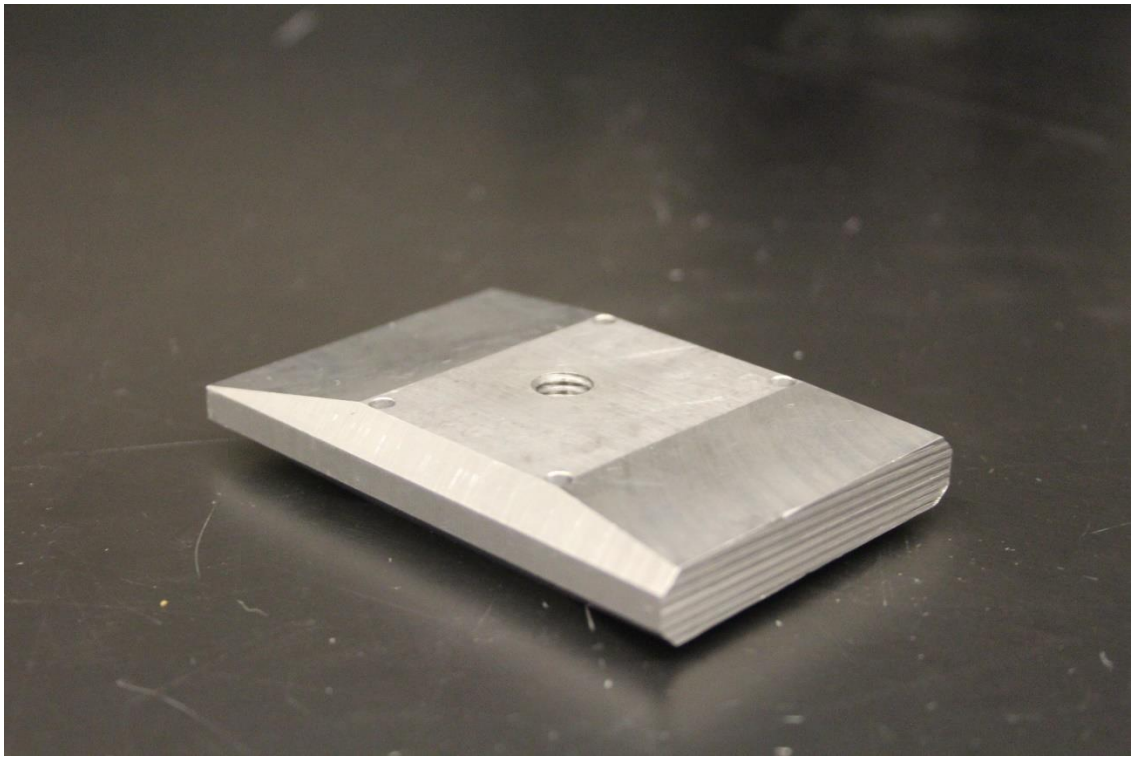

Figure 67: Vertebral body part (top)

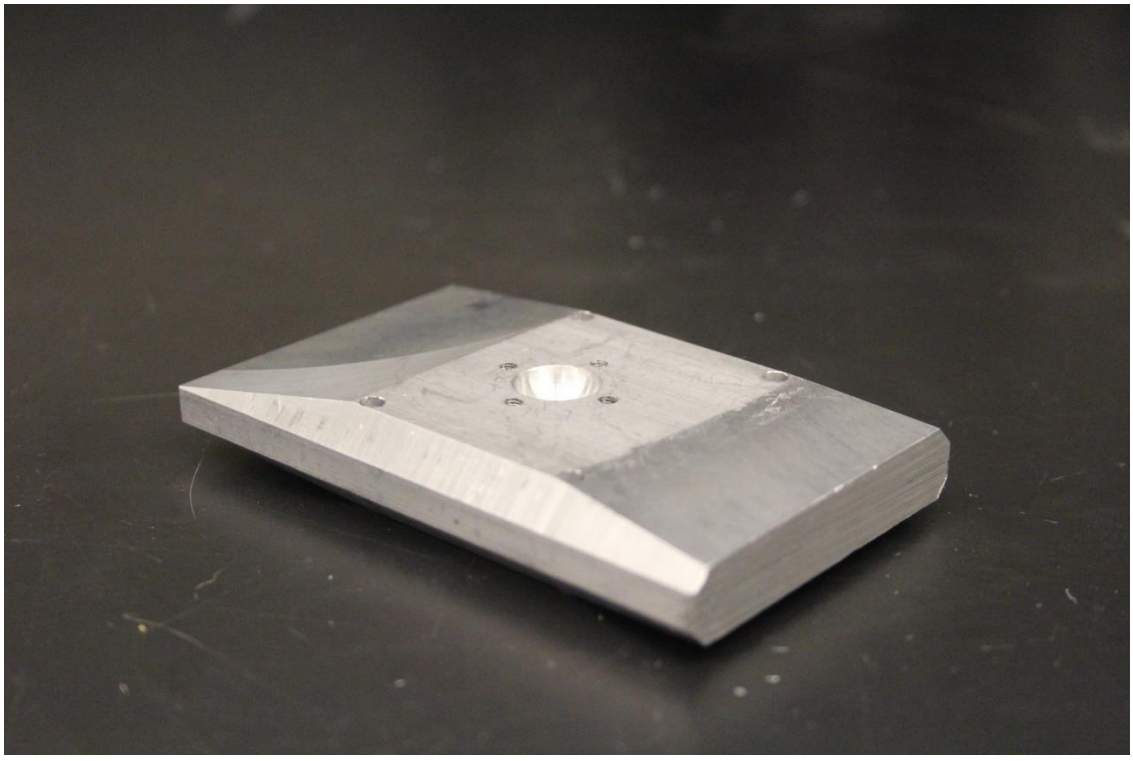

Figure 68: Vertebral body part (bottom)

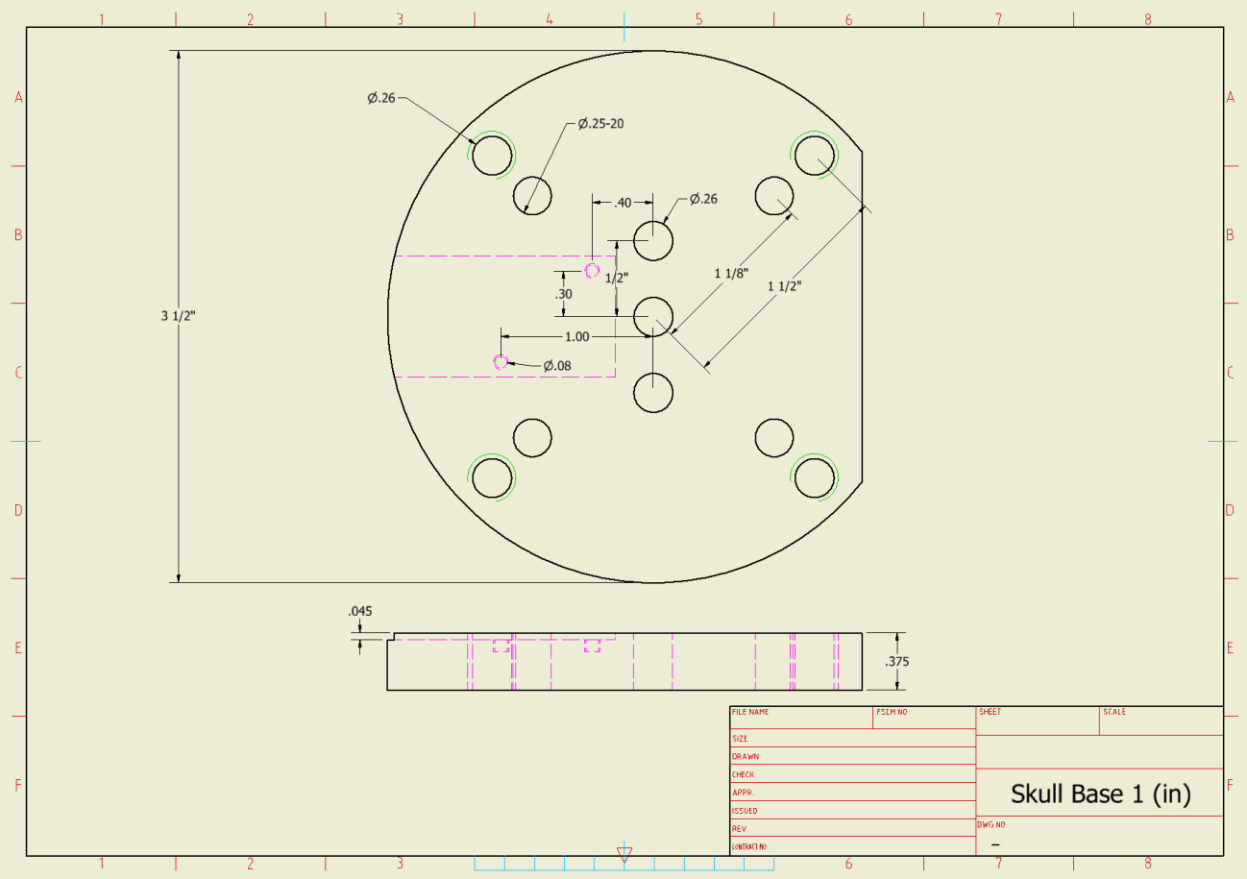

Figure 69: Skull base 1 drawing (Aluminum, AM_ANSI)

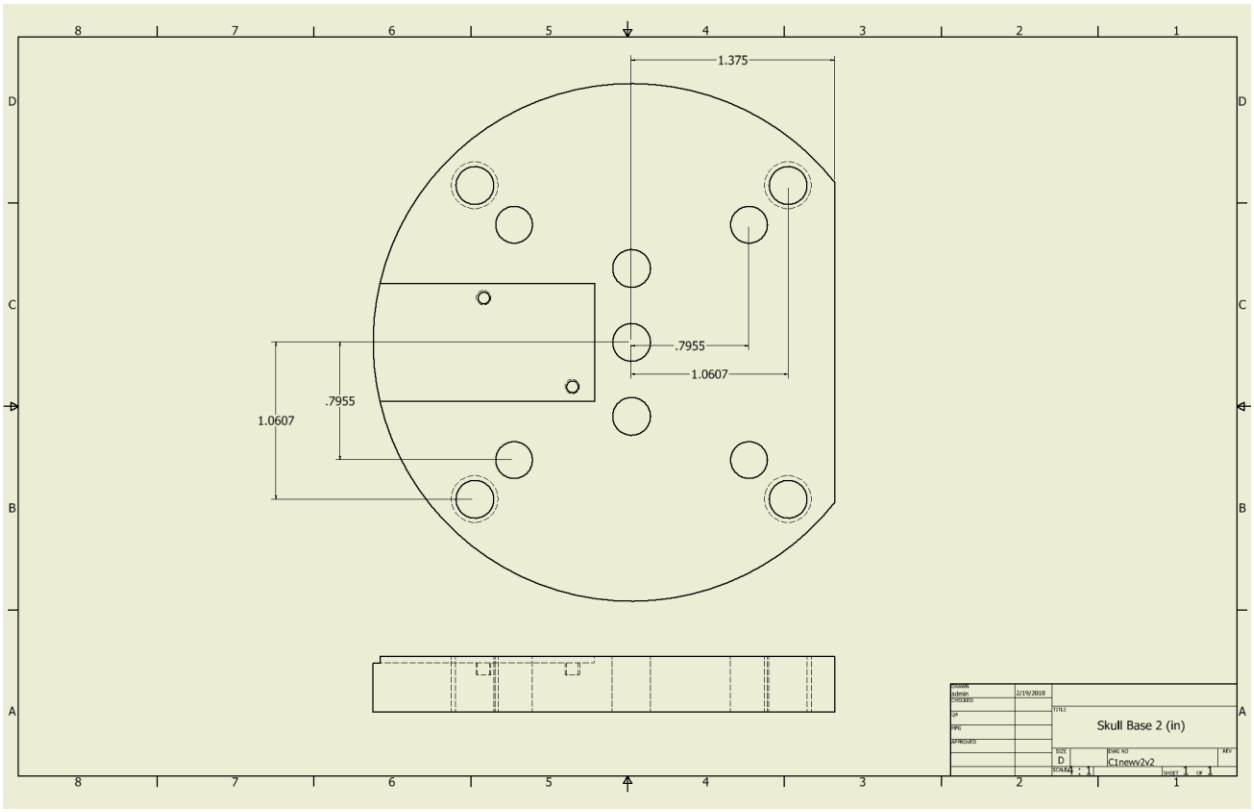

Figure 70: Skull base 2 drawing (Aluminum, ANSI)

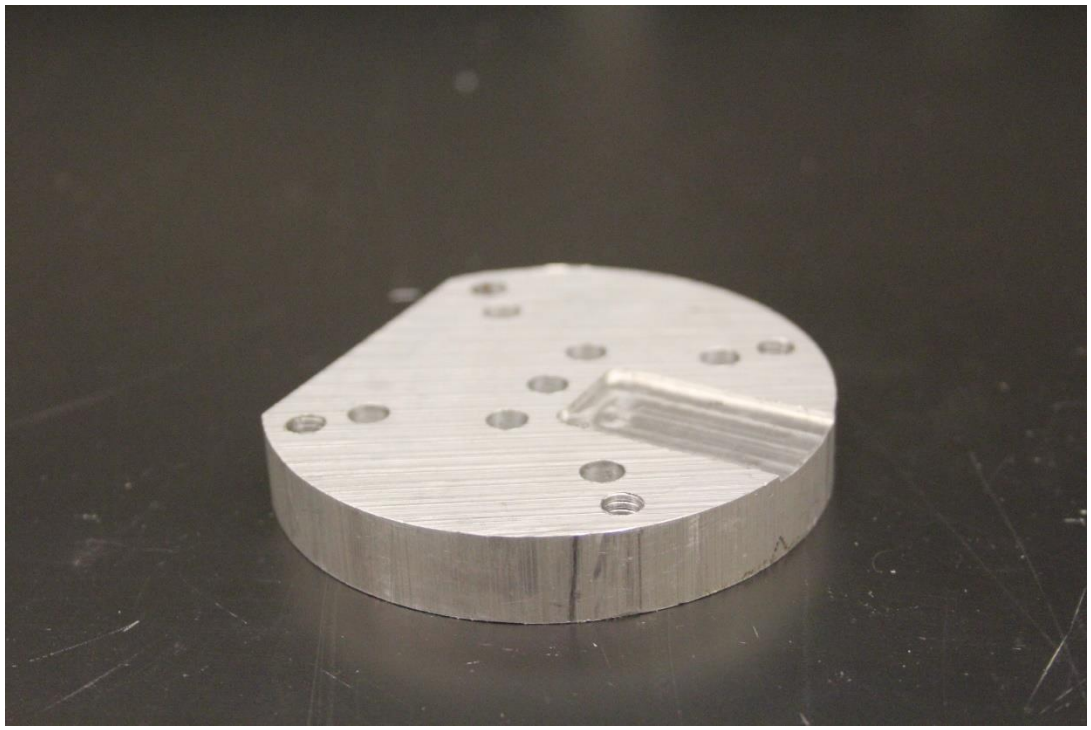

Figure 71: Skull base part (top)

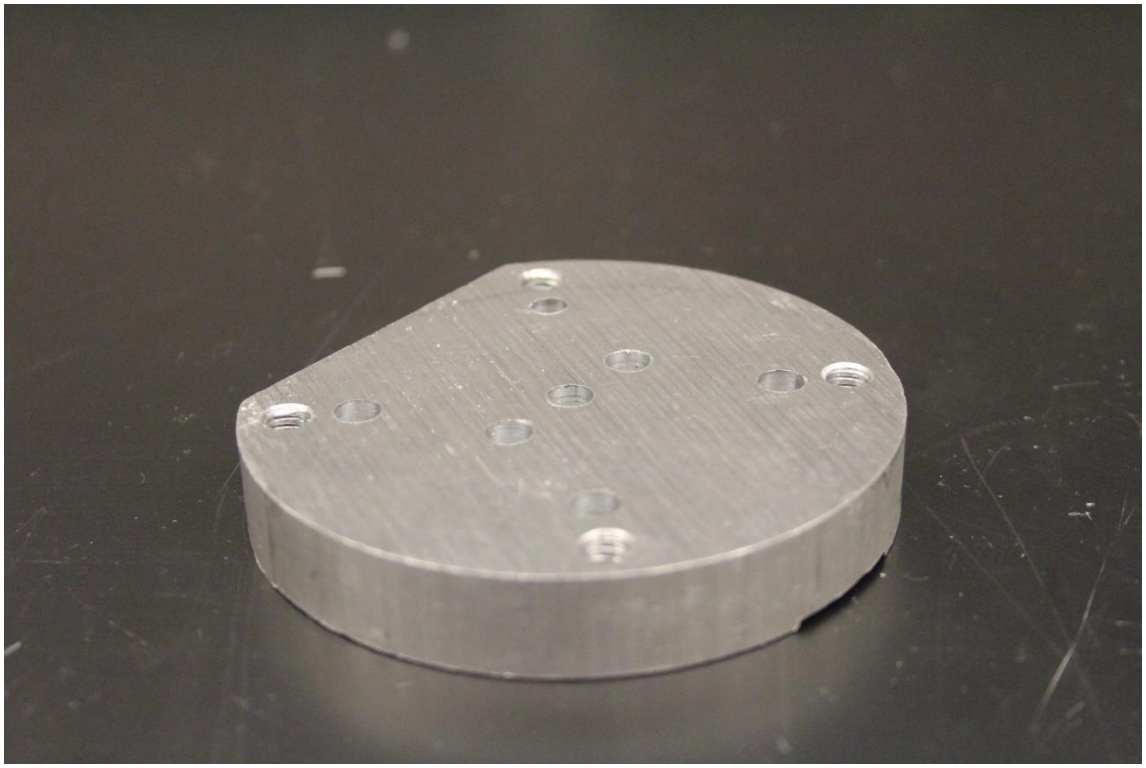

Figure 72: Skull base part (bottom)

APPENDIX B

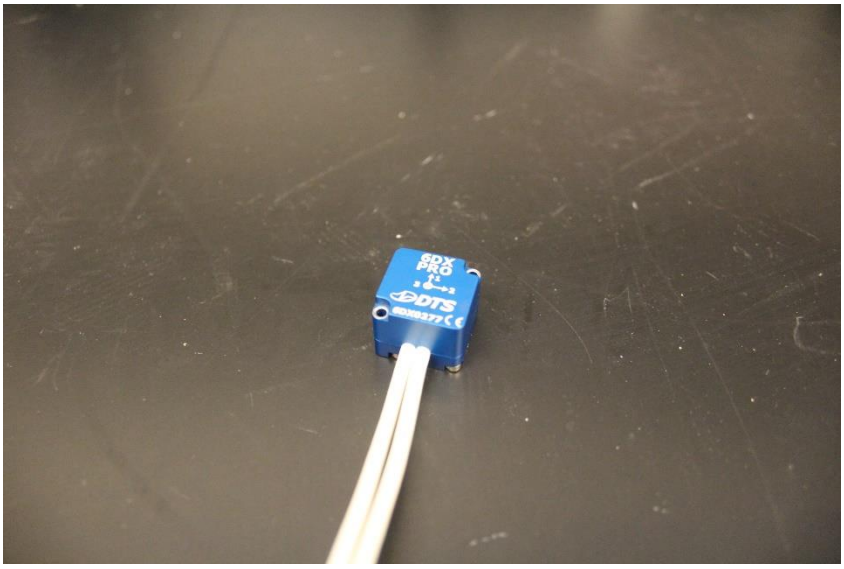

Figure 73: DTS 6DX Pro sensor

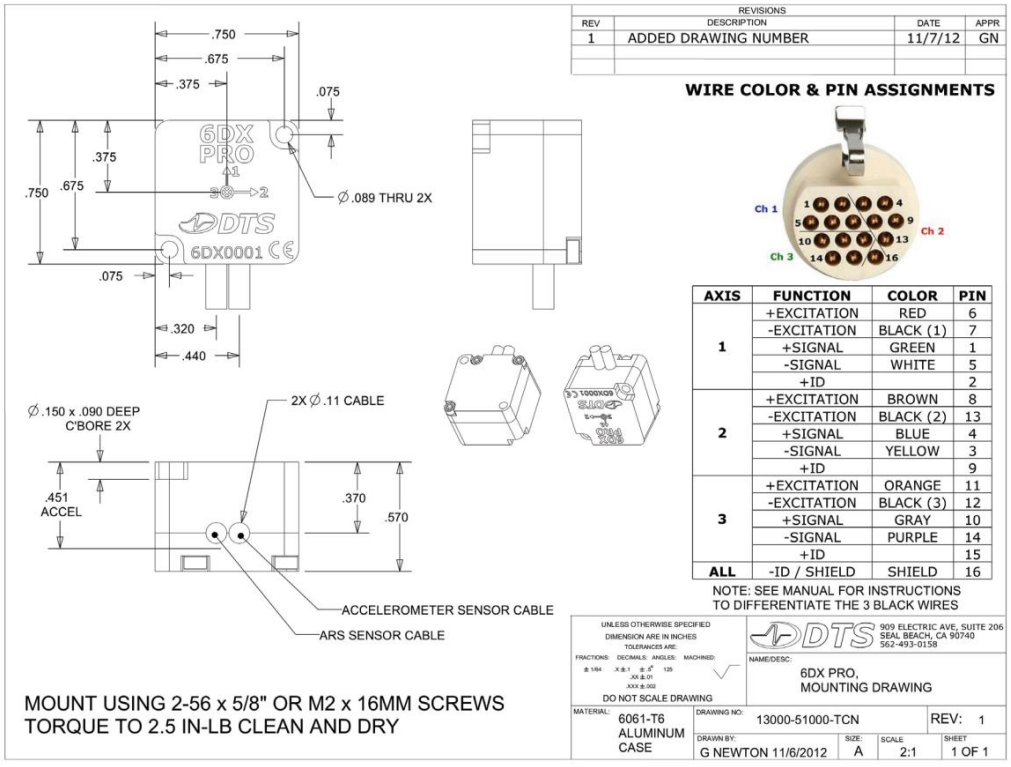

Figure 74: DTS 6DX Pro sensor drawing [32]